ABSTRACT

CHYZH, ANDRII. Neutron Capture Measurements on ^{157}Gd and ^{89}Y at DANCE. (Under the direction of Dr. Gary E. Mitchell).

Neutron capture reactions are of crucial importance for different applications in nuclear physics and nuclear engineering. Common challenges in measuring these reactions are the separation of the (n, γ) channel from other reaction channels, such as (n, el) and (n, n'), that contribute large backgrounds and obscure the γ-ray cascade following neutron capture. Several major facilities focus on neutron capture. Perhaps the best detector for neutron capture measurements is the DANCE (Detector for Advanced Neutron Capture Experiments) array, a 4π array of 160 BaF_2 crystals. In the present research two nuclei were investigated with DANCE: ^{157}Gd and ^{89}Y.

The ^{157}Gd isotope was measured in 2006. It is known for an enormous (n, γ) cross section – the largest one in nature for stable isotopes. ^{157}Gd has several practical applications, including its use as a shutdown system in nuclear reactors, medical therapy, neutron shielding, etc. There are 7 stable isotopes of Gd; this permits the study of the systematics of phenomena such as the scissors mode resonance as a function of mass and deformation. DANCE also enables the improvement of the resonance spectroscopy, including the level density, and thus the strength functions, essential for calculating neutron reaction rates.

^{89}Y was measured with DANCE in 2008, and additional data for improved statistics were taken in the following year. The main motivation was to improve the neutron capture cross section. Yttrium is important for stewardship science and its isotopes are used as radchem detectors to infer the neutron flux. The ^{89}Y(n, γ) cross section is poorly known, with low accuracy and a limited neutron energy range. The major difficulty is that the elastic cross section is so large compared to neutron capture.

This thesis is divided into 3 parts. The 1st part contains a detailed description of the hardware used in both experiments. The 2nd part is dedicated to the ^{157}Gd experiment: how the data were taken, the challenges of the off-line analysis, and comparison of the DANCE results with other existing data, and with statistical model calculations. The 3rd part is about the ^{89}Y experiment. In addition this section explains how the neutron scattering background was simulated with other nuclei, and how the absolute neutron flux was determined with the aid of a resonance in ^{197}Au.

©Copyright 2009 by Andrii Chyzh
All Rights Reserved

Neutron Capture Measurements on ^{157}Gd and ^{89}Y at DANCE

by
Andrii Chyzh

A dissertation submitted to the Graduate Faculty of
North Carolina State University
in partial fullfillment of the
requirements for the Degree of
Doctor of Philosophy

Physics

Raleigh, North Carolina

2009

APPROVED BY:

Dr. Mohamed A. Bourham	Dr. John H. Kelley
Dr. Gary E. Mitchell Chair of Advisory Committee	Dr. Christopher R. Gould

BIOGRAPHY

I always knew that I would be a scientist. When I was 5, I found an old text book with familiar pictures and unfamiliar symbols in my grand mother's book case. It had arrows and text. This is how I taught myself to read. The symbols turned into letters, the arrows became vectors, and that strange text turned out to be formulas and words: universe, galaxy, planet, molecule, nucleus... When I was passing the reading exam to attend elementary school, I did 60 words in a minute, the passing grade was 30.

Naturally, my favorite subjects were any class connected to physics. I was a good student, but this did not stop me from skipping literature classes. Once in the Ukrainian school, while I was escaping from a boring literature class, I saw the school principal, who was looking for students who should be attending class. To escape I stepped into a room... only to find that there was a physics Olympiad for students. The physics teacher, Yaroslav Filimonovich, agreed to save me from the principal if I in return attended the competition. Well, I had never attended an official physics class before. I got the 1st place in the school. Then I got the 1st prize in the city and state. This did not work quite as well for the country competition – my school had no money to send me to that level of competition. Who cares? I beat older students! Until my graduation I was among top 3 students in physics at the school, in city, and state.

In the post-soviet era of economic troubles my parents, Tamara and Viktor, always talked with me about becoming a lawyer, economist, doctor, musician, ... anything but a scientist. That was what children were doing. But I always knew I would be a scientist, and they supported me in whatever I was determined to do. The same path of scientist was chosen by my younger brother Roman.

In 1998 I was accepted to the National University of Kiev (KNU), one of the best schools in the country, without even taking the entrance exams since I was a holder of the 3rd prize in the Physics Olympiad, a state level. The university math was hard, the physics – easy. Since my first year I knew my major would be nuclear physics. I took numerous major related classes in nuclear physics, spectroscopy, and electronics.

My bachelor's project was to investigate the active zone of the nuclear reactor. I learned what kinds of reactions take place there, how to calculate macro cross sections for some reaction channels using the WIMSD-5B code, how the nuclear fuel changes its

physical properties at criticality inside the reactor. This all happened thanks to my adviser Dr. Alexander Shkarupa.

I was determined to learn nuclear physics further. My next step was to get a masters degree. My MS project was connected to nuclear reactors again, namely PWR-1000. The goal was to investigate how much radiation damage occurs inside the reactor wall. The neutron beam is measured inside the reactor and right outside on its shell, but there is no way to measure it inside the wall because of the safety requirements. I built the MCNP-4C model of the 1/6 segment of the PWR-1000 reactor to use the neutron flux measured on the internal side of the wall as an input for my model to get the neutron flux distribution as a function of the wall thickness. This work was performed under adviser Dr. Volodymyr Borysenko.

After my graduation with the masters degree I was eager to continue education in nuclear physics and in 2003 attended the Kiev Institute for Nuclear Research (KINR), Neutron Physics Department. I was working closely with Dr. Vladimir Libman. The experiment I was working on was to measure the neutron capture cross section on ^{181}Ta with a precision better than 5%. The only source of neutrons we had was the 10 MW reactor, so in order to get the 1.95-keV quasi-monoenergetic neutron energy line we combined filters from different isotopes.

In 2005 I was accepted to the North Carolina State University, Physics Department. My immediate choice was to do nuclear physics with Dr. Gary Mitchell, who later arranged my visit to the Los Alamos National Laboratory. My PhD research was to investigate neutron capture reactions on ^{157}Gd and ^{89}Y. I performed the experiments and analyzed the data, the cross sections were determined and the results on resonance spectroscopy were produced for these nuclei.

This thesis is about what happened between 2005 and 2009.

ACKNOWLEDGMENTS

I would like to give my sincere thanks and acknowledgments to several key people who assisted me in doing this research.

My supervisor – Dr. Gary Mitchell, North Carolina State University – who played a major role in my studying, provided me with his ideas on the theoretical topics and made a significant contribution to get this research complete in time. Dr. David Vieira – a scientist at the Los Alamos National Laboratory – who was my host at this lab and helped me to conduct the ^{89}Y experiment. Dr. Marian Jandel – a scientist at the same laboratory – who instructed me on details and different aspects of how to analyze the DANCE data. Dr. Todd Bredeweg – a scientist at the same laboratory – who was very supportive on the technical side and explained many aspects of the DANCE hardware. Dr. John Ullmann and Dr. Aaron Couture – the instrumental scientists at LANSCE – for their valuable meeting discussions that gave me a clear prospective view of how to perform the experiments at DANCE. In addition thanks go to Dr. Milan Krticka from the Charles University at Prague, for his assistants in the DICEBOX simulations and Dr. Anton Tonchev from the Triangle University Nuclear Laboratory (TUNL) – credits for preparing me for work with the Acquiris digitizers. My utmost thanks to all of the DANCE collaborators – people that made the DANCE project come to life.

The main credits go to the North Carolina State University, Physics Department, and the Los Alamos National Laboratory. I have broadened my scientific horizons and spent unforgettable years during my Ph.D. studies at NCSU and gained an invaluable research experience at LANL. This university as well as the national lab gave me an excellent opportunity to become a nuclear physics scientist.

TABLE OF CONTENTS

LIST OF TABLES ..... **vii**

LIST OF FIGURES ..... **viii**

1 Hardware **1**
1.1 Introduction 1
1.2 LINAC at Los Alamos Neutron Science Center (LANSCE) 1
1.3 Spallation Neutron Source, Lujan Center, Flight Path 14 3
1.4 Time-of-Flight (TOF) technique 5
1.5 DANCE array 6
1.6 Neutron beam monitors 9
1.7 Data acquisition system 10
1.8 Pulse shape discrimination 12
1.9 Raw data overview 13

2 ^{157}Gd Experiment **16**
2.1 Introduction 16
2.2 Neutron capture measurements on ^{157}Gd 16
2.2.1 The ^{157}Gd and ^{9}Be targets 17
2.2.2 Experimental setup 18
2.3 Data analysis 19
2.3.1 Raw cluster data 19
2.3.2 DANCE analyzer 21
2.3.3 Particle identification (PI) 22
2.3.4 γ-energy calibration 26
2.3.5 Time calibration (alignment) 28
2.3.6 Multiplicity 29
2.3.7 Energy spectra 31
2.3.8 Background subtraction 33
2.3.9 Dead-time corrections 36
2.3.10 Beam attenuation and target self shielding 39
2.4 Resonance spectroscopy 42
2.4.1 Determination of the ^{157}Gd(n,γ) cross section 42
2.4.2 Resonance spin assignments 44
2.4.3 Resonance parameters and comparison with nuclear data libraries 49
2.4.4 DICEBOX/GEANT4 simulations 53
2.4.5 DICEBOX simulations of DANCE neutron capture data 56
2.4.6 Summary 59

3 ^{89}Y Experiment 60
3.1 Introduction 60
3.2 Neutron capture measurements on ^{89}Y 61
3.2.1 Targets: ^{nat}Y, ^{nat}Fe, ^{nat}Pb, ^{208}Pb, ^{181}Ta, ^{197}Au 62
3.2.2 Experimental setup 65
3.3 Data analysis 65
3.3.1 Overview of the raw data spectra 66
3.3.2 Time calibration spectra. Differential cross section. γ-energy calibration. Particle identification (PI). 68
3.3.3 ^{181}Ta contaminant in the ^{nat}Y targets 69
3.3.4 Simulating neutron scattered ^{89}Y(n, el) background 72
3.3.5 Corrections for beam attenuation and target self shielding 75
3.3.6 Processing losses – efficiency of cuts 78
3.3.7 Neutron flux determination using ^{197}Au as a reference 80
3.3.8 Determination of the ^{89}Y(n, γ) cross section 81
3.4 Discussion of results 82
3.4.1 Spin assignments in ^{89}Y resonances 83
3.4.2 ^{89}Y(n, γ) cross sections for 3 targets 85
3.4.3 Comparison of DANCE data with ENDF and EXFOR 87
3.4.4 Summary 88

Bibliography 90

Appendices 93
Appendix A 94

A Results on ^{157}Gd 94
A.1 List of additional figures for ^{157}Gd 94
A.2 List of additional tables for ^{157}Gd 112

LIST OF TABLES

Table 1.1 Isotopic abundances in ^{nat}Ba. 7

Table 1.2 Energies [MeV] of Ra decay chains. The ^{226}Ra decay chain is dominant; 5 α-lines are used to calibrate DANCE for γ-energies. 7

Table 2.1 Percent composition of the ^{157}Gd target and of natural Gd. 17

Table 2.2 Results of resonance spectroscopy for ^{157}Gd compared to the Atlas of Neutron Resonances of Mughabghab. 50

Table 3.1 Targets used in the ^{89}Y(n,γ) experiment. 63

Table 3.2 Q–values for (n,γ) on Y, Ta and Barium. 67

Table A.1 Results on the 3 methods (author, Koehler, Becvar) of the spin assignment for the ^{157}Gd resonances compared to the Atlas of Neutron Resonances of Mughabghab. 112

LIST OF FIGURES

Figure 1.1 An aerial view of LANSCE. . . . 2

Figure 1.2 Vertical cross section of SNS, with W – tungsten target and Be, Pb, Fe backscattering system. . . . 3

Figure 1.3 The Lujan center flight paths; DANCE is at FP14. . . . 3

Figure 1.4 Scheme of FP14 at the Lujan center. . . . 4

Figure 1.5 DANCE array. . . . 8

Figure 1.6 DANCE is built from crystals of 4 shapes: 12 of type A, 30 of type B, 60 of type C, and 60 of type D. . . . 8

Figure 1.7 DANCE cutaway scheme. . . . 8

Figure 1.8 Scheme of acquisition hardware. . . . 10

Figure 1.9 Sequence of events in one beam pulse. . . . 10

Figure 1.10 PMT Waveform– fast and slow components are digitized with 2 ns increments. . . . 13

Figure 1.11 PMT waveforms for gamma rays and alpha particles. . . . 13

Figure 1.12 Schematic view of the raw data analysis. . . . 15

Figure 2.1 ^{89}Y target. . . . 18

Figure 2.2 Aluminum target holder. . . . 18

Figure 2.3 Scheme of ^{157}Gd experiment. . . . 19

Figure 2.4 I_{fast} vs. I_{slow} for BaF_2 crystal. . . . 23

Figure 2.5 I_{fast} vs. I_{slow} for ^{235}U beam monitor. . . . 23

Figure 2.6 I_{fast} vs. I_{slow} for BF_3 beam monitor. . . . 23

Figure 2.7 I_{fast} vs. I_{slow} for Si beam monitor. . . . 23

Figure 2.8 γ-energy calibration with internal α-activity. 26

Figure 2.9 Distribution of physical event time stamps relative to the crystal 0. 29

Figure 2.10 $M_{cr} = 1$ and $M_{cl} = 1$. 30

Figure 2.11 $M_{cr} = 2$ and $M_{cl} = 2$. 30

Figure 2.12 $M_{cr} = 3$ and $M_{cl} = 3$. 30

Figure 2.13 $M_{cr} = 2$ and $M_{cl} = 1$. 30

Figure 2.14 $M_{cr} = 3$ and $M_{cl} = 2$. 30

Figure 2.15 $M_{cr} = 9$ and $M_{cl} = 3$. 30

Figure 2.16 E_n vs. E_{sum} 2D plot for ^{157}Gd(n,γ) without multiplicity cuts. 32

Figure 2.17 E_n vs. E_{sum} 2D plot for ^{157}Gd(n,γ) multiplicity cuts. 32

Figure 2.18 E_n yield with and without multiplicity cuts. 32

Figure 2.19 $E_{\sum}$ yield with and without multiplicity cuts. 32

Figure 2.20 Unnormalized E_n spectra of ^{157}Gd and ^{9}Be. 34

Figure 2.21 Neutron scattering background subtraction: $K_{Be} = \frac{Yield(Gd)}{Yield(Be)}$ 34

Figure 2.22 E_n spectrum of K_{Be} correlates with the ^{nat}Ba(n,γ) cross section. 34

Figure 2.23 E_n spectra of ^{157}Gd before and after background subtraction. 34

Figure 2.24 Dead time corrections in E_n scale for one run. 39

Figure 2.25 Beam image without target 41

Figure 2.26 Beam image after attenuation by the ^{157}Gd target. 41

Figure 2.27 Neutron beam spectra with the ^{157}Gd target and the ^{9}Be blank. 41

Figure 2.28 Attenuation of the neutron beam by ^{157}Gd. 41

Figure 2.29 Cross section of ^{157}Gd(n,el): DANCE vs. ENDF/B-VII. 43

Figure 2.30 Average γ-ray multiplicity. Resonances are divide into two distinct groups – one per spin value. 45

Figure 2.31 M_{cl} distributions are the same if the spins are equal. 46

Figure 2.32 E_n spectrum of M3-M5 reveals resonances with $J = 1$ as positive peaks.... 47

Figure 2.33 E_n spectrum of M3-M6 reveals the same resonances with $J = 1$ as in Fig. 2.32.... 47

Figure 2.34 Cross sections of the two possible spin assignments, $J = I \pm 1/2$, for each resonance.... 49

Figure 2.35 E_{sum} spectra of the 44.2-eV resonance for $M_{cl} = 2$ – 5: simulation (red) vs. experiment (blue).... 55

Figure 2.36 E_γ spectra of the 44.2-eV resonance for $M_{cl} = 2$ – 5: simulation (red) vs. experiment (blue).... 55

Figure 3.1 Yttrium has one stable isotope: ^{89}Y.... 60

Figure 3.2 Chain of yttrium transformations following neutron exposure.... 62

Figure 3.3 EXFOR data for $^{89}\mathrm{Y}(n,\gamma)$.... 62

Figure 3.4 ENDF/B-VII, JEFF, and JENDL data for $^{89}\mathrm{Y}(n,\gamma)$.... 62

Figure 3.5 2 D spectrum for the thick yttrium target for M_3.... 66

Figure 3.6 Differential cross section of $^{89}\mathrm{Y}(n,el)$ at several E_n energies.... 70

Figure 3.7 Downstream DANCE crystals experience higher (n,el) background than upstream crystals.... 70

Figure 3.8 Neutron spectra of ^{89}Y contaminated with ^{181}Ta and of pure ^{181}Ta.... 71

Figure 3.9 Yttrium neutron spectrum after ^{181}Ta is subtracted.... 71

Figure 3.10 ENDF/B-VII data on (n,γ) and (n,el) for ^{89}Y and ^{208}Pb.... 73

Figure 3.11 Subtraction of the $^{89}\mathrm{Y}(n,el)$ background simulated through $^{208}\mathrm{Pb}(n,el)$ within one E_n bin.... 73

Figure 3.12 $K_{Pb}(E_n)$ correlates with the ratio $\frac{^{89}Y(n,el)}{^{208}Pb(n,el)}$.... 73

Figure 3.13 $^{89}\mathrm{Y}(E_n)$ spectra before and after subtracting the $^{89}\mathrm{Y}(n,el)$ background.... 73

Figure 3.14 Self-shielding effects for ^{89}Y.... 77

Figure 3.15 E_{sum} spectrum for $M_{cl} = 2$; The closer cut to the Q-value, the larger the signal-to-noise.... 78

Figure 3.16 The M distributions for ^{89}Y are not as distinctive as for ^{157}Gd. 83

Figure 3.17 Cross section of ^{157}Gd(n, el): DANCE vs. ENDF/B-VII. 84

Figure 3.18 ^{89}Y(n, γ) measured for the 1 mil thin target with DANCE. 86

Figure 3.19 ^{89}Y(n, γ) measured for the 5 mil medium target with DANCE. 86

Figure 3.20 ^{89}Y(n, γ) measured for the 25 mil thick target with DANCE. 86

Figure 3.21 ^{89}Y(n, γ): DANCE vs. evaluated data libraries. 88

Figure 3.22 ^{89}Y(n, γ): DANCE vs. other experimental data. 88

Figure A.1 Spin assignment for $J = 1$ resonances. E_n spectra of $M_1 = 3$ vs. $M_2 = 4$. . 96

Figure A.2 Spin assignment for $J = 1$ resonances. E_n spectra of $M_1 = 3$ vs. $M_2 = 5$. . 97

Figure A.3 Spin assignment for $J = 1$ resonances. E_n spectra of $M_1 = 3$ vs. $M_2 = 6$. . 98

Figure A.4 Spin assignment for $J = 1$ resonances. E_n spectra of $M_1 = 4$ vs. $M_2 = 5$. . 99

Figure A.5 Spin assignment for $J = 1$ resonances. E_n spectra of $M_1 = 4$ vs. $M_2 = 6$. . 100

Figure A.6 Spin assignment for $J = 1$ resonances. E_n spectra of $M_1 = 5$ vs. $M_2 = 6$. . 101

Figure A.7 The 21.65-eV resonance vs. the prototype 20.56-eV resonance. 102

Figure A.8 The 23.33-eV resonance vs. the prototype 20.56-eV resonance. 102

Figure A.9 The 25.4-eV resonance vs. the prototype 20.56-eV resonance. 102

Figure A.10 The 40.17-eV resonance vs. the prototype 20.56-eV resonance. 102

Figure A.11 The 44.22-eV resonance vs. the prototype 20.56-eV resonance. 102

Figure A.12 The 48.8-eV resonance vs. the prototype 20.56-eV resonance. 102

Figure A.13 The 53.38-eV resonance vs. the prototype 20.56-eV resonance. 103

Figure A.14 The 66.65-eV resonance vs. the prototype 20.56-eV resonance. 103

Figure A.15 The 81.48-eV resonance vs. the prototype 20.56-eV resonance. 103

Figure A.16 The 82.3-eV resonance vs. the prototype 20.56-eV resonance. 103

Figure A.17 The 87.46-eV resonance vs. the prototype 20.56-eV resonance. 103

Figure A.18The 96.59-eV resonance vs. the prototype 20.56-eV resonance. 103

Figure A.19The 100.2-eV resonance vs. the prototype 20.56-eV resonance. 104

Figure A.20The 105.3-eV resonance vs. the prototype 20.56-eV resonance. 104

Figure A.21The 107.7-eV resonance vs. the prototype 20.56-eV resonance. 104

Figure A.22The 110.5-eV resonance vs. the prototype 20.56-eV resonance. 104

Figure A.23The 115.4-eV resonance vs. the prototype 20.56-eV resonance. 104

Figure A.24The 120.9-eV resonance vs. the prototype 20.56-eV resonance. 104

Figure A.25The 137.9-eV resonance vs. the prototype 20.56-eV resonance. 105

Figure A.26The 143.54-eV resonance vs. the prototype 20.56-eV resonance. 105

Figure A.27The 148.4-eV resonance vs. the prototype 20.56-eV resonance. 105

Figure A.28The 156.38-eV resonance vs. the prototype 20.56-eV resonance. 105

Figure A.29The 164.38-eV resonance vs. the prototype 20.56-eV resonance. 105

Figure A.30The 171.18-eV resonance vs. the prototype 20.56-eV resonance. 105

Figure A.31The 183.76-eV resonance vs. the prototype 20.56-eV resonance. 106

Figure A.32The 190.58-eV resonance vs. the prototype 20.56-eV resonance. 106

Figure A.33The 194.37-eV resonance vs. the prototype 20.56-eV resonance. 106

Figure A.34The 202.69-eV resonance vs. the prototype 20.56-eV resonance. 106

Figure A.35The 205.35-eV resonance vs. the prototype 20.56-eV resonance. 106

Figure A.36Spin assignment in the range E_n = 18 – 28 eV. 107

Figure A.37Spin assignment in the range E_n = 32 – 67 eV. 107

Figure A.38Spin assignment in the range E_n = 73 – 112 eV. 108

Figure A.39Spin assignment in the range E_n = 113 – 180 eV. 108

Figure A.40Spin assignment in the range E_n = 180 – 285 eV. 109

Figure A.41Spin assignment in the range E_n = 285 – 430 eV. 109

Figure A.42Spin assignment in the range E_n = 440 – 670 eV. 110

Figure A.43^{157}Gd resonances in the range E_n = 10 – 70 eV. 110

Figure A.44^{157}Gd resonances in the range E_n = 70 – 200 eV. 111

Figure A.45^{157}Gd resonances in the range E_n = 200 – 500 eV. 111

Figure A.46^{157}Gd resonances in the range E_n = 500 – 1600 eV. 111

Chapter 1

Hardware

1.1 Introduction

The neutron capture measurements were performed at the Los Alamos National Neutron Science Center (LANSCE), Lujan center, flight path 14 (FP14). The LANSCE linac produces a proton beam of 800-MeV energy. It is accumulated in the proton storage ring (PSR) and is injected into the tungsten neutron production target located in the Lujan center. Then the newly created neutron beam is moderated through water moderators. The moderated neutron beam is collimated on FP14 of the Lujan center with a series of steel and lead collimators. At the end of FP14 the Detector for Advanced Neutron Capture Experiments (DANCE) and its data acquisition systems are located. FP14 ends with the beam stop.

In this section I will describe the hardware and instruments involved in the neutron capture measurements on ^{157}Gd and ^{89}Y.

1.2 LINAC at Los Alamos Neutron Science Center (LANSCE)

The linear accelerator (linac) at LANSCE (see Fig. 1.1) is a proton beam production facility. The linac building alone is approximately 0.5 miles long. The initial energy of the ions injected into the accelerating section is 750 keV. Following the ion injection, the beam is chopped with respect to the linac phase. Then it is accelerated up to 100 MeV in

the drift-tube section, which is 62-m long and operates at 201-MHz repetition rate. The next accelerating section is a side-coupled section, which works at a 805 MHz rate and contributes the majority of the beam acceleration. The maximum energy of the proton beam is 800 MeV. See [2] for more details.

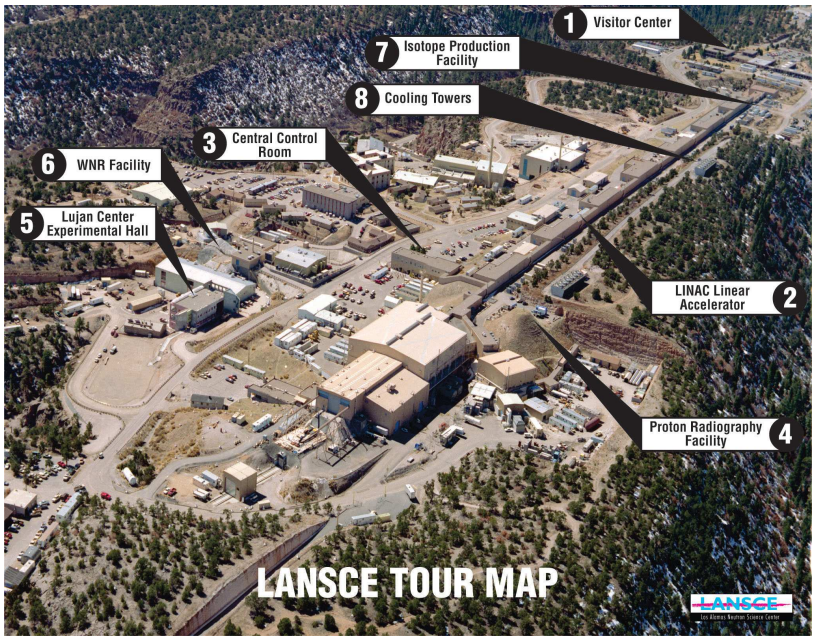

Figure 1.1: An aerial view of LANSCE.

The timing of the proton beam burst is such that it consists of 825 μs macropulses. The repetition rate of the macropulses is 120 Hz. In turn, the macropulse consists of micropulses that are 100 ps long. Each micropulse contains approximately 10^8 protons. The linac accelerates protons to different energies, but only those in the vicinity of 800 MeV are selected and transported into the proton storage ring (PSR).

The PSR accepts proton macropulses at a 20-Hz rate. The 450-μs proton macropulses, made of micropulses spaced every 5 ns, are injected into the PSR. The macropulses wrap around the PSR at a rate of 20 Hz, until the end of the macropulse. The accumulated protons are transported from the PSR into the neutron production target located in the Lujan center at a rate of 20 Hz. The time spread of a macropulse after the PSR is 250 ns, and the average current of the proton beam after the PSR lies in the range 90 – 100 μs.

1.3 Spallation Neutron Source, Lujan Center, Flight Path 14

The 800-MeV proton beam is used to produce neutrons in the energy range from thermal to MeV. The proton beam is compressed in the PSR into 750 μm pulses of 125 ns FWHM at a repetition rate of 20 Hz. Then the proton beam is injected into the Spallation Neutron Source (SNS) located at the ER1 building adjacent to the Lujan Center.

The main element of the SNS is the neutron production target [3]. It consists of 2 cylinders made of natural tungsten (^{nat}W). Because of a very high radiation load on the W-target, it is extensively cooled with water, which also serves as a moderator for newly created neutrons. The proton beam strikes the W-target vertically. The tungsten material was chosen because of the high neutron output: one 800-MeV proton can produce up to 17 neutrons. The W-target assembly is surrounded with the backscattering moderator system, thus increasing the peak neutron flux. The backscattering system consists of beryllium (Be), lead (Pb), and steel (Fe). See Fig. 1.2 for a plane view of the SNS vertical cross section.

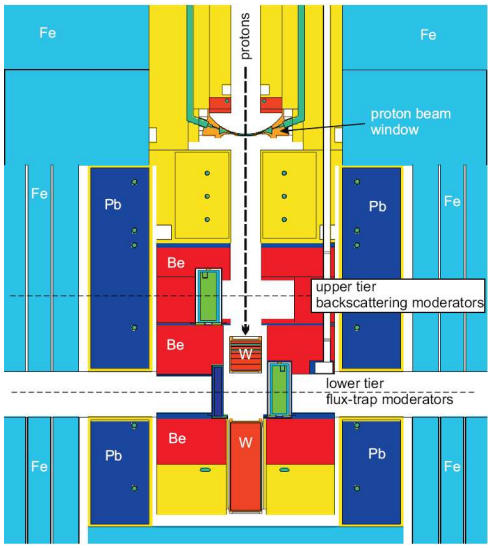

Figure 1.2: Vertical cross section of SNS, with W – tungsten target and Be, Pb, Fe backscattering system.

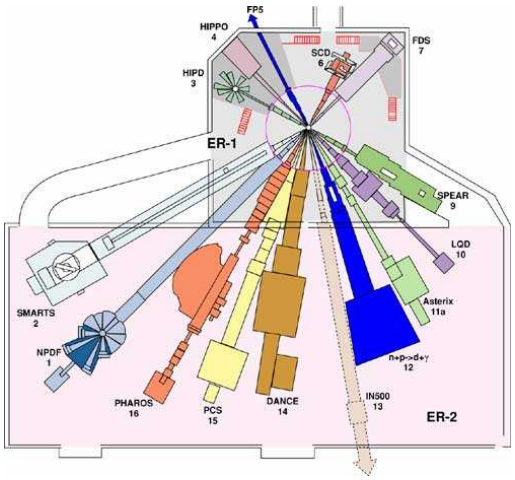

Figure 1.3: The Lujan center flight paths; DANCE is at FP14.

The Lujan Center is designed for neutron scattering measurements that are important for:

- material science and engineering;

- polymer science;
- chemistry;
- earth science and geology;
- structural biology;
- condensed matter physics;
- neutron nuclear science and transmission spectroscopy.

DANCE is located on flight path 14 (FP14) of the Lujan center. The moderated neutron beam has many exits from SNS, one of them enters FP14. The distance the neutrons travel between SNS and the target inside DANCE is approximately 20.3 m, see Fig. 1.4.

The series of copper and borated polyethylene collimators in FP14 shape neutrons into a circular beam of 1.0-cm diameter. Most of the aluminum beam pipe from SNS to DANCE has no vacuum maintened in it. Then the neutron beam enters the DANCE cave, where a 0.05-torr vacuum is maintained inside the beam pipe that goes through DANCE. Normally a target is installed in this section of the beam pipe. It is always under vacuum when the beam is on, although some radioactive targets can be measured without both the beam and vacuum. The last part of FP14 is a few meter section of the beam pipe downstream after DANCE and its beam monitors, and it ends with the concrete beam stop. Also the control room with the data acquisition system is located next to the DANCE cave.

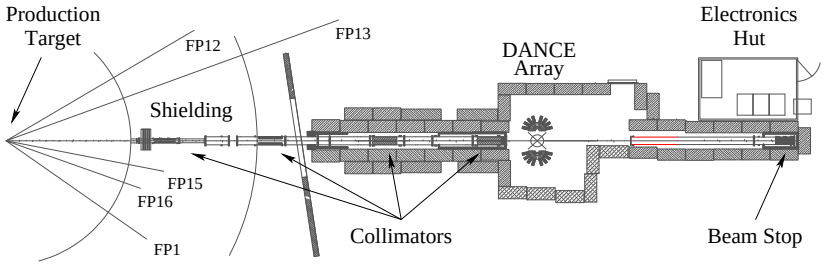

Figure 1.4: Scheme of FP14 at the Lujan center.

1.4 Time-of-Flight (TOF) technique

It is absolutely essential for capture experiments to measure the incident neutron energy as precisely as possible. The time-of-flight (TOF) technique is used at FP14 to determine the energy of each neutron that hits the detector. For FP14 we assume that neutrons are non-relativistic up to 1-MeV. The flight path length L_{FP14} is 20.25 m from the water moderator to the target locaated inside DANCE. The arrival time T_n of the incident neutron is the time between a trigger signal from the proton beam and a signal from DANCE detecting the first event within one beam burst, which has a repetition rate of 20 Hz. The incident neutron energy in this simplified case is

$$E_n = \frac{m_n V_n^2}{2} = \frac{m_n}{2}(\frac{T}{L})^2 \tag{1.1}$$

where V_n is the incident neutron speed and m_n is the neutron mass.

Because of the uncertainties in T and L, this formula defines only an approximate neutron energy for FP14. If no corrections are made, the measured ^{157}Gd resonance energies are shifted relative to those in the ENDF/B-VII data base. The differences can be, for example, as large as 0.2 eV for the 20.5-eV resonance, i.e., $\sim$1%. The uncertainty in the T determination is caused by

- time delays due to finite lengths of cables where electrical signals travel through (from SNS to DANCE, from DANCE to its data acquisition, etc),
- the fact that the TOF trigger is linked to the proton beam, rather than to the moment when the neutron created in SNS leaves the light water moderator and enters FP14.

The L parameter has also some uncertainty, the main contribution of which comes from the geometrical size of the moderator. L is the distance between the center of the moderator, where neutrons are created, and the target inside DANCE. Neutrons are created throughout the volume of the W-target rather than only at the center. Since the proton beam has an energy of 800 MeV, most neutrons are fast. Before entering FP14 neutrons scatter inside SNS and are moderated with water. Thus in reality neutrons of the same energy can come from both the adjacent and opposite to FP14 sides of the water moderator. Therefore incident neutrons of the same energy are spread in time, which introduces uncertainties in the TOF assumption that the neutron energy is determined from arrival time. Since

technically it is very challenging to define ΔL, this uncertainty can be translated into ΔT in Eq. 1.1. The lower the incident neutron energy, the larger relative uncertainty $\frac{\Delta T}{T}$. The total uncertainty in incident neutron energy ΔE_n can be propagated from Eg. 1.1:

$$\Delta E_n = 2E_n\sqrt{(\frac{\Delta L}{L})^2 + (\frac{\Delta T}{T})^2}. \tag{1.2}$$

As mentioned above, it is impossible to determine ΔL precisely, so the appropriate corrections for ΔT is made in Eq. 1.1 in order to compensate for both ΔL and ΔT uncertainties. The actual formula used in the incident neutron energy calculation is

$$E_n = \frac{m_n}{2}(\frac{T + \Delta T}{L})^2 \tag{1.3}$$

where ΔT is an empirical correction for T, defined so the measured resonance energies of ^{1}97Au are as close the ENDF/B-VII data as possible in the neutron energy range of 0.025 eV – 300 keV. For neutrons in the T = 300 to 500 μs time-of-flight range, the correction varies from ΔT = 200 to 400 ns. This helps to reduce the energy uncertainty in the 20.5 eV ^{157}Gd resonance from 0.2 eV down to 0.05 eV.

1.5 DANCE array

The Detector for Advanced Neutron Capture measurement (DANCE) (see Fig. 1.5) is installed at the end of FP14, in the so-called DANCE cave, before the beam stop. DANCE was designed in order to measure neutron capture better in many aspects than any previous system.

Any neutron capture detecting system, including DANCE, has some requirements [6] to maximize the output of (n, γ) events and to minimize different kinds of background. These requirements include:

- high detector efficiency for γ-rays for up to 16 MeV, which allows the collection of pileup data ;
- low detector efficiency for neutrons to minimize background from neutron scattering reactions. For example, NaI and CsI are excluded because of the large ^{127}I(n, γ) cross section;

- energy resolution good enough to distinguish individual γ-rays in a cascade, typically $\frac{\Delta E_\gamma}{E_\gamma} = 0.15$–$0.2$ is sufficient;
- timing resolution good enough to collect data from each (n, γ) event, since during TOF measurements neutrons with a wide of energies produce events within a relatively short time period;
- segmentation of detectors to reduce the count rate per detector.

In order to design DANCE to perform better than any other similar system (n_TOF for example [5]) all of these requirements have to be satisfied. DANCE is an assembly of 160 detectors that form an enclosed sphere (see Fig. 1.7), thus maximizing efficiency via usage of the 4π-geometry. 2 detectors are removed for the beam pipe that goes through DANCE; the effective solid angle of DANCE coverage is $\sim 3.52\pi$. Each crystal (see Fig. 1.6) is wrapped with a PVC, 0.7-cm thick light isolating foil.

Each DANCE detector contains a BaF_2 scintillator crystal. BaF_2 was chosen for its light output. Its pulse height response can be separated into two components, slow and fast. Using the pulse shape discrimination (PSD) technique it is possible to reject α-background.

Table 1.1: Isotopic abundances in ^{nat}Ba.

Isotope	Abundance [%]
^{130}Ba	0.106
^{132}Ba	0.101
^{134}Ba	2.417
^{135}Ba	6.592
^{136}Ba	7.854
^{137}Ba	11.232
^{138}Ba	71.698

Table 1.2: Energies [MeV] of Ra decay chains. The ^{226}Ra decay chain is dominant; 5 α-lines are used to calibrate DANCE for γ-energies.

^{226}Ra-^{206}Pb	^{228}Ra-^{208}Pb
4.784	5.423
5.304	5.685
5.489	6.288
6.002	6.340
7.686	6.778
	8.785

Natural barium consists of 7 stable isotopes (Table 1). Also ^{nat}Ba always has some level of ^{nat}Ra impurity; ^{nat}Ra is a chemical homologue of ^{nat}Ba, which makes the BaF_2 crystals radioactive with the approximate rate of 0.2 $\frac{Bq}{cm^3}$. ^{nat}Ra has two radioactive isotopes, ^{226}Ra and ^{228}Ra. They decay through two chains that end up at ^{206}Pb and ^{208}Pb, respectively (Table 1). The products of these radioactive decay chains include γ-rays and α-particles, which contribute to an ambient background. Using the pulse shape

discrimination technique, α-particles can be separated from γ-rays. This α-activity can be used to track γ-energy calibration of DANCE for changes due to temperature variations during measurements. This makes the α-activity in the BaF_2 crystal beneficial for DANCE.

One of the main requirement for DANCE is high efficiency. In addition a high segmentation is required in order to reduce the count rate per crystal; because of high count rate a dead time issue at some point makes the data analysis impossible and can spoil the entire data set. To satisfy these requirements all of the BaF_2 crystals have an equal volume, are 17 cm long, and each crystal covers the same solid angle from the target view point. There are 4 different crystal shapes, arranged into a soccer ball like system. The crystals form an enclosed sphere. Each crystal is in optical contact with an individual photomultiplier tube.

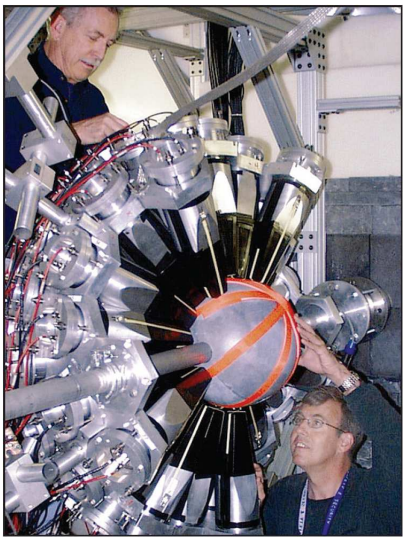

Figure 1.5: DANCE array.

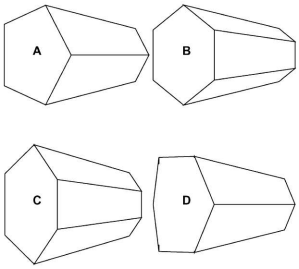

Figure 1.6: DANCE is built from crystals of 4 shapes: 12 of type A, 30 of type B, 60 of type C, and 60 of type D.

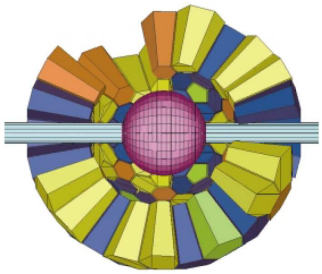

Figure 1.7: DANCE cutaway scheme.

The purpose of DANCE is to measure γ-rays from the neutron capture reaction (n,γ), and one of the major backgrounds in DANCE experiments is from the neutron scattering reaction (n,el); port of the neutrons scattered from the target make it to the BaF_2 crystals. To eliminate neutrons scattered from the target while letting γ-rays pass, a ^{6}LiH sphere surrounds the target inside DANCE. The ratio $\frac{\sigma(n,tot)}{\sigma(\gamma,tot)}$ in ^{6}LiH is larger than in any other available material with similar properties; due to large $^6\mathrm{Li}(n,\alpha)$ cross section

neutrons are eliminated without γ-background. The ^{6}LiH shell is a sphere of 36-cm diameter with a 24-cm hollow sphere inside, so the thickness of the shell is 6 cm.

1.6 Neutron beam monitors

For calculating the (n, γ) cross section one needs to know the characteristics of the incident neutron beam that bombards the target. 3 separate neutron beam monitors are installed at FP14, as well as 1 monitor of the ambient neutron background inside the DANCE cave.

The first beam monitor downstream after the target is the so-called Si-Li detector. At approximately 2 m downstream from the DANCE target, the ^{6}LiF foil of 2-μm thickness and 3x4 cm^2 deposited on the 8-μm thick capton foil is located in the center of the beam pipe at exactly 45° to the incident neutron beam. A vacuum is maintained at the foil location. That foil is used because of the $^6\mathrm{Li}(n,t)^4\mathrm{He}$ reaction, and tritons and α-particles are detected with the n-type Si surface barrier detector which is placed close to the ^{6}LiF foil, ∼5 cm away from the beam.

The second beam monitor is located 4 cm after the Si-Li one, outside the vacuum section of the beam pipe. It is an ionization gas chamber with thin capton windows, and is filled with BF_3+Ar gas at a pressure of approximately 1 atm. The amount of Ar is small comparing to BF_3. The reaction used here is $^{10}\mathrm{B}(n,\alpha)^7\mathrm{Li}$. Despite the close proximity of the Si(Li) beam monitor, charged particles coming from it do not interfere with the BF_3 readings; there is an aluminum window of the beam pipe between these two beam monitors.

The third and the last beam monitor is behind the BF_3 detector. It is a fission chamber that has a ^{235}U sample inside and filled with P-10 gas. The uranium sample in the center of the chamber is shaped into a uniform cylinder, ∼50-mg total mass, 6.99-cm sensitive diameter, 1.3-$\frac{mg}{cm^2}$ thickness. The fission reaction $^{235}\mathrm{U}(n,f)$ is used to produce and detect fission fragments and thus to determine the neutron flux. The ^{235}U detector can deal with a higher count rate than BF_3 and Si(Li) beam monitors because the ^{235}U detector has smaller efficiency.

A background monitor is also installed inside the DANCE cave. It is a Li_6-glass detector, located at ∼1.5-m distance from DANCE. This detector monitors changes of the neutron background inside the DANCE cave. Increases in fast neutron readings inside the

Lujan center do occur rarely when the proton beam goes out of alignment and hits the beam pipe just before entering SNS.

1.7 Data acquisition system

DANCE is a system made of 160 detectors, since many detectors generate data from every event the DANCE data rate can be really large. In fact, when measuring targets with large (n, γ) or (n, el) cross sections, thick or radioactive targets, etc, the data rate can exceed 1 raw Terabyte per day. In addition the beam monitors produce data at an approximate rate of several Gigabytes per hour. In order to cope with such a high data rate, an appropriate data acquisition (DAQ) was built. DAQ is a complex system [7] that includes a network of specialized hardware (computers) and software that are specifically designed to collect signals from DANCE photomultiplier tubes (PMT), sort the raw binary data, perform on-line data reduction, and record it on hard drives (HDD) with the MIDAS [10] format for further off-line analysis. The acquisition software is also responsible for synchronizing all of the DAQ computers, and it is critical for DAQ to be synchronized within milliseconds.

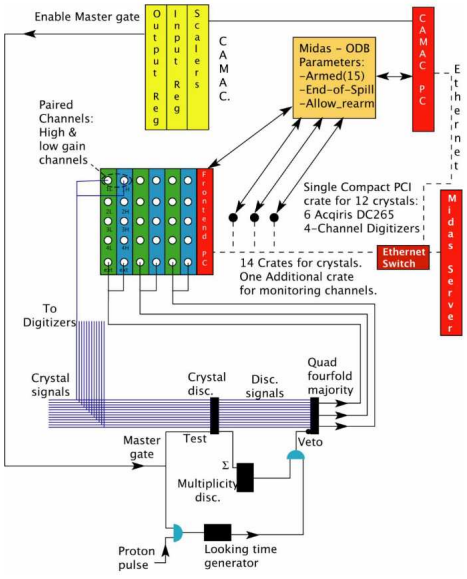

Figure 1.8: Scheme of acquisition hardware.

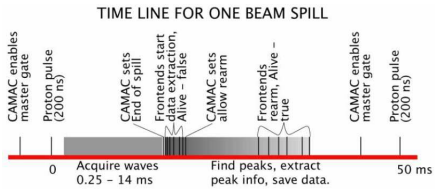

Figure 1.9: Sequence of events in one beam pulse.

In order to extract as much information as possible, a signal from each PMT is split

into two Acqiris 4-channel DC256 digitizers [8]. The digitizers sample each signal waveform at a rate of 500 MHz, which is 2 ns/point, each point is recorded with 8 bit resolution (see Fig. 1.8). Each digitizer channel is equipped with 128 Kbytes of fast memory. Depending on experimental conditions and the desired results, two operating modes can be used:

- Continuous mode. The signal from the proton beam after a fixed time triggers all the digitizers simultaneously and they collect data for a preset amount of time. For the ^{89}Y experiment it was 250 μs. This mode is used to cover a neutron TOF up to $2 \cdot 250 = 500$ μs and has no dead time issues. The factor of 2 comes from the fact that 2 digitizers sample signals from 1 PMT.

- Sequential (segmented) mode. Whenever 2 or more detectors fire above the 50-mV threshold within the 100 ns time coincidence window, the corresponding digitizers are triggered externally with the NIM hardware, and the remaining digitizers remain dead till the end of the cycle. The number of detectors that trigger, a so-called crystal multiplicity gate, must be at least 2. In this mode neutrons with TOF up to 14 ms are covered, but it has a preset dead time of 2.5 μs, which is corrected later in off-line analysis.

The difference between these two modes is the neutron energy range covered, the segmented mode enables to measure neutrons down to thermal energies, and a dead time issue, it is present in the segmented mode. For many experiments data is collected using both modes separately. In the segmented mode the 3.5 μs dead time is introduced to cut noise before each signal resulting from a physical event.

The beam rate is 20 Hz, so DAQ has roughly 40 ms to read out all of the necessary digitizers, perform on-line analysis to extract waveform information, and to send the data to the central computer that runs the `mserver` program. It coordinates the work of frontends, builds events from the raw data and records data to hard drives with the MIDAS format. After 50 ms, 40 of which are spent to collect, analyze, and record data, DAQ has 10 ms to rearm digitizers for the next beam pulse. In order to achieve the necessary broad band the digitizers are arranged into 14 parallel PCI crates, each crate serves 6 digitizers, and thus handles 12 DANCE PMTs. Each crate contains the digitizer and the computer (frontend) based on an Intel 1.8 GHz CPU that works under RedHat Enterprise Linux OS [9]. The computers run the frontend programs written with Midas 1.9.5 framework [10],

which perform an online analysis and data reduction. Then the data is sent to the computer that combines the data from multiple frontends into a single stream and records it to HDD. The Midas `mhttpd` task program is used to monitor and control the DAQ operation via a web interface. Once the on-line analysis is complete the data is sent to the 15-Terabyte RAID (Redundant Array of Independent Disks), from there the data is backed up to another 15-Terabyte RAID.

1.8 Pulse shape discrimination

DANCE is capable of producing a huge amount of data that must be reduced before recording it to HDD. The best way to decrease amount of data is to include only the most useful information at every possible analysis stage. The very first off-line analysis starts with the pulse shape discrimination (PSD) technique of the PMT signal waveform.

The signal waveform that comes from a PMT is divided into two parts – the so-called fast and slow components (see Fig. 1.10). The very first task is to detect the leading edge of the waveform. Every 10 ns the amplitudes of two digitized points are subtracted and the difference is divided by the 2 ns time bin. Thus the slope of the waveform is determined within every 5 waveform points. When this slope exceeds a preset threshold (typically 50 mV), which is determined by the `CFD` software (Constant Fraction Discriminator), the frontend software detects the leading edge. This is used to separate signals from noise.

The digitizer (one channel per crystal) samples waveforms with a 2 ns increment into 32 points, a total of 64 ns. These data are identified as the fast component. Then it samples the second part of the waveform (after 32 points of the fast component) in 5 sections, each for 100 points, or a total of $5 \cdot 200 = 1000$ ns. These data are identified as the slow component. The identification of these components is done later in an off-line analysis, for now digitizer just samples waveforms and record amplitude (mV) and time (ns) for each 2 ns point.

The BaF_2 crystals are designed to detect γ-rays with a high efficiency, but they also have internal α-activity from the ^{226}Ra–^{206}Pb radioactive decay chain. The ^{228}Ra–^{208}Pb decay is negligible in BaF_2. The light output of the BaF_2 crystal depends on the energy deposited and the type of particle. The two waveforms in Fig. 1.11 correspond to two different particles, γ and α. The ratio of the integrals $\frac{I_{fast}}{I_{slow}}$ depends on the type of

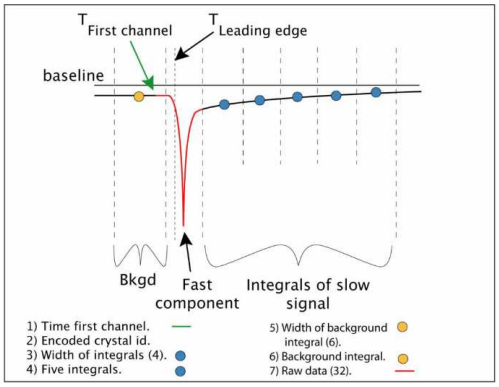

Figure 1.10: PMT Waveform– fast and slow components are digitized with 2 ns increments.

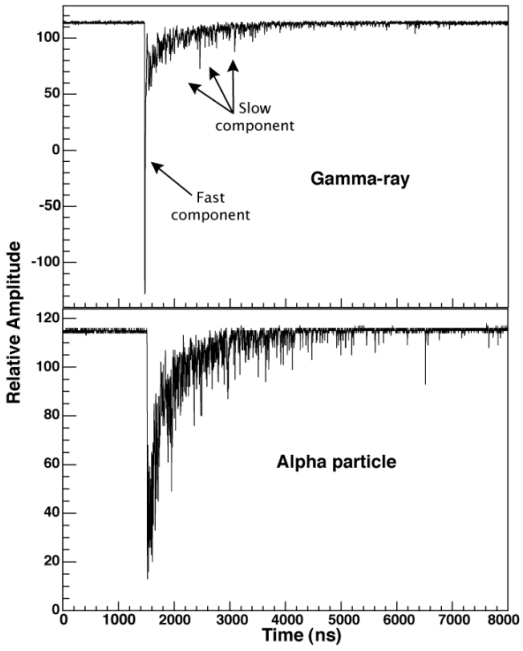

Figure 1.11: PMT waveforms for gamma rays and alpha particles.

particle and the deposited energy. Thus using PSD one can identify particles and separate α-background from γ-rays.

The same PSD technique is applied to the waveform of the beam monitors, with the only difference is a time increment, which is 50 ns for beam monitors vs. 2 ns for DANCE crystals. Although there is no slow component, it is being read as a fast one for 32 points, as well as the 500 points of the slow component. It is performed in this way in order to simplify the on-line analysis, since beam monitors are considered to be 4 additional DANCE channels and their data is processed in the same way as for DANCE crystals, except for the time increment when sampling waveforms.

1.9 Raw data overview

Digitized data of each waveform and added by the frontend data contain information about amplitude, time, crystal ID, etc. For example, the waveform is integrated with $32 + 5 \cdot 100 = 532$ points, total of $532 \cdot 2ns = 1.064\mu s$, and this is done for 160 DANCE crystals and 4 beam monitors (in continuous mode). So the raw data includes

$532 \cdot (160 + 4) = 87248$ multiple entry records from every single beam spill with a rate of 20 Hz. This is 1.7 million records per second, or 6.28 billion records per hour, and each record contains hundreds of bytes of data. This simple estimate indicates that the raw data rate during experiments is huge, and for some targets it can be as large as 1 Terabyte per day. In order to decrease the amount of data for storage on HDDs, both on- and off-line analyses are performed (see Fig. 1.12).

In general the raw data is processed in several major steps:

- On-line calculation of the total raw integrals of each waveform acquired during a neutron beam spill, then baseline subtraction, and determination of the TOF value of each signal for each crystal.
- Then physical events are built.
- Then both the energy and time calibrations are performed, which allows the data to be quantified such that a physical analysis becomes possible.
- From the calibrated data the physical quantities can be calculated and energy spectra built.
- The rest of the analysis is performed based on energy spectra. This includes gating on E_n, E_γ, and multiplicity, subtracting background and contaminants, determining the neutron beam flux, cross sections, resonance spins, etc.

If the data are processed at least through the first two steps, a typical one-week experiment on a non-radioactive target can be compressed into several hundred Gigabytes of data. The data is collected and stored on a run increment basis, with the run time determined by the data rate, typically 1 run contains 1 Gigabyte of data. For example, 1 run of the ^{89}Y data contains 50 minutes of measurements, in contrast the radioactive ^{176}Lu target produces a similar run of data every 4 minutes, which corresponds to $\sim 10^8 \frac{events}{sec}$. Breaking data into runs is important in terms of reliability when performing measurements and flexibility when analyzing data. Should a hardware glitch or a software error occur, only the corresponding data run will be wasted,and the rest of the data remains intact.

To handle DANCE data, a special software framework was written and is under constant development and modification. ROME builder (from Paul Scherrer Institute),

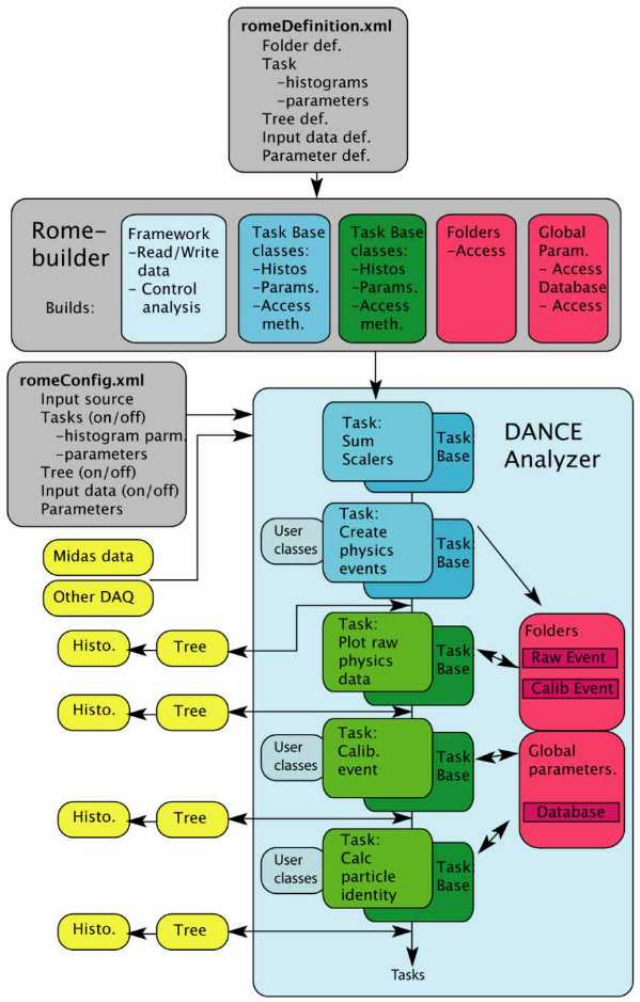

Figure 1.12: Schematic view of the raw data analysis.

which is based on the ROOT framework (from CERN), provides an interface where one can write software for graphing different experimental aspects and parameters (see Fig. 1.12). The analysis of the DANCE data can be separated into different tasks – for each task a C++ application must be developed using ROOT [11]. These tasks are independent from each other.

Chapter 2

^{157}Gd Experiment

2.1 Introduction

Gadolinium [13] is of interest in different areas of science and technology. ^{157}Gd has the highest thermal neutron capture cross section of any known nuclide with the exception of ^{135}Xe, but ^{135}Xe also has a fast burn-out rate inside operating nuclear reactors, which limits its usefulness as a nuclear control rod material. Gadolinium has applications in nuclear reactors as a burnable poison. It is also used as a secondary, emergency shut down measure in some types of nuclear reactors, for example in the CANDU [15] type.

Another point of interest is nuclear structure. It might be possible to study the systematics of behavior of the scissors mode resonance as a function of mass and deformation, since Gd has 7 stable isotopes. Better resonance spectroscopy may help to improve the level density and, thus, strength functions, are essential in calculating nuclear reaction rates.

2.2 Neutron capture measurements on ^{157}Gd

For the DANCE neutron capture measurements on ^{157}Gd two targets were used – one the ^{157}Gd target (on a Be backing) and a ^{9}Be target. Since ^{9}Be is used as a backing plate for the ^{157}Gd deposition, an additional measurement on ^{9}Be alone is necessary to account for the corresponding background created by the neutrons scattered from beryllium.

2.2.1 The ^{157}Gd and ^{9}Be targets

The element gadolinium has Z = 64, belongs to the lanthanide group in the periodic table and has 7 stable isotopes with atomic number A = 152, 154, 155, 156, 157, 158, and 160. The ^{157}Gd target used in the neutron capture measurements with DANCE was enriched to 99.7% ^{157}Gd. The isotopic composition of the target is listed in Table 3 along with the composition of natural gadolinium.

Table 2.1: Percent composition of the ^{157}Gd target and of natural Gd.

Isotope	Target [%]	Natural [%]
^{152}Gd	<0.01	0.2
^{154}Gd	<0.01	2.18
^{155}Gd	0.08	14.8
^{156}Gd	0.09	20.47
^{157}Gd	**99.7**	**15.65**
^{158}Gd	0.12	24.84
^{160}Gd	<0.01	21.86

The ^{157}Gd target (Fig. 2.1) was fabricated at the Lawrence Livermore National Laboratory [12] (LLNL). The target has several components. The thin beryllium foil is sturdy enough to support the deposited ^{157}Gd isotope, and is glued to the ring frame made of natural aluminum. The aluminum ring is inserted into a short aluminum cylinder (Fig. 2.2) that serves as a sample holder, and it is placed in the neutron beam pipe. The ^{157}Gd isotope was deposited by the electroplating method onto the ^{9}Be backing foil. The deposition is a circular spot of 7-mm diameter. The thickness of the ^{157}Gd deposition is known approximately – averaged throughout the entire area it is $\sim$0.8 $\frac{mg}{cm^2}$. However, it is highly non uniform, with a difference between deposition thicknesses on the edges and the center of up to a factor of 4. Uniformity of the target deposition is required to determine the absolute ^{157}Gd(n,γ) cross section. The cross section can also be determined by normalization of the ^{157}Gd(n,γ) cross section relative to some well known resonance from evaluated nuclear data, for example ENDF/B-VII. The ^{157}Gd isotope was deposited on the ^{9}Be backing foil. Although this foil material has a relatively small neutron capture cross section, the foil is much thicker than the ^{157}Gd deposition. The beryllium created a significant background, which is mostly from neutrons scattered from beryllium and less so from neutron capture on beryllium. Since these backgrounds must be accounted for, a

blank Be foil was studied. The ^{9}Be target is a self-supporting foil (Fig. 2.1) that is mounted onto the same target holder (Fig. 2.2) as the Gd target.

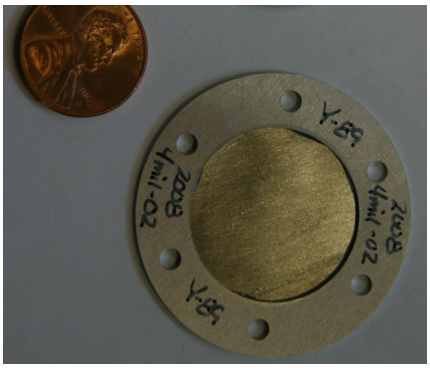

Figure 2.1: ^{89}Y target.

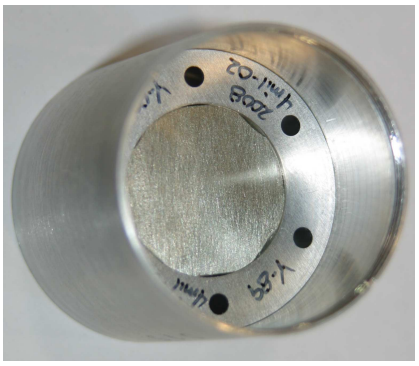

Figure 2.2: Aluminum target holder.

2.2.2 Experimental setup

The aluminum target holder with the ^{157}Gd target was placed inside the beam pipe, precisely in the center of DANCE. During the Gd measurements this section of the beam pipe was under a vacuum of ∼50 mtorr (1 torr = 1/760 bar = 133.322 Pa). The incident neutron beam hits the ^{157}Gd target and after passing through the target reaches the beam monitors. γ-rays from the ^{157}Gd(n,γ) reaction are detected in the DANCE crystals, as well as other products from different reactions. These include γ-rays that are present in the neutron beam and neutrons that scatter from the ^{157}Gd target and the ^{9}Be backing and are captured in the BaF_2 crystals.

The data were collected using both the continuous and segmented modes of the DANCE data acquisition system. The continuous mode allows the collection of data down to $\sim$ 10 eV neutron energy. The segmented mode has limitations due to a dead time issue and the highest count rate the data acquisition system can cope with. This mode is used primarily for extending the neutron energy range down to 10^{-1} eV. The beam time was divided approximately equally between the two modes: 3 days of measurement for each mode, with 0.5 day of the beam time were dedicated to the ^{9}Be blank measurement.

During the ^{157}Gd experiment a high background was encountered. This background was due to the proton beam, which went out of alignment during the ^{157}Gd measurement and grazed the beam pipe before entering the SNS. The 800-MeV protons caused

a significant increase in the ambient γ-background level inside the Lujan center, which created some challenges in the data analysis process.

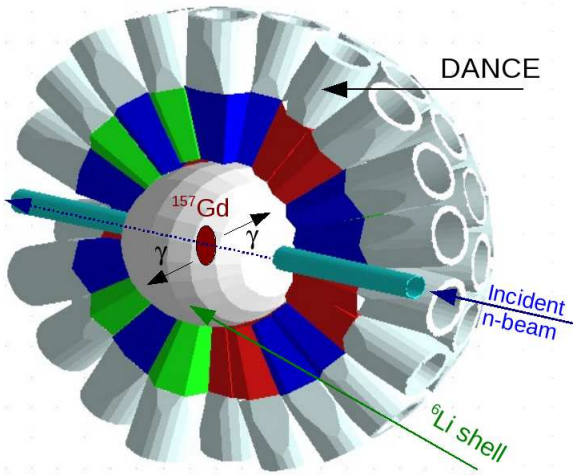

Figure 2.3: Scheme of ^{157}Gd experiment.

2.3 Data analysis

DANCE is capable of generating a huge amount of raw binary data. At the on-line analysis the data is reduced and compressed into a special binary MIDAS format. Since the structure of the MIDAS format [10] is basically irrelevant for the data analysis it will not be discussed. The data structure and the analysis as applied to the ^{157}Gd data will be described.

2.3.1 Raw cluster data

After DANCE data is reduced on-line, the data are recorded to HDD with the special binary MIDAS format [10]. Each MIDAS file is compressed with the `gzip` compression utility [16]. This binary format of recording and compressing data is adopted for the purpose of minimizing the disk space required to store the data. The compression ratio of the raw generated data can be as large as 30%. After detecting and on-line processing of a single event, the following information is recorded to HDD for further off-line analysis:

- a time stamp of the waveform leading edge from the firing crystal. In the continuous mode this time is relative to the proton beam time trigger, while in the segmented mode the time is relative to the T0 time stamp;
- digitized points of the waveform from a firing crystal with the 2 ns time increment – 32 points for the fast component and 5 times 100 = 500 points for the slow component;
- the ID of the firing crystal.

This raw data format is the same for both the DANCE crystals and the neutron beam monitors, with the only difference a detector ID. For the DANCE crystals the ID range is 0 to 161, and for the beam monitors it is 170 to 173.

During the ^{157}Gd experiment the recorded data rate was $\sim$ 2 Gigabyte per hour in the continuous mode and $\sim$3 Gigabyte per hour in the segmented mode for the Gd target. For the Be target the data rate was smaller, $\sim$1 Gigabyte per hour, since the Gd target includes both the Gd target material and the Be backing. The data rate in the segmented mode is higher than in the continuous mode because this mode covers a wider neutron energy range – down to 10^{-1} eV in the segmented mode, where the neutron flux is greatest, versus 10^{1} eV in the continuous mode.

MIDAS files are recorded for each run separately. The size of the run file is a compromise between convenience and data integrity. The main advantage of such a data structure is reliability. In case of problems the data are affected only for the duration of a particular run or set of runs, while the data taken before these problems is not affected. Also small portions of the data can be analyzed quickly during the experiment in order to perform necessary checks, evaluate the data quality, and if necessary to made changes in the experimental schedule – usually to redistribute beam time among different targets and/or to measure new targets that might help to deal with background issues. The discrete data format also allows chronological tracking of hardware and software related problems during the experiment. Another advantage of this procedure is to overcome computer limitations of handling very large amounts of data. For example the maximum number of blocks in a single file supported by the `ext3` file system is 2^{31}, which corresponds to a maximum file size of 16 Gigabyte to 2 Terabyte, depending on the block size. The `ext3` file system [17] is used in HDD where the DANCE data is recorded. The `ext3` file system is very commonly used for Linux computers.

Once the data are recorded and backed up to several RAIDs, it is no longer linked to DANCE and the on-line analysis is complete. Further steps in the data processing belong to the off-line analysis sequence.

2.3.2 DANCE analyzer

The MIDAS files of the ^{157}Gd experiment are $\sim$1 Gigabyte each, with one file per run. These files contain raw data of every event detected with DANCE crystals and beam monitors. It is not possible to draw conclusions directly from the MIDAS file. First the data must be analyzed, organized, and rewritten into a human readable format. To do this special software – DANCE analyzer – was designed by J.M.Wouters. Since the analysis is different according to experimental conditions, the analyzer was created as an open code software. Thus a user can make changes, add new features, and adjust the analyzer to specific needs.

The DANCE analyzer is a ROME [18] application, which in turn is a ROOT based framework; the analyzer utilizes all of the ROOT classes. The analyzer consists of modules containing one step of the analysis. Each module is independent from every other module and has an interface, which is the only connection to the other modules. Each module inside the analyzer is called a task. The task satifies the modularity requirements. The task interface is a ROME folder, which is basically a ROOT folder – the storage object of memory data. The ROOT folder is the only area where data memory can be stored. Thus the task interface is the ROME storage object. The user writes only simple codes for physical analysis, rather than a single large code. This structure is why the analyzer was created using ROME.

What the analyzer does on the run-by-run basis is the following:

- Reads a MIDAS file where raw data is stored;
- Reads an xml input file for a number of runs, which contains numerous parameters specific to the experimental conditions;
- Goes along a time scale and selects events within a preset time coincidence window. These events are considered to be associated with the same neutron induced event. Consider T_0 the moment when the trigger arrives. Then the crystal signals arrive

at $T = T_0 + T_e$, where T_e is the time stamp on the leading edge of the event signal. The analyzer selects events within the time range $T = \Delta T \pm 20$ ns. All of the events within this 20 ns window later will go into a particular bin of the two-dimensional [TOF,E_γ] space. Then the analyzer uses sliding time coinsidence window and picks events within the next coincidence window $T = 20 - 40$ ns, and so on. The number of such time coincidence windows depends on both the size of the time coincidence window (20 ns for ^{157}Gd) and the preset looking time window for the experiment (500 μs in the continuous mode). In this example the data is collected for 500 μs after each proton beam trigger, which has a repetition rate of 20 Hz;

- Integrates points of each waveform: 32 points for the fast component I_{fast}, and 500 points for the slow component I_{slow}. The ratio $\frac{I_{fast}}{I_{slow}}$ is used in the particle identification process. This ratio permits the separation of γ-rays from α-particles. Earlier the ratio $\frac{I_{fast}}{I_{slow}+I_{fast}}$ was used, but later this ratio was shown to provide worse resolution;

- Calculates the neutron energy of each event from a given TOF and flight path and fills TOF histograms;

- Calculates the γ-energy of each event from a given E_γ calibration and I_{slow} integral and fills E_γ histograms;

- Fills other histograms with various technical data, such as triggers from the proton beam (in the continuous mode) or external device (in the sequential mode), beam current, data rate, etc. These help to monitor the experimental conditions and to discover any unusual software response to hardware problems.

The analyzer produces so-called histos files that are further used to calibrate data for time and energy, to identify and separate γ-rays from α-particles, and to build energy spectra for physical analysis. After all of this is finished, software for further analysis is up to the user.

2.3.3 Particle identification (PI)

One of the main procedures in the analysis is particle identification, which is achieved by applying the pulse shape discrimination (PSD) technique. As was mentioned

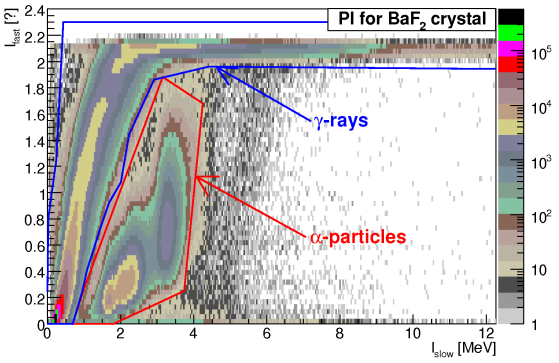

Figure 2.4: I_{fast} vs. I_{slow} for BaF_2 crystal.

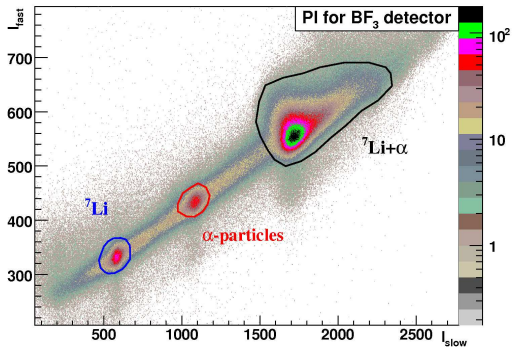

Figure 2.6: I_{fast} vs. I_{slow} for BF_3 beam monitor.

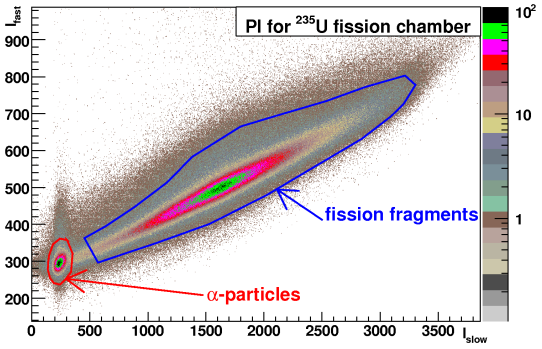

Figure 2.5: I_{fast} vs. I_{slow} for ^{235}U beam monitor.

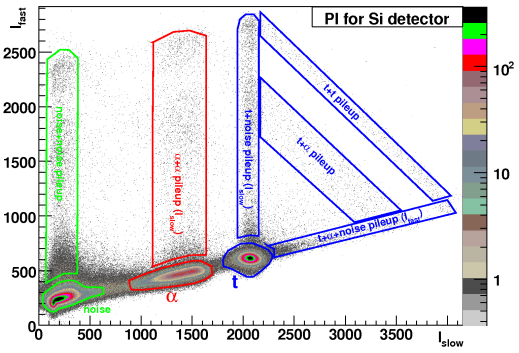

Figure 2.7: I_{fast} vs. I_{slow} for Si beam monitor.

above, the waveform from an event detected by a BaF_2 crystal has two components – slow and fast. The waveform is digitized with a 2 ns time increment. Each of the digital points contains two parameters – time and amplitude. The first 32 points are dedicated to the fast component, and the next 500 points are dedicated to the slow component. The all 32 fast component points are recorded, and the 500 slow component points are integrated into 5 integrals, only these 5 integrals are recorded. The fast component is recorded full details because it is important for the leading edge determination. The integrals of the fast and slow components reflect the light output of the scintillator, which in turn depends on the energy and type of detected particle. Using this dependence one can identify some of the particles detected by the BaF_2 crystals. The same procedure can be used for the beam monitors. The integrals I_{fast} and I_{slow} for each waveform can be arranged in a 2-dimensional space. In Fig. 2.4 - 2.7 the X-axis is a measure of I_{slow}, and the Y-axis corresponds to I_{fast}. Particle identification is performed for each type of detector used in the ^{157}Gd experiment.

First consider the PI for a BaF_2 crystal. As was mentioned earlier, BaF_2 has

an internal α-activity due to the presence of ^{226}Ra, which is a chemical homolog of Ba. Every BaF_2 crystal generates an α-background in addition to the measured γ-rays. This α-background is eliminated by identifying each event via the PSD technique. Figure 2.4 is an example of how PI is performed for the BaF_2 crystal data. In the 2D space of I_{slow} versus I_{fast} one can clearly see that α-events are distinguished from γ-events. An α-event at the same value of I_{slow}, which here is energy calibrated for BaF_2, has a different value of I_{fast}. In fact thiw identification of α-events can be beneficial for the energy calibration of the I_{slow} component. This is used to correct the γ-ray energy calibration for gain shifts (usually due to temperature dependence of the BaF_2 light output). Since α-particles are created inside the crystal, the efficiency for such a perfect "calibration source" is 100%.

The beam monitors have different types of background and detect different particles, so if possible PI should be performed for them in order to associate their measurements with neutron-induced events and to eliminate backgrounds.

The ^{235}U fission chamber is a gas cylinder filled with P10 gas, which is a mixture of 10% metahne and 90% argon. Inside the chamber a small amount of ^{235}U is placed. Incident neutrons hit the uranium target and the $^{235}\mathrm{U}(n, f)$ reaction causes energetic fission fragments to leave the target. In the P10 gas the fission fragments ionize methane molecules and the collected charge creates an electrical signal. Methane was chosen as it has a relatively high gas gain [19]. In addition to uranium fission, other reaction channels are open as well, such as the spontaneous α-decay of ^{235}U. These α-particles contribute to the the count rate and are considered background. Since the α-activity is a natural property of ^{235}U it is not correlated with the intensity of the incident neutron beam. Figure 2.5 shows how fission fragments are separated from α-particles.

The next beam monitor is the BF_3 detector, which is a gas ionization detector filled with BF_3 gas enriched in ^{10}B. Incident neutrons induce the $^{10}\mathrm{B}(n, a)^7\mathrm{Li}$ reaction, and the α-particles and ^{7}Li nuclei ionize the gas. The charge is collected by 3 anode wires inside the detector. The BF_3 detector has a background issue associated with the incident neutron beam intensity – not only the $^7\mathrm{Li}+\alpha$ signal generates events. The $^7\mathrm{Li}+\alpha$ peak can be seen in Fig. 2.6 as the most energetic events. However, the BF_3 detector used in this experiment has 3 different types of signal. Figure 2.6 indicates that signal comes from at least 3 different sources, which are identified as

- $^7\mathrm{Li}+\alpha$ – when the total energy of the $^{10}\mathrm{B}(n, a)^7\mathrm{Li}$ reaction is deposited.

- α-wall effect – when induced charge from only α-particle is detected and not from ^{7}Li.
- ^{7}Li – when induced charge from only this nucleus is detected and not from the α-particle.

The total energy of the $^{10}\mathrm{B}(n,a)^{7}\mathrm{Li}$ reaction is divided between ^{7}Li and α-particle. The energy partitioning between α and ^{7}Li is based on the momentum in the senter-of-mass (COM) system, the ionization generated in the gas depends on the $\frac{dE}{dx}$, which is proportional to Z^2 and the ionization energy of the gas. So the α-particle is more energetic than ^{7}Li, as can be seen in Fig. 2.6. It should be noted that this is an assumption why this detector gives three types of signal instead of one. This assumption was made based on the known physics and detector readings. We do not know exactly what is inside the BF_3 detector, since the company LND INC [20] that produces the detector for commercial purposes does not disclose its details of the detector design.

Another detector used to monitor the neutron beam is the so-called Si beam monitor. It is so-called because it is not only a Si detector. There is also a LiF foil in the beam pipe oriented at a 45° angle to the neutron beam direction. The Si surface barrier detector has its surface vector directed perpendicularly to the LiF foil, and thus the Si detector does not interfere with the neutron beam, and only detects reaction products from the LiF foil. The Li in the foil is enriched with ^{6}Li isotope. The reaction $^{6}\mathrm{Li}(n,\alpha)t$ produces two types of charged particles, which are detected with the Si detector. Figure 2.7 shows an example of how PI is performed for the Si detector. In this spectrum the α-particles and tritons are well separated because they have different energies. There is also some level of system noise (for example low energy X-rays) present. The efficiency for detecting charged particles is $\sim$100% (ignoring solid angle), thus the count rate can be high enough to create pileup of events. The pileup combinations for the Si detector are the following:

- $\alpha + \alpha$
- $\alpha + t$
- α+noise
- $t + t$
- t + noise

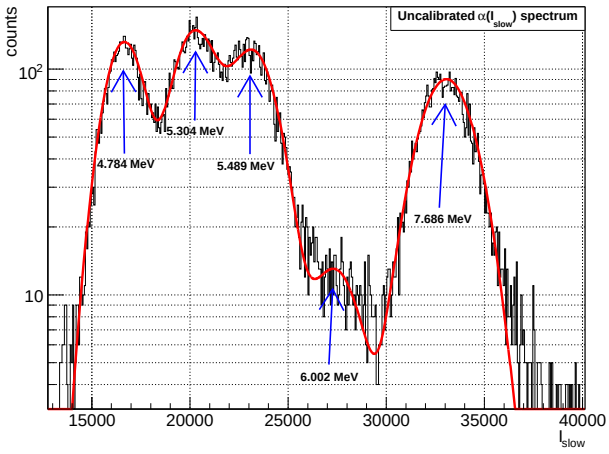

Figure 2.8: γ-energy calibration with internal α-activity.

- $t + \alpha$ + noise
- noise + noise

All of these pileup combinations can be observed in Fig. 2.7. Each pileup can populate either one of I_{fast} or I_{slow} components separately, or both components. The pileup placement depends on how the components are distinguished when performing the PSD procedure. To determine the neutron beam, events have to be associated with a neutron reaction and free of background as much as possible. The best candidate in this case is the triton event.

2.3.4 γ-energy calibration

The TOF technique determines the incident neutron energy by measuring the arrival time of the neutron relative to the time when it was born. For the capture measurements with DANCE one also needs to know the γ-ray energy, which obviously cannot be determined with the TOF technique. The DANCE crystals are calibrated with three standard γ-sources: ^{60}Co, ^{88}Y, and ^{22}Na. Using several sources enables the coverage of a wider energy range. In addition all of the BaF_2 crystals have internal α-activity due to the presence of ^{226}Ra. The energies of those α-particles are well known and can be used for energy calibration. Energy calibration performed using external sources is a standard procedure in experimental nuclear physics and will not be described here. The use of the internal α-activity of barium for energy calibration is more unusual and will be described.

Once the particle identification (PI) is performed for the γ-rays and α-particles, the α-spectrum is created. Figure 2.8 shows such an I_{slow} spectrum for crystal 22 (this crystal has good statistics). The five α-peaks correspond to the five energies listed in Table 1.2 (see Sec. 1.5) for the ^{226}Ra–^{206}Pb decay chain. The five peaks are fit with the formula:

$$F(x) = \sum_{i}^{n_\alpha} a_i e^{-\frac{(x_i - b_i)^2}{2c_i^2}} \tag{2.1}$$

where a_i, b_i, and c_i are the amplitude, location, and width of the ith alpha peak, respectively. n_α is the number of α-peaks to be fit.

A good fit results in values of the parameters a, b, and c for each alpha peak. Each x_i value corresponds to a c_i value, i.e., an I_{slow} channel correlates with γ-energy. This dependence can be described with a simple linear relation:

$$E(x) = A + B \cdot x \tag{2.2}$$

where A and B are the calibration parameters. Of course, instead of a linear fit a more complicated expression, for example a polynomial of degree 2 or more, can be used for a more precise γ-energy calibration. However, for DANCE data the E_γ calibration requirements are not that stringent, the responce function is sufficiently linear to not require higher terms, and the energy resolution of the BaF_2 crystal is $\sim$10%. The precision of the linear fit (Eq. 2.2) is sufficient for the data analysis. On the other hand, for the E_n calibration increased precision is essential, for example for neutron resonance spectroscopy.

The internal α-activity is superior for γ-energy calibration than the use of calibrated γ-sources. There is no need to stop measurements and replace targets, as in case of γ-sources, since the α-source is present permanently inside the crystals. Since the energy calibration can be performed for every run independently, it is possible to monitor the α-activity level as a function of time and to track any changes in the energy calibration (for example due to temperature changes). Both calibration methods are used for DANCE data. The γ-sources provide an initial energy calibration, while the α-activity makes possible the monitoring and correction of the calibration during a run.

2.3.5 Time calibration (alignment)

Neutron energy calibration is essential when measuring neutron capture cross sections. The energy of an incident neutron is determined with the standard formula (Eq. 1.1 in Sec. 1.4). Knowledge of the neutron mass, arrival time, and flight path length, is sufficient to calibrate the incident neutron energy. A neutron capture event leads to a light being generated inside the BaF_2 crystal and this light is collected by and amplified in the photomultiplier tube (PMT). When the signal from the PMT arrives at the data acquisition system (DAQ), all of the 160 channels should be synchronized in time within nanoseconds. For each of the 160 PMTs there are 2 cables that connect PMT and DAQ, one is the power supply, and another one is the signal cable. Since the 2 lengths of the signal cables are used and due to signals being delayed in electronics, the waveform leading edges are not synchronized. The time synchronization of the waveform leading edges from all of the 160 crystals is crucial since the data of all of the 160 crystals must be organized into a single event stream. In the continuous mode each event has a time stamp relative to the trigger coming from the proton beam. Since the trigger opens all of the 160 channels at the same time, prior to organizing the data into a single stream of events, the data are first analyzed to determine how much each crystal deviates from each other in the average time of the waveform leading edges. The exact procedure is as follows:

- initial time coincidence window is chosen rather large, usually 100 ns;
- event time stamps (relative to the trigger) from the crystal 0 are considered to be time zeros within the time coincidence window;
- event time stamps from the crystal N are recalculated into time stamps relative to the crystal 0 within the same time coincidence window;
- relative to crystal 0 time stamps from crystal N are organized into a time distribution histogram with the zero point being the time stamp of crystal 0;
- all of the above steps are performed for all of the 100 ns time coincidence windows during the entire experiment and for each crystal except crystal 0.

From such a time distribution one can determine how much on average crystal (channel) N is faster or slower relative to crystal (channel) 0. This procedure is performed for all

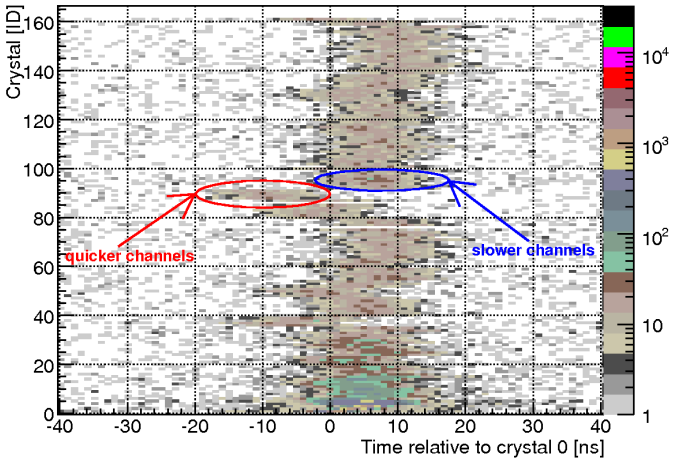

Figure 2.9: Distribution of physical event time stamps relative to the crystal 0.

the $160 - 1 = 159$ crystals and the net result is saved into the time histogram where the $T = 0$ moment is the event time of the 0th crystal. Figure 2.9 is a 2D histogram showing a distribution of time stamps relative to crystal 0. The X-axis is time in ns and the Y-axis is a crystal ID. The 1st Y-bin corresponds to crystal 0, and obviously the only possible value for this crystal is 0.0 ns. The 76th and 86th Y-bins are empty, since these crystals are removed from the DANCE assembly to leave space for the beam pipe. The majority of the channels deliver signals to DAQ that are slower than channel 0, but some channels are faster. For example, the channels of the crystals 88 to 92 are 10 ns faster than the crystal 0 channel.

If a channel is either faster or slower than the channel 0, it is considered unsynchronized. When analyzing data, all time stamps of crystal N are corrected for the same time delay to make the crystal N synchronized with crystal 0. Such a time alignment (calibration) is performed for each crystal individually within one run. If the time calibration is performed well enough, the initial ±100 ns time coincidence window can be reduced to ±10-20 ns. The main objective of this time calibration is to improve the signal-to-noise ratio.

2.3.6 Multiplicity

DANCE is an assembly of 160 BaF_2 crystals. The segmentation enables one to distinguish individual γ rays. There are several ways to interpret the physical event inside the BaF_2 crystal depending on the numbers and combinations of crystals that fire within

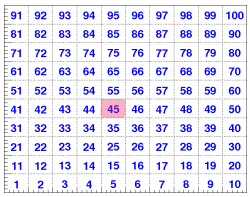

Figure 2.10: $M_{cr} = 1$ and $M_{cl} = 1$.

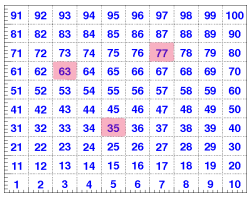

Figure 2.12: $M_{cr} = 3$ and $M_{cl} = 3$.

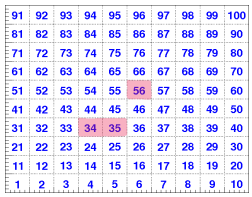

Figure 2.14: $M_{cr} = 3$ and $M_{cl} = 2$.

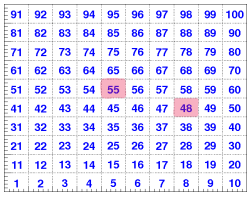

Figure 2.11: $M_{cr} = 2$ and $M_{cl} = 2$.

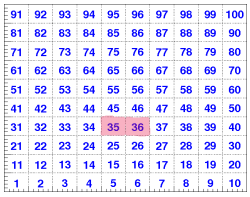

Figure 2.13: $M_{cr} = 2$ and $M_{cl} = 1$.

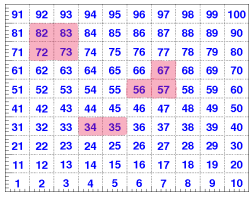

Figure 2.15: $M_{cr} = 9$ and $M_{cl} = 3$.

a time coincidence window. One definition of multiplicity is simply the number of crystals that fire within the given time coincidence window. This is called the crystal multiplicity M_{cr}. However, the crystal multiplicity can be very misleading, since many photons undergo comptoin scattering, are born in a pair production, and they deposit part of their energy in a given crystal and some energy in an adjacent crystal or crystals. Therefore a second definition is used – the cluster multiplicity M_{cl}. The concept of cluster multiplicity M_{cl} is more involved. A cluster is defined as a group of adjacent crystals that fire within a time coincidence window.

Imagine that the crystals are geometrically located as shown in Fig. 2.10 to 2.15 (of course the crystals are not square shaped and there are many more of them. However, the shape and number of crystals are irrelevant for this example in which each number represents a crystal ID).

- 1 crystal fires (Fig. 2.10) – 1 γ-ray, $M_{cr} = M_{cl} = 1$;
- 2 non-adjacent crystals fire (Fig. 2.11) – 2 γ rays from the same capture event, $M_{cr} = M_{cl} = 2$;
- 3 non-adjacent crystals fire, each firing crystal is non-adjacent to the other firing crystals (Fig. 2.12) – 3 γ rays from the same capture event, $M_{cr} = M_{cl} = 3$;
- 2 adjacent crystals fire (Fig. 2.13) – 1 γ ray, $M_{cr} = 2$, $M_{cl} = 1$;
- 3 crystals fire, 2 of them are adjacent, (Fig. 2.14) – 2 γ rays, $M_{cr} = 3$, $M_{cl} = 2$;

- 3 groups of adjacent crystals fire, (Fig. 2.15) – 3 γ rays, $M_{cr} = 9$, $M_{cl} = 3$.

Any combination of firing DANCE crystals can be characterized in a similar manner. Of course, the multiplicity can be higher than 3; in practice the multiplicity of usable data can be as large as M_{cl}=7-9. In the ^{157}Gd analysis the cluster multiplicity was used. This examples shows that at higher multiplicity M_{cl} is more correct than M_{cr}.

2.3.7 Energy spectra

The second step in the DANCE data analysis is building spectra. The types of spectra that are used to draw physical conclusions are described below.

After the data are organized and calibrated, energy spectra are created. Since DANCE data includes various information about every event, one can determine the incident neutron energy E_n (from TOF and flight path data), the individual gamma energy E_γ, and the total γ-ray energy per capture E_{sum}.

DANCE it a calorimeter, it measures the total γ-ray energy of the decay cascade following neutron capture. Decay cascades vary in the number of γ rays and their energies. DANCE data enable determination of the number of γ rays per neutron capture cascade M_{cl} since M_{cl} resembles γ-ray multiplicity, the energy E_γ of each individual γ-ray, and the total energy E_{sum} of the cascade, which is the sum of the individual γ-ray energies:

$$E_{sum} = \sum_{i}^{M_{cl}} E_{\gamma i} \tag{2.3}$$

Any of the energies, E_n, E_γ, or E_{sum} can be used as an axis of energy spectra. Some of types of energy spectra that can be built from DANCE data include:

- E_n vs. $E_{\sum}$ without multiplicity cuts (Fig. 28) – dimensional spectrum with X-axis the neutron energy and Y-axis the total γ-ray energy.
- Yield E_n vs. E_{sum} with multiplicity cuts (Fig. 29) – 2D spectrum with X-axis neutron energy and Y-axis the total γ-ray energy.
- Yield vs. E_n (Fig. 2.18) – neutron energy yield with and without multiplicity cuts.
- Yield vs. E_{sum} (Fig. 31) – 1D spectrum made by projecting E_n cut on E_{sum} axis with and without multiplicity cuts.

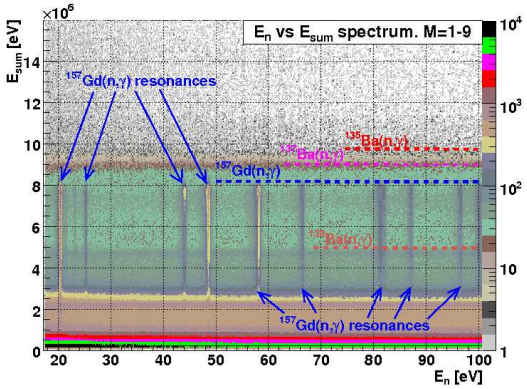

Figure 2.16: E_n vs. E_{sum} 2D plot for $^{157}\mathrm{Gd}(n,\gamma)$ without multiplicity cuts.

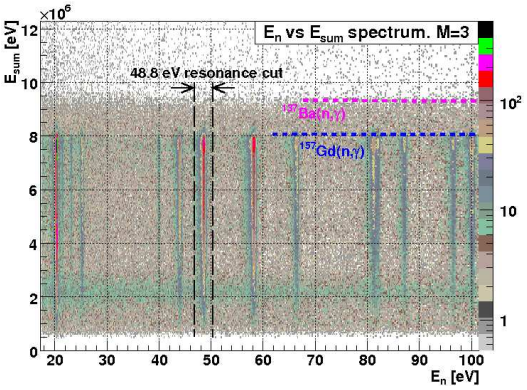

Figure 2.17: E_n vs. E_{sum} 2D plot for $^{157}\mathrm{Gd}(n,\gamma)$ multiplicity cuts.

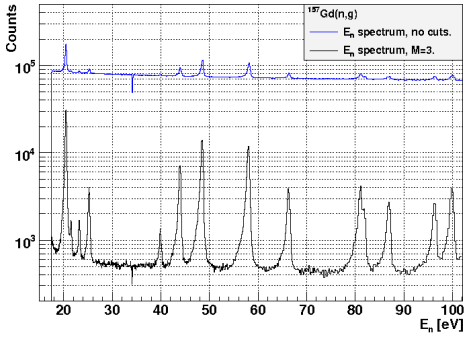

Figure 2.18: E_n yield with and without multiplicity cuts.

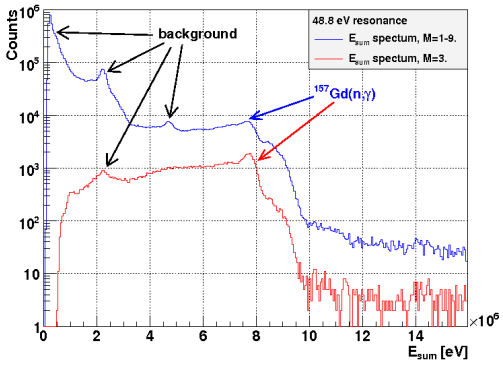

Figure 2.19: $E_{\sum}$ yield with and without multiplicity cuts.

Two types of spectrum are the major sources of physical information from a DANCE experiment, one is E_n vs. E_γ and the other is E_n vs. E_{sum}. In fact, any other type of spectrum can be derived from these two by making projections on one of the axes, placing cuts on another axis, and making M_{cl} cuts.

The gadolinium target consisted of the thin ^{9}Be foil (the exact thickness is unknown, but it is irrelevant) and the ^{157}Gd isotope deposited on the berrylium backing foil. The Q-value of the $^{157}\mathrm{Gd}(n,\gamma)$ reaction is 7.93739(6) MeV, which is shown in the 2D spectra (see Fig. 2.16 and 2.17), as well as lines of the Ba isotopes.

Neutron energy spectra can be built by making projections from the 2D matrices. In Fig. 2.18 two neutron energy spectra are shown. One is the projection made from the 2D spectrum (Fig. 2.16) with no cuts on E_{sum} energy and M_{cl} spans from 1 to 9. The other is the projection made from the similar 2D spectrum (Fig. 2.17) but only for multiplicity $M_{cl} = 3$. The obvious differences in these two neutron energy spectra are the level of counts and background. The $M_{cl} = 3$ spectrum has $\sim 10^2$ counts fewer than the $M_{cl} = 1 - 9$ one. The background is significantly suppressed when increasing the multiplicity. Thus the signal-to-noise of the resonances is increased and they are much easier to analyze.

The total γ-ray energy E_{sum} spectra can be built from the same 2D spectra by making projections, but on different axes than in case of neutron energy spectra. In Fig. 2.19 the two E_{sum} spectra are shown. A narrow cut is put on the neutron energy around the 48.8-eV resonance for both spectra. One E_{sum} spectrum includes data for the range of multiplicities $M_{cl} = 1 - 9$, the other one is only for $M_{cl} = 3$. Increasing M_{cl} has the same effect as in case of neutron energy spectra: the larger M_{cl}, the lower the background.

2.3.8 Background subtraction

The ^{157}Gd target consists of two major components, the Be backing, and the ^{157}Gd isotope deposited onto it. The incident neutrons interact with both nuclides, but with different cross sections. The cross section of the $^{157}\mathrm{Gd}(n,\gamma)$ reaction is one of the highest neutron capture cross sections of natural stable isotopes at thermal neutron energies ~ 0.025 eV. ^{157}Gd also has a relatively large neutron scattering cross section $^{157}\mathrm{Gd}(n,el)$. The $^{157}\mathrm{Gd}(n,\gamma)$ and $^{157}\mathrm{Gd}(n,el)$ cross sections are comparable in the neutron energy range $E_n = 10^0 - 10^5$ eV.

Since the $^9\mathrm{B}(n,\gamma)$ cross section is $\sim 10^5$ times smaller than that of $^{157}\mathrm{Gd}(n,\gamma)$

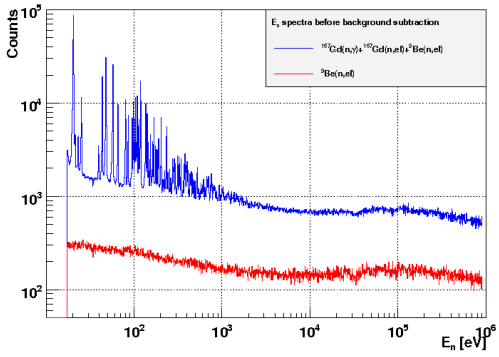

Figure 2.20: Unnormalized E_n spectra of ^{157}Gd and ^{9}Be.

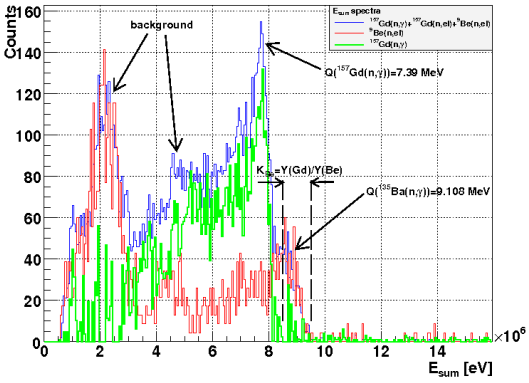

Figure 2.21: Neutron scattering background subtraction: $K_{Be} = \frac{Yield(Gd)}{Yield(Be)}$

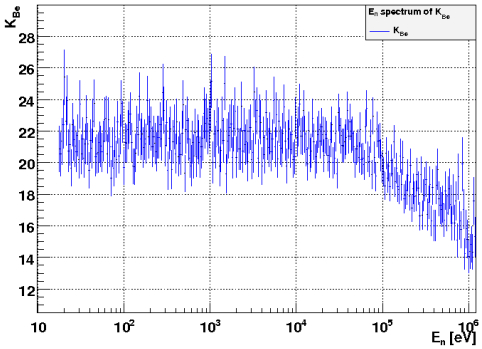

Figure 2.22: E_n spectrum of K_{Be} correlates with the ^{nat}Ba(n,γ) cross section.

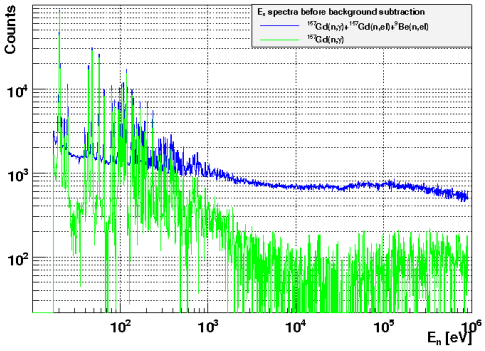

Figure 2.23: E_n spectra of ^{157}Gd before and after background subtraction.

and has no resonances, this background is small. However, the ^{9}B(n,γ) cross section is not negligible: it is $\sim$ 10 b throughout the entire neutron energy range relevant for DANCE, which is 10^{-2} eV – 1 MeV.

Neutron scattering leads to a γ-ray background in DANCE from the Ba(n,γ) reaction in the BaF_2 crystal, and thus has to be accounted for. In Fig. 2.20 two E_n DANCE spectra are shown. One is the raw E_n spectrum of the ^{157}Gd target, which consists of both ^{157}Gd and ^{9}Be. The other one is the E_n spectrum of the Be backing, which is monoisotopic. Neutron capture and neutron scattering on both ^{157}Gd and ^{9}Be contribute to the Gd spectrum, while the Be spectrum contains only data from neutron capture and neutron scattering on Be. Using the Be spectrum allows the subtraction of the corresponding background from the Gd spectrum. The subtraction of neutron scattering background (Fig. 2.21) is performed for each neutron energy bin as follows:

- The E_{sum} spectrum is created by projecting one neutron energy bin of the 2D spectrum onto the Y-axis (E_{sum}). In Fig. 2.21 the E_{sum} spectrum was created by projecting several E_n bins for better statistics and a convenient representation. The initial ^{157}Gd spectrum (blue line in Fig. 2.21) includes both (n,γ) and (n,el) yields. The ^{9}Be spectrum (red line on Fig. 2.21) has only the (n,el) yield. The problem is to extract only the ^{157}Gd(n,γ) yield.

- The Q-value of the ^{157}Gd(n,γ) reaction is 7.93739(6) MeV, while the Q-value of ^{135}Ba(n,γ) is 9.10774(4) MeV. Thus the ^{157}Gd neutron capture overlaps only partially with the ^{135}Ba capture. The high energy part of the ^{135}Ba capture yield is free of ^{157}Gd capture, and thus can be used as a normalization region. The range $E_{sum} = 8.5 - 9.5$ MeV, is free of ^{157}Gd capture. This peak is due to neutrons scattered from ^{9}Be and ^{157}Gd that are captured by ^{135}Ba nuclei in the BaF_2 crystals. Normalization of the ^{157}Gd and ^{9}Be spectra to each other in the E_{sum} region above the Q-value of ^{157}Gd(n,γ) reaction results in this part of the ^{9}Be spectrum being equivalent to the neutron scattering background from the Gd target. Although the ^{157}Gd(n,el) yield is not scaled to the ^{9}Be(n,el) yield.

- The ratio K_{Be} of the yields from Gd and Be in the normalization region is calculated for every neutron energy bin. The (n,el) background subtraction is then performed as $Y(Gd(n,\gamma)) = Y(Gd) - Y(Be)\cdot K$, with the result only neutron capture (green line in Fig. 2.21), which is ^{9}Be(n,el) background free. There are no other (n,el) background peaks and the E_{sum} spectrum ends at Q-value of the ^{157}Gd(n,γ) reaction.

The subtraction of the background due to neutron scattering is the major source of error for the final cross section. As can be seen in Fig. 34, the error bars from the background subtraction alone can be as large as 10–20%. To reduce this error, the E_n spectrum of K_{Be} can be rebinned – 2 or more E_n bins are combined into 1 bin. This rebinning is valid only if the ^{9}Be(n,el) cross section has no resonance structure, because the E_n spectrum of K_{Be} obviously correlates with the ^{9}Be(n,el)+^{157}Gd(n,el) cross sections. The Gd spectra before and after the background subtraction are shown in Fig. 2.23. The spectra in Fig. 2.20–2.23 are all for multiplicity $M_{cl} = 3$.

2.3.9 Dead-time corrections

The data acquisition (DAQ) system is programmed to collect data in two different ways: continuous mode and segmented (sequential) mode. In the continuous mode the data is collected during up to 2 ms starting from a trigger. In the segmented mode it is possible to increase the looking time T_{look} up to 14 ms, and thus cover a wider neutron energy range. Although the segmented mode may look more appealing than the continuous mode, use of the segmented mode data is limited by a dead time issue. The higher the neutron energy in the segmented mode, the larger the losses due to dead time.

To understand the dead time issue one needs to consider the timing sequence of the segmented mode. In the continuous mode the trigger comes from the proton beam, while in the segmented mode the trigger is set artificially whenever two or more crystals fire within the 100-ns time window. After the trigger is set, one digitizing card starts to read data, and the other cards are blocked (dead) from taking data. Each crystal is connected to two cards and one card digitizes the fast component of the waveform, while the other card digitizes the slow component. Each card digitizes data from 4 different crystals. There are several possibilities of how the trigger is set in the segmented mode, and several consequences for the dead time:

- 2 firing crystals set the trigger, with the crystals connected to the same card – this card stays open and collects data for 2 μs from the 4 crystals connected to this card, while all of the other cards are set "dead" (collect no data) for 2 μs plus 1–1.5 μs. Then the cards are allowed to rearm after data collection;

- 2 firing crystals set the trigger, with the crystals connected to 2 different cards – these 2 cards collect data from 8 different crystals, all the other cards are "dead";

- 3 firing crystals set the trigger – 1 to 3 cards collect the data from $1 \cdot 4 = 4$ to $3 \cdot 4 = 12$ crystals, and the rest of the crystals are "dead";

- N crystals fire – up to N cards read $N \cdot 4$ crystals, the rest of the crystals are "dead";

The hardware dead time T_{DAQ} in the segmented mode is the time during which the crystals are not read, starting from each trigger. However, some crystals potentially can be read, even if they are not supposed to, due to the way the crystals are connected to the cards.

There is no practical way to account for this, so they are just blocked by setting up a blocking time when analyzing waveforms. This is the time between the trigger and the moment the the card starts to read the crystals. This time should always be larger than 2 μs, in practice it varies between 3 and 3.5 μs. For the ^{157}Gd experiment it was 3.5 μs; this is the actual dead time T_{dead}.

The segmented mode data is affected by the dead time. The data is collected during $T_{dead} = 3.5$ μs is only from certain crystals. Although the rest of the crystals might detect events, the data from these crystals is not collected. Such a data loss is called a dead time loss. For example, an event was detected at the time of flight corresponding to $E_n = 1$ keV. The majority of the crystals are dead for the next 3.5 μs, during which slower neutrons with $E_n = 0.9$ keV energy might hit the target, but this data will be lost. The next hits, say after 4 μs, will be detected again. Thus, the dead time spans the TOF scale starting from the bin up to $i + 3.5\mu$s.

The losses due to dead time can be determined using probability theory if one assumes that the likelihood of a loss is the same throughout the TOF bins covered by the dead time. There are many methods of calculating the probability of a loss during a dead time. The one channel dead time loss is described as

$$C_{real} = \frac{C_{obs}}{1 - C_{obs}T_{dead}} \tag{2.4}$$

where C_{obs} is an observed count rate, T_{dead} is a dead time, and C_{real} is a real count rate. Consider a TOF bin as a channel in Eq. 2.4. When the n^{th}channel is dead events are lost in this channel during T_{dead}. If two or more events fall into the same channel, 1 event is lost even if this channel is alive, because these two events are recorded as a single event (pile up). Let D_n be the probability of the nth channel being dead and $P_n(N)$ the probability that N true events fall into the nth channel. The probability of losing K events is

$$D_n P_n(N) + (1 - D_n)P_n(N + 1) \tag{2.5}$$

The average number of lost events in the nth channel is

$$X_n = \sum_{N=1}^{\infty} [(1 - D_n)P_n(N) + D_n P_n(N + 1)] \tag{2.6}$$

Now consider C_n to be the average true count rate and $C_n^{'}$ be the observed count rate in the channel n. The true count rate in the channel n is

$$C_n = \sum_{N=1}^{\infty} [NP_n(N)] \tag{2.7}$$

the observed count rate in channel n is

$$C_n^{'} = C_n - X_n \tag{2.8}$$

Assume that X_n is the number of counts per beam burst. The Poisson distribution for P_N then becomes

$$C_n^{'} = (1 - D_n)(1 - e^{-C_n}) \tag{2.9}$$

Thus the probability of a channel being dead depends only on the preceding n channels. The probability of a channel receiving at least one event and therefore being alive is a sum of products of probabilities that all of the m preceding channels that could make the channel n dead are alive. The number $m = \frac{T_{dead}}{TOF_{ch}}$, where TOF_i is the time of 1 TOF channel (assume all TOF bins are of equal width). Thus

$$D_n = \sum_m [(1 - P_m(0))(1 - D_m)] = \sum_m [(1 - e^{C_m})(1 - D_m)] = \sum_m C_m^{'} \tag{2.10}$$

The true count rate in channel n is

$$C_n = -ln[1 - \frac{C_m^{'}}{1 - \sum_m C_m^{'}}] \tag{2.11}$$

where $m \leq n$ always, C_n is the true count rate in channel m, and $C_m^{'}$ is the observed count rate in channel m. The summation is performed over the number of channels m that are before channel n, where $TOF_n = TOF_m + T_{dead}$, i.e., each of the m channels can make the channel n dead.

The dead time correction is made for raw TOF spectra, with no cuts and gates, so the observable count rate is what DANCE actually measures. The TOF spectrum of the dead time corrections can be changed to a neutron energy scale. In Fig. 2.24 the E_n spectrum of absolute dead time corrections for one run is shown. The Y-axis is an absolute

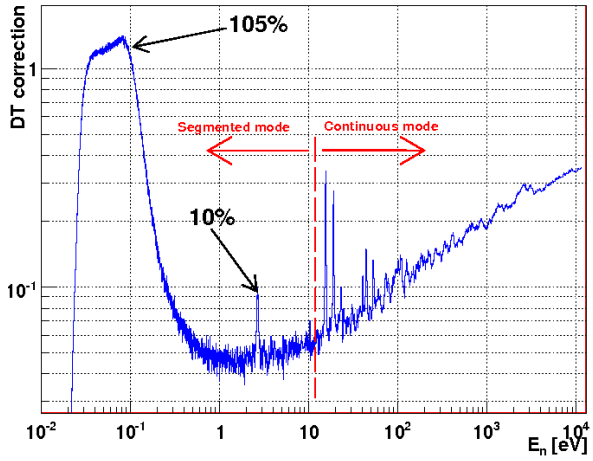

Figure 2.24: Dead time corrections in E_n scale for one run.

scale of correction to be made for a final E_n cross section spectrum. Consider the E_n spectrum of the raw data. At the 2.8-eV resonance the correction is $\sim 10\%$, while around the resonance it is 1–2%. Large dead time corrections are not viable, since the Poission distribution is invalid for large P_N. Thus the correction above $\sim 20\%$ is wrong, limiting the range of the segmented mode data. Whenever possible one should use the continuous mode data. The segmented mode data should only be used to lower neutron energies to the point where the dead time correction is so large such it cannot be corrected properly.

2.3.10 Beam attenuation and target self shielding

To determine the cross section one needs to know the values of the incident neutron flux Φ_n and the target self-shielding factor S_{Gd}. The neutron flux Φ_n is attenuated when passing through the target. The classic transmission experiment is described by the formula

$$\Phi = \Phi_0 e^{-\sigma_{tot} n x} = \Phi_0 e^{-\sigma_{tot} \mu}, \tag{2.12}$$

where Φ is the observed neutron flux transmitted through the target, Φ_0 is the incident flux, σ_{tot} is the total cross section for the target, n is the atomic concentration (density) of the target in $\frac{atom}{volume}$ units, x is the target thickness, and μ is the target thickness in $\frac{atom}{area}$ units. The conditions for the transmission experiment for Eq. 2.12 to apply are:

1. The incident neutron beam is parallel, or at least neither converges nor diverges within

the measurement geometry.

2. The beam intensity profile is uniform.

3. All of the incident neutrons hit the target, i.e., the target diameter must be larger than or equal to that of the beam.

4. The target thickness must be uniform, so that all of the beam transmits through the same amount of material.

5. Attenuation of the beam by the detectors that measure Φ and/or Φ_0 is negligible.

Unfortunately not all of these conditions apply for the ^{157}Gd experiment – only conditions 1 and 5 are satisfied. First, the ^{157}Gd material on the target is a non-uniform deposition electroplated onto the ^{9}Be foil, The ^{9}Be foil also attenuates the neutron flux, although much less than ^{157}Gd. Second, the ^{157}Gd deposition diameter is $\sim$7 mm, which is not the same as the beam diameter at the target location. Third, the beam intensity profile is non-uniform – more intense at the center and less at the edges. The majority of neutrons lie inside the round spot close to a 1-cm diameter circle. The target non-uniformity and the beam profile non-uniformity make the transmission Eq. 2.12 impossible to apply for the ^{157}Gd experiment.

To determine the beam attenuation, images of the neutron beam were taken. One photo image (Fig. 2.26) was taken with the ^{157}Gd target in place. Another photo image (Fig. 2.25) was made with no target in place.

Image 2.25 is basically the beam intensity profile (in arbitrary units). It is clear that the beam profile is non-uniform and is close to a circular shape. The intensity is larger at the center, but its peak is shifted to the right and drops rapidly at the edge of the circle. The difference between the intensities at the center and at 1 cm off-center is up to 25%.

Image 2.26 provides information about the target profile. The ^{157}Gd layer is smaller than the beam spot. In the center the ^{157}Gd deposition is thicker than at the edge. The difference in thickness can be determined from the difference in the beam intensities from these two images. For ^{157}Gd the thickness varies up to a factor of 4. This is only an estimate, since the attenuation is a function of σ_{tot}, which in turn is a function of neutron energy.

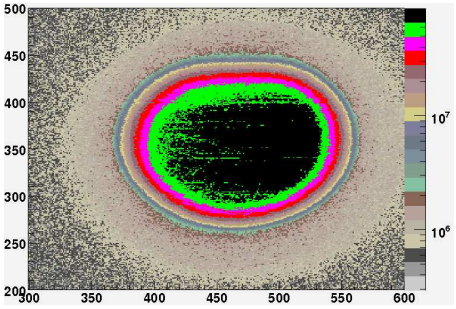

Figure 2.25: Beam image without target

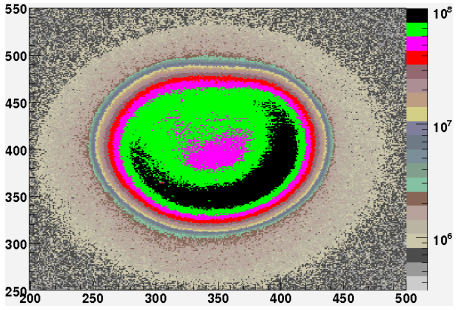

Figure 2.26: Beam image after attenuation by the ^{157}Gd target.

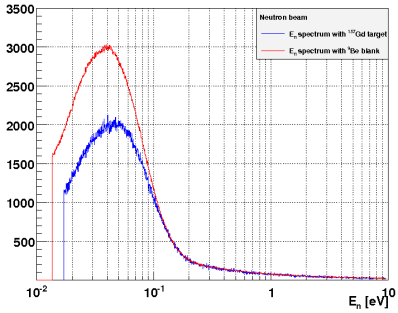

Figure 2.27: Neutron beam spectra with the ^{157}Gd target and the ^{9}Be blank.

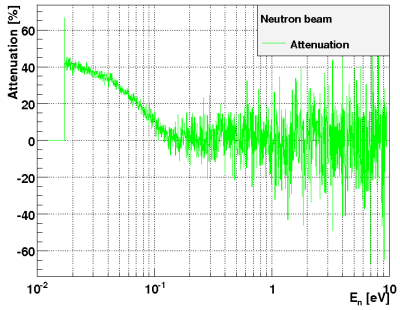

Figure 2.28: Attenuation of the neutron beam by ^{157}Gd.

Thus it is impossible to determine the beam attenuation precisely over the entire DANCE neutron energy range. First, because of the non-uniformity of the ^{157}Gd deposition, and second, because of the dependence of the attenuation on E_n. However, it can be determined for some regions of E_n, for example at resonances and at thermal energies. Therefore, in the DANCE experiments it is desirable to have a target smaller then the incident neutron beam spot.

The thickest part of the ^{157}Gd deposition is $\sim 0.8 \frac{mg}{cm^2}$. The beam attenuation and self-shielding factor are negligible between and at resonances. However, the correction is large at thermal energies, where ^{157}Gd has the largest known σ_{tot} for neutrons.

Since determination of the beam attenuation by the ^{157}Gd target is impossible using Eq. 2.12, it was accomplished empirically. Two neutron spectra (Fig. 2.27) were measured, one with ^{157}Gd (blue line) on the ^{9}Be foil, and another one with only the ^{9}Be (red line) foil. The raw neutron spectra were processed in exactly the same way – the same PIs, cuts, background subtractions, etc. The difference (Fig. 2.28) between the ^{157}Gd+^{9}Be and ^{9}Be spectra is due to the presence of ^{157}Gd, and it is large enough to affect the neutron

beam at thermal energies. In fact, the beam attenuation due to ^{157}Gd at 0.025 eV is $\sim 40\%$. In the E_n = 1 eV – 1 MeV region the beam attenuation is within the statistical error.

2.4 Resonance spectroscopy

In addition to the focus on the capture cross section, the DANCE data can be used to provide much information about the properties of the compund nucleus ^{158}Gd, such as resonance parameters and photon strength functions. These topics are considered in the following sections.

2.4.1 Determination of the ^{157}Gd(n,γ) cross section

Although the original motivation for DANCE was the measurement of cross sections of small and/or radioactive targets (and this was the primary reason for the measurement of ^{89}Y described in the last part of this thesis), the primary motivation for the ^{157}Gd experiment was to learn more about nuclear structure. To determine the absolute cross section independent of other sources, such as the compilations ENDF/B-VII, JENDL, or JEFF, is complicated. Usually one determines the "relative" cross section. In this case the DANCE data is normalized to a well-known resonance taken from the EDNF/B-VII data base. This normalization approach is used when the neutron flux cannot be determined well.

When the ^{157}Gd data set was measured, a relatively high γ-background was present. This ambient background probably originated from the proton beam hitting the walls of the beam pipe, and thus producing high energy γ-rays that were scattered into the Lujan Center. Because of this γ-ray background the DANCE readings were affected. However, this high background condition is not the reason why the ^{157}Gd(n,γ) cross section is determined relative to ENDF/B-VII data.

The major problem lies in the characteristics of the ^{157}Gd target. It was produced by electroplating the ^{157}Gd isotope onto the ^{9}Be backing foil. The thickness of the ^{157}Gd deposition is very non-uniform: the difference in thickness varies by a factor of as much as 4. Also the ^{157}Gd deposition size is close to that of the beam spot, but it is not larger than the beam spot, and the deposition is not located precisely in the center of the ^{9}Be backing. Thus, it is possible that during the measurements the ^{157}Gd target did not entirely overlap the

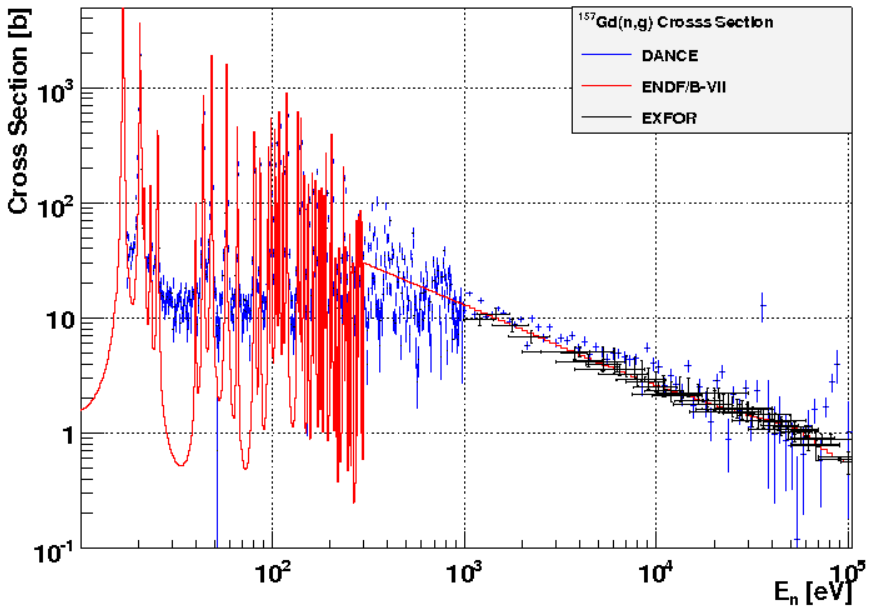

Figure 2.29: Cross section of ^{157}Gd(n, el): DANCE vs. ENDF/B-VII.

beam spot. The beam intensity profile is non-uniform as well as the ^{157}Gd target, although not as much. The intensity measured by the beam monitors differs from the intensity of the beam that hits the ^{157}Gd target.

Our option was to use a well-known cross section as a reference. For ^{157}Gd the reference cross section was taken from ENDF/B-VII in the chosen neutron energy region. The well-known isolated resonance at 58.38 eV was used for normalizing the DANCE cross section to that of ENDF/B-VII. The normalization is performed by scaling the DANCE cross section until it matches the ENDF/B-VII cross section. Once the scaling is done, the normalization coefficient is applied to the entire DANCE neutron energy range of E_n = 10 eV – 100 keV. The resulting ^{157}Gd(n, γ) cross section is shown in (Fig. 2.29). The scaling of DANCE data to that of ENDF/B-VII was performed on several resonances in the energy range 10 – 100 eV, and the resulting normalization coefficients were the same within statistical errors. The DANCE data seem to be in a good agreement at the resonances and in the unresolved resonance region. The differences in the valleys between resonances are larger – the DANCE cross section is larger than the ENDF/B-VII value, which can be explained by the presence of an ambient background, which was the case during the ^{157}Gd measurement.

According to the Mughabghab compilation resonances have been observed up to about 750 eV, but complete analysis has only been performed up about 300 eV. The DANCE data enable the resolution of resonances up to 1074 eV, but the complete analysis is done up to 200 eV. Above the 1074 eV energy the DANCE timing hardware and statistics combined are not precise enough, and thus only the average cross section is determined. Within errors, the DANCE values agree with both those of ENDF/B-VII and EXFOR. At neutron energies above 10 keV the statistical error is large, and the only way to determine the cross section in this region is to rebin the histograms, i.e., to combine several bins.

2.4.2 Resonance spin assignments

The very large segmentation of the DANCE array makes it ideal for determining the γ-ray multiplicity. The distribution of neutron capture intensity as a function of γ-ray multiplicity can be used to assign spins for neutron capture resonances. Various methods to achieve this are described below.

The underlying physics is the following: for this heavy nucleus the decay from a compound nuclear resonance is assumed to be statistical. This decay is primarily dipole. Since ^{157}Gd has ground state spin/parity of $3/2^-$, the resonances formed by s-wave neutrons have spin 1 or 2. The ground state of ^{158}Gd has spin/parity 0^+. Therefore by the simplest of arguments one expects that the statistical decay of spin 2 resonances will have a higher number of γ-rays (higher multiplicity) than the decay of spin 1 resonances. This simple argument does not consider nuclear structure effects, but does describe the spirit of the approach. A wide variety of methods have been developed over the years to utilize the multiplicity to determine resonance spins. Here we discuss only those methods that have been developed for analysis of DANCE data.

The simplest method is to use the average multiplicity. An excellent example where this method worked very well is given by Sheets *et al.* [27]. In this case the average multiplicity differed by about 8% for the two spin states. The average multiplicity $< M_{cl} >$ was calculated for the ^{157}Gd resonances in the energy range $E_n = 20 - 200$ eV as follows:

$$< M_{cl} >= \sum_{M=2}^{7} [M_i Y_i(M_i)] / \sum_{M=2}^{7} [Y_i(M_i)] \tag{2.13}$$

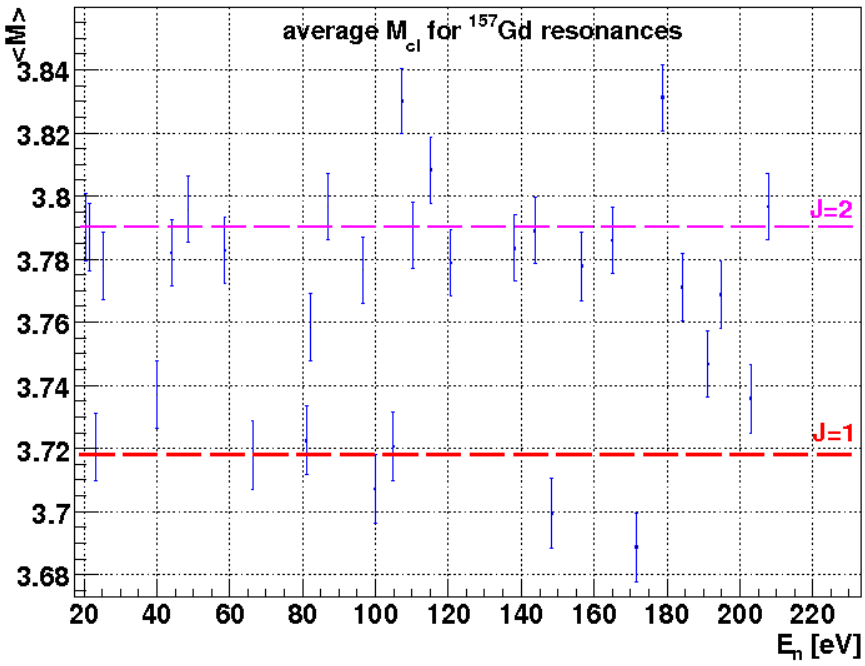

Figure 2.30: Average γ-ray multiplicity. Resonances are divide into two distinct groups – one per spin value.

where M_{cl} is the average γ-ray multiplicity for a given resonance and $Y_i(M_i)$ is the yield at the M_i point of the M_{cl} distribution for a given resonance. The summation is calculated for the range $M_{cl} = 2 - 7$; M = 1 is excluded because it mainly background and M > 7 is excluded because of poor statistics.

In Fig. 2.30 $< M_{cl} >$ is shown for each resolved resonance, each point corresponds to a particular resonance. There are two distinct groups of $< M_{cl} >$ points. One group is around the value $< M_{cl} > = 3.79$ (pink line), all resonances close to that line have spin $J = 2$. Another group of resonances are in the vicinity of $< M_{cl} > = 3.72$ (red line), all resonances in this group have spin $J = 1$. The difference in average multiplicities for two spin values is rather small – only $\Delta(< M_{cl} >) = 0.07$, which corresponds to 2.5% difference in yields between two resonances with different spins.

Therefore this method works fairly well, but has ambiguous results for a number of resonances. This suggests that a more detailed analysis of the multiplicity distribution is appropriate.

Several methods have been developed to determine the resonance spin from the multiplicity information obtained with the DANCE array. One was developed by Koehler

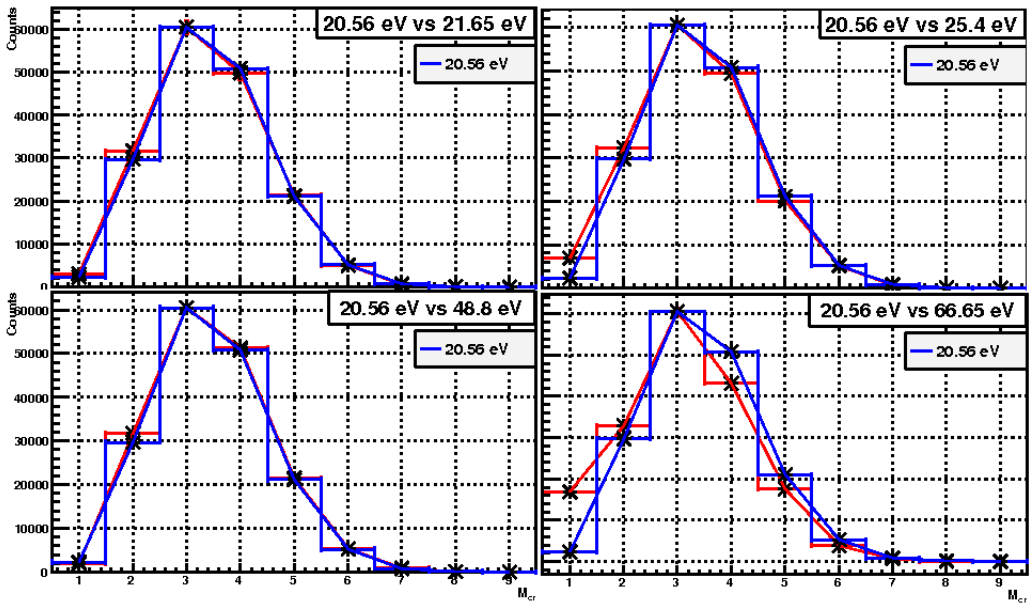

Figure 2.31: M_{cl} distributions are the same if the spins are equal.

[28]. This method provided reliable resonance spin assignments for ^{147}Sm. Since this method is described in detail in the literature [28], here the focus will be on the main idea underlying this method and provide results for the ^{157}Gd resonances.

E_{sum} spectra for $M_{cl} = 1 - 9$ are built from the E_n vs. E_{sum} 2D spectra by projecting the data onto the Y-axis of E_{sum}. E_n gates are placed around the resonances. A set of $E_{sum}(M_{cl})$ spectra for each resonance is then prepared. Each $E_{sum}(M_{cl})$ spectrum is integrated within the E_{sum} gate around the Q-value. Then for each resonance the distribution of these M_{cl} integrals is formed, where the X-axis is M_{cl} and the Y-axis represents this integral $Y(M_{cl})$. The next step is to compare the two $Y(M_{cr})$ distributions (Fig. 2.31) for the different resonances. First their yields should be normalized at some point, usually at $M_{cl} = 3$ or 4. The differences in the $Y(M_{cr})$ are the key. If the distributions are the same within errors, as they are for the 20.56-, 21.65-, 25.4-, and 48.8-eV resonances, then these resonances have the same spin, in this example $J = 2$. If the shapes are different, as they are for the 20.56- and 66.65-eV resonances, where the average M_{cl} is shifted at points $M = 4$, 5, and 6, then the spins are different. The conclusion is that the 20.56- and 66.65-eV resonances have spins $J = 2$ and 1, respectively. This technique requires one prototype resonance with known spin, here the 20.56-eV resonance. Resonance spins may be determined

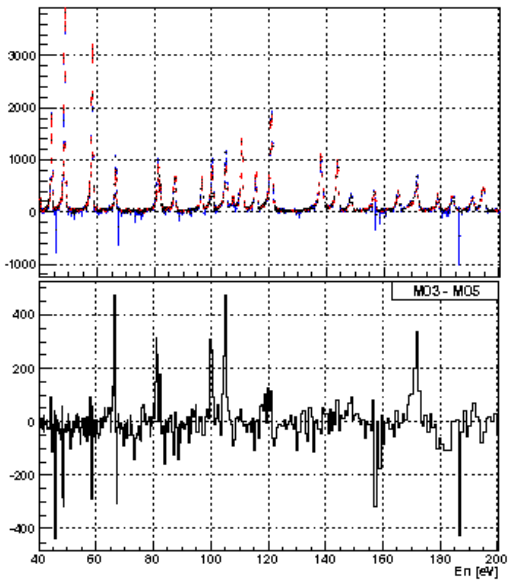

Figure 2.32: E_n spectrum of M3-M5 reveals resonances with $J = 1$ as positive peaks.

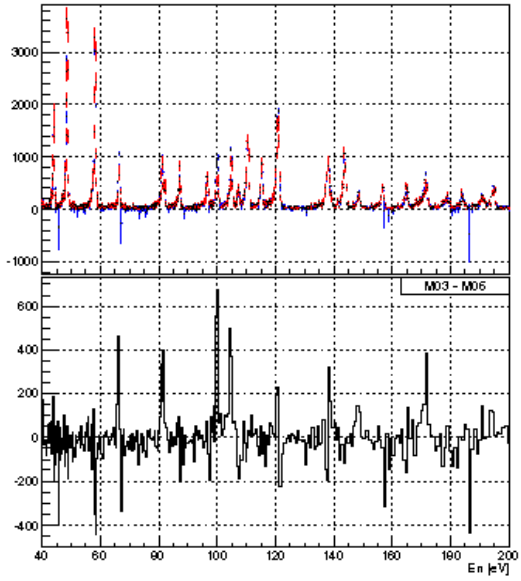

Figure 2.33: E_n spectrum of M3-M6 reveals the same resonances with $J = 1$ as in Fig. 2.32.

with this approach only if the signal-to-noise ratio and the statistics are suitable.

Another method that is closer to the spirit of Koehler's method was developed by the author of this thesis. It exploits the same dependence of spin on the γ-ray multiplicity, but the processing is simpler than in Koehler's method. My method is based on the decomposition of neutron spectra into excitation functions for separate multiplicities, and these are then compared to each other after suitable normalizaton. The spin assignment is made directly from these decomposed E_n spectra.

The E_n spectra for each M_{cl} are built by projecting E_n vs. E_{sum} spectra gated around the Q-value onto the X-axis of E_n. The two $E_n(M_{cl})$ spectra of different M_{cl}, say 3 and 4, are then normalized to each other at a well-isolated resonance with known spin. Then the $E_n(M5)$ spectrum (blue line of Fig. 2.32) is subtracted bin-by-bin from the $E_n(M3)$ spectrum (red line of Fig. 2.32). The resulting decomposed $E_n(M3-M4)$ spectrum may be used to determine resonance spins. If the normalization resonance has spin $J = 2$, then the $E_n(M3-M4)$ spectrum ideally has zero counts at E_n energies of resonances with the same spin $J = 2$. The yield at resonances of different spin $J = 1$ will be positive (or negative if the subtraction is the opposite: $E_n(M4-M3)$). For example, in Fig. 2.32 two E_n spectra, M3 and M5, are compared. They are normalized at the 20.5-eV $J = 2$ resonance. The $J = 1$

resonances are seen at E_n = 66-, 81-, 100-, 104-, 120-, and 167 eV. The same resonances with $J = 1$ are observed with the M3 and M6 E_n spectra (Fig. 2.33).

One major advantage of this method is that there are multiple combinations of the M excitation curves that can be used. The results for this spin assignment method are shown in the Tab. A.2 in the appendix.

The basic idea used here is that the γ-ray multiplicity distribution is different for capture states of different spins, and that this is reflected in different cross sections for each multiplicity. If the effect is large, then even the difference in the average multiplicity can be large enough to determine the spin. For ^{157}Gd this effect is rather small $\sim$2%, and thus one must consider the details of the multiplicity distribution. The advantage of this spin assignment method is that it is simple and can quickly indicate whether a spin assignment is possible. One downside to this approach (as well as that of Koehler) is that it does not provide any numerical information on the probability of the correctness of the spin assignment. Another serious issue is that the method assumes that all resonances with the same spin have identical multiplicity distributions. They are similar, but due to Porter-Thomas fluctuations and experimental errors, they are not identical.

Another spin-assignment method was developed by Becvar *et al.* [29]. The details of the method are described in this paper. This is the most advanced method for spin assignment using multiplicity information since it is the most sensitive of the three methods. Spin assignments for the ^{157}Gd data are possible up to E_n =388 eV, reliable results were produced up to E_n = 205 eV.

This method exploits the dependence of the cross section on the multiplicity distribution on the spin of the resonance state. Fig. 2.34 shows the extracted cross sections for the two possible spin components: $J = I - 1/2$ and $J = I + 1/2$. This figure indicates that the resonances at 81, 100, and 104 eV probably have $J = 1$, not $J = 2$; the other resonances at 87, 96, and 110 eV probably have $J = 2$. The primary advantage of this method is that the fitting (decomposition into the cross sections for two possible spins) is performed at each energy and does not assume that the multiplicity distribution is the same for all resonannces with the same spin

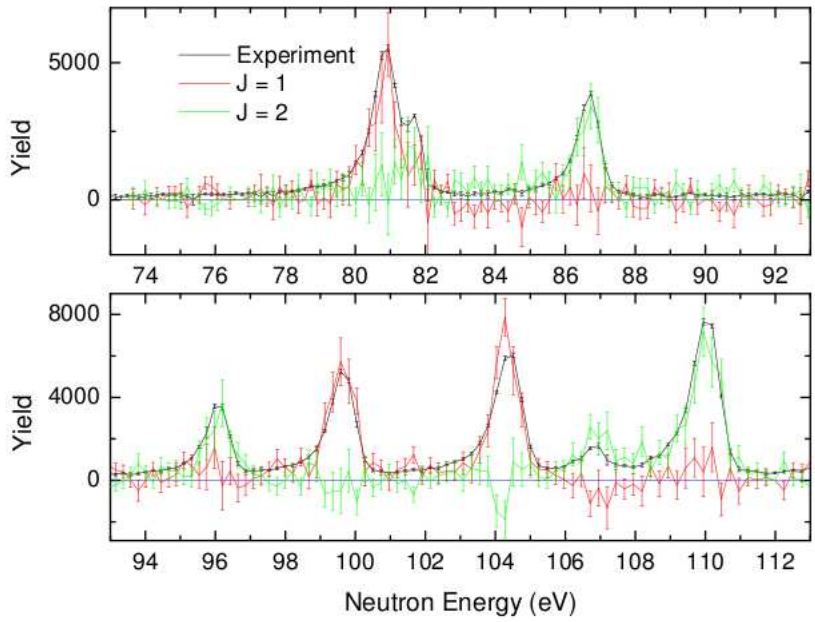

Figure 2.34: Cross sections of the two possible spin assignments, $J = I \pm 1/2$, for each resonance.

2.4.3 Resonance parameters and comparison with nuclear data libraries

The spin-parity of the ^{157}Gd ground state is $J^\pi = \frac{3}{2}^-$. The s-wave capture can excite the ^{158}Gd states with spin-parity values of $J = 1^-$ and 2^-. The neutron binding energy in the compound ^{158}Gd nucleus is 7.73739(6) MeV, thus the final results come from the events within the window of $E_{sum} = 7.1$ – 8.0 MeV. This cut is made after background subtraction to reduce the residual backgrounds.

The ^{157}Gd(n,γ) cross section is one of the largest neutron capture cross sections for natural stable isotopes. Thus, ^{157}Gd(n,γ) resonances were investigated with Ge-detectors [25] before DANCE, but the E_n range is rather limited – so far according to the Atlas of Neutron Resonances [31] the last known resonance is at $E_n = 756.6$ eV. The DANCE results observe resonances up to $E_n = 1.1$ keV. Thus, new ^{157}Gd(n,γ) resonances were discovered in the range $E_n = 878$ – 1074 eV. Spin assignments were possible for the low energy resonances; the results on the DANCE resonance spectroscopy for ^{157}Gd(n,γ) are compared to the Mughabghab data in Table 2.4.3. In the end of this table the new resonances are present and marked with the note *new*. The results for all of the methods that are described in the previous section are listed in the separate table A.2 in the appendix.

Table 2.2: Results of resonance spectroscopy for ^{157}Gd compared to the Atlas of Neutron Resonances of Mughabghab.

Energy	**Mughabghab**			**DANCE**		
E_0 [eV]	J	l	$2g\Gamma_n$ [meV]	$< M_{cl} >$	J	Notes
0.0314 ±0.0002	2	0	0.588±0.01			self shielded
2.825 ±0.015	2	0	0.431±0.004			dead time
16.24 ±0.03	1	0	0.3±0.1			doublet
16.77 ±0.06	2	0	16±1			doublet
20.56 ±0.04	2	0	14.2±1	3.79±0.01	2	
21.65 ±0.04	2	0	0.47±1			doublet
23.33 ±0.04	1	0	0.61±1	3.72±0.01	1	doublet
25.4 ±0.04	2	0	2.3±1	3.78±0.01	2	
40.17 ±0.09	1	0	0.98±1	3.74±0.01	1	
44.22 ±0.1	2	0	11.2±1	3.78±0.01	2	
48.8 ±0.11	2	0	30±1	3.79±0.01	2	
58.38 ±0.08	2	0	35±1	3.78±0.01	2	
66.65 ±0.15	1	0	11±1	3.72±0.01	1	
81.48 ±0.15	1	0	15±1	3.72±0.01	1	doublet
82.30 ±0.15	2	0	7.7±1	3.76±0.01	2	doublet
87.46 ±0.15	2	0	12.7±1	3.80±0.01	2	
96.59 ±0.15	1	0	15.2±1	3.78±0.01	2	
100.2 ±0.1	1	0	35±1	3.71±0.01	1	
105.3 ±0.1	1	0	43±1	3.72±0.01	1	
107.7 ±0.1	2	0	7±1	3.83±0.01	2	
110.5 ±0.1	2	0	53±1	3.78±0.01	2	
115.4 ±0.1	2	0	24±1	3.81±0.01	2	
120.9 ±0.15	1	0	165±1	3.78±0.01	2	
135.19 ±0.15	2	0	1.1±1			
137.9 ±0.15	2	0	59±1	3.78±0.01	2	
138.8 ±0.15	2	0	62±1			doublet
139.3 ±0.15	2	0	7.5±1			doublet

Continued on next page

Table 2.2 Continued from previous page

Energy	**Mughabghab**			**DANCE**		
E_0 [eV]	J	l	$2g\Gamma_n$ [meV]	$< M_{cl} >$	J	Notes
143.54 ±0.15	2	0	75±1	3.79±0.01	2	
148.4 ±0.15	1	0	18±1	3.70±0.01	1	
156.38 ±0.15	2	0	24.7±1	3.78±0.01	2	
164.38 ±0.15	2	0	25.7±1	3.79±0.01	2	
167.88 ±0.15	2	0	2.5±1			
169.51 ±0.15	2	0	4.1±1			
171.18 ±0.15	1	0	33±1	3.69±0.01	1	
178.48 ±0.15	2	0	20±1	3.83±0.01	2	
183.76 ±0.15	2	0	22±1	3.77±0.01	2	
190.58 ±0.15	1	0	21±1	3.74±0.01	1	
194.37 ±0.15	2	0	56±1	3.77±0.01	2	
202.69 ±0.15	2	0	7.2±1	3.73±0.01	1	
205.35 ±0.25	2	0	1.22±1	3.79±0.01	2	
207.56 ±0.25	2	0	135±1		2	
216.9 ±0.25	1	0	6±1			
220.65 ±0.25	1	0	3±1		[1]	
228.05 ±0.25	2	0	8.2±1			
239.3 ±0.25	1	0	190±1		2	
244.6 ±0.25	[1]	0	3.3±1			
246.39 ±0.25	2	0	11.6±1		[2]	
250.2 ±0.25	1	0	4.3±1			
255.0 ±0.25		0	2.7±1			
255.2 ±0.25		0	2.8±1			
260.05 ±0.25	1	0	16.4±1			
265.61 ±0.25	2	0	8.0±1			
268.02 ±0.25	2	0	13.1±1			
281.02 ±0.25	[1]	0	48±1		2	

Continued on next page

Table 2.2 Continued from previous page

Energy	**Mughabghab**			**DANCE**		
E_0 [eV]	J	l	$2g\Gamma_n$ [meV]	$< M_{cl} >$	J	Notes
287.6 ±0.25	2	0	17.8±1			
290.8 ±0.25	1	0	49±1		[1]	
293.7 ±0.25	[1]	0	46±1		[2]	
300.9 ±0.8	1	0	40±1		1	
306.4 ±0.25	2	0	3.5±1			
319.0 ±0.25	[1]	0			1	
321.0 ±0.25	[2]	0				
339.0 ±0.25	2	0			[2]	
350.42 ±0.25	2	0			2	
367.95 ±0.25	2	0				
381.14 ±0.25	2	0			[2]	
388.83 ±0.25	2	0			2	
397.81 ±0.25	1	0				
401.21 ±0.25	2	0				
416.4 ±0.4	2	0				
421.0 ±0.4	2	0			[1]	
429.5 ±0.4	2	0				
445.4 ±0.4	2	0				
451.4 ±0.4	1	0				
457.9 ±0.4	2	0				
472.0 ±0.4	2	0				
475.8 ±0.4	2	0				
485.4 ±0.4	2	0				
510.1 ±0.4	1	0				
530.4 ±0.4	2	0				
539.3 ±0.4	2	0				
555.3 ±0.4	1	0				

Continued on next page

Table 2.2 Continued from previous page						
Energy	**Mughabghab**			**DANCE**		
E_0 [eV]	J	l	$2g\Gamma_n$ [meV]	$< M_{cl} >$	J	Notes
584.0 ±0.4	2	0				
593.0 ±0.4	1	0			1	
602.5 ±0.4	2	0				
618.4 ±0.4	2	0				
666.6 ±0.4	2	0				
743.8 ±0.4	2	0				
756.6 ±0.4	2	0				
878 ±2						new
795 ±2						new
828 ±2						new
846 ±2						new
880 ±2						new
895 ±2						new
854 ±2						new
1026 ±2						new
1057 ±2						new
1074 ±2						new

2.4.4 DICEBOX/GEANT4 simulations

In heavy nuclei complete spectroscopic information is available only for a limited energy range above the ground state, usually of the order of an MeV. As the excitation energy increases, the density of states increases approximately exponentially and resolving the energy levels and the transitions between them becomes progressively more difficult. At some critical energy E_{crit} it is impossible to resolve transition energies even with the best hardware. The region above E_{crit} is called the quasicontinuum. The extreme statistical model is used to describe γ-decay in this region. The major parameters of the statistical model are the nuclear level density ρ and a set of photon strength functions (PSFs) for the

various γ-ray multipolarities.

The multi-step cascade (MSC) spectra are used to study the decay of the ^{157}Gd(n,γ) resonances of known spin and parity obtained with DANCE. The simulated MSC spectra were compared with the experimental MSC spectra and the model parameters adjusted to obtain "best" fits.

Below the critical energy, E_{crit}, all of the characteristics of the decay scheme (energies, spins and parities of levels, and their decay properties) are complete. This information is entered into the statistical model calculation. Above this critical energy the level scheme of the nucleus and it complete decay scheme are generated by using an *a apriori* chosen level density function $\rho(E,J,\pi)$ and PSFs for multipolarities $E1$, $M1$, and $E2$. All higher multipolarities are neglected. The DICEBOX algorithm generates a level scheme for the region above E_{crit} up to the Q-value of ^{157}Gd(n,γ). With this information the transitions are calculated. Partial radiation widths for a transition between states s_1 and s_2 are:

$$\Gamma_\gamma(s_1 \rightarrow s_2) = \sum_{XM} \frac{n^2 f(XM) E_\gamma^{2M+1}}{\rho(E,J,\pi)} \tag{2.14}$$

where $f(XM)$ is the PSF for a transition of type X (electric or magnetic) and multipolarity M; n is a random number with zero mean and unit variance to ensure that individual partial widths fluctuate with the Porter-Thomas distribution. The summation in Eq. 2.14 is performed over all types of possible transitions in this model ^{157}Gd.

One set of all levels and transitions is called a nuclear realization. For fixed PSFs and $\rho(E,J,\pi)$ there could be an infinite number of realizations due to the Porter-Thomas distribution. Typically, 10 – 20 realization with 10^5 cascades each is sufficient to test one DICEBOX model.

DICEBOX provides an idealized version of the MSC cascades, but the detector array has a finite response function. To correct the model calculations for this effect, the DICEBOX output for the MSC cascades serve as the input for the GEANT4 model of DANCE. The GEANT4 model provides only the pulse height response function of the BaF_2 detectors, and says nothing about the target and its properties. The output of the GEANT4 simulation includes MSC spectra (E_γ spectra of individual γ-rays) and E_{sum} spectra (total γ-ray energy spectra) for the multiplicity range M_{cl} = 1 – 9 that may be compared with the experimental data.

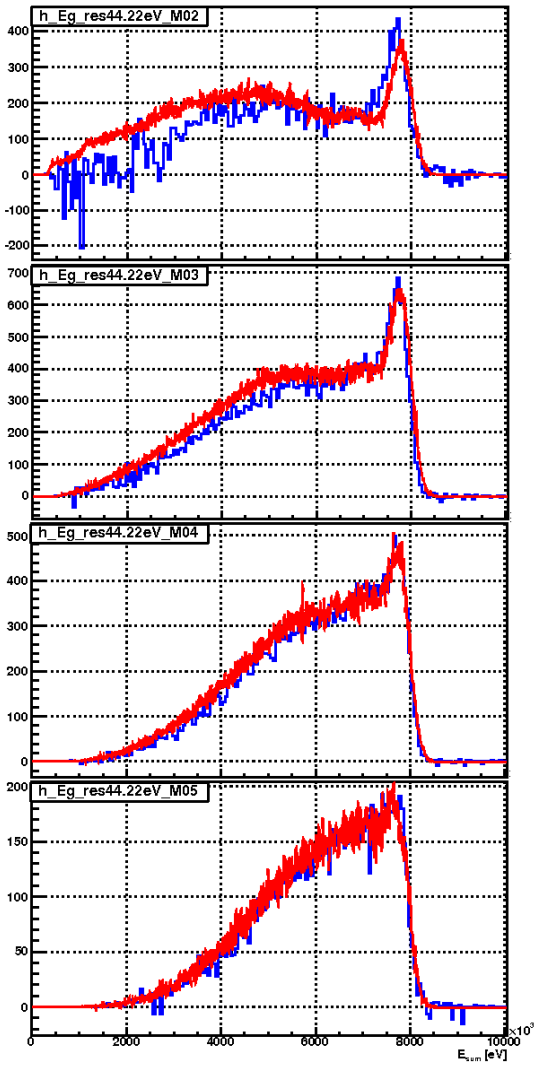

Figure 2.35: E_{sum} spectra of the 44.2-eV resonance for $M_{cl} = 2 - 5$: simulation (red) vs. experiment (blue).

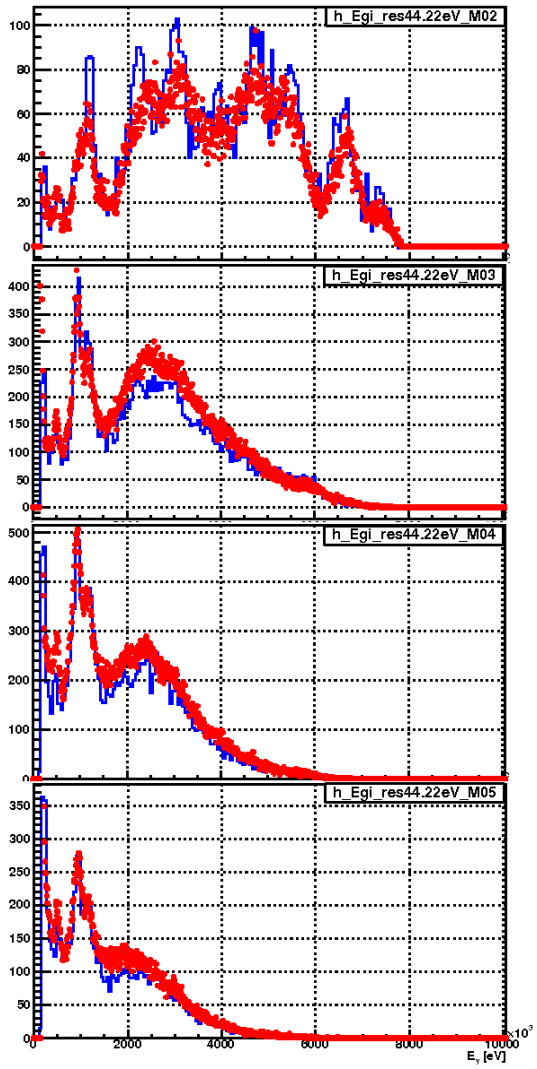

Figure 2.36: E_γ spectra of the 44.2-eV resonance for $M_{cl} = 2 - 5$: simulation (red) vs. experiment (blue).

Then the simulated and experimental spectra were compared and analyzed. Comparisons were made for E_{sum} spectra and E_γ spectra for various multiplities and for the decay of resonances with different spins. Then the appropriate changes, that are anticipated to reduce the differences between the simulated and experimental data, are made in the DICEBOX model and all of the simulations steps are repeated.

Many tests were performed with DICEBOX. One of the best agreements between the simulated and DANCE spectra is shown in Fig. 2.35 and 2.36 of E_{sum} and E_γ. This example is for the DICEBOX model of a $J^\pi = 2^-$ state that includes a 2-component scissors mode in the $M1$ PSf. The parameters are given below. The normalization of the DICEBOX and DANCE data was performed with the E_{sum} spectrum of $M_{cl} = 4$. This normalization coefficient is used for the rest of both the E_{sum} (Fig. 2.35) and E_γ (Fig. 2.36) spectra. The differences at the E_{sum} spectra of $M_{cl} = 2$ are due to a slight shift in the E_γ energy calibration of the DANCE data. The difference in yields is due to the presence of background in the DANCE spectrum. Because the DICEBOX simulations agree better with the DANCE data at higher M_{cl} than at $M_{cl} = 2$, this suggests that the background at higher M_{cl} is subtracted much better than for $M_{cl} = 2$. The E_γ spectra of $M_{cl} = 2$ are the most important when comparing simulations and experiment, because the simulated two step cascade spectra are the most sensitive to any changes made in the DICEBOX model.

2.4.5 DICEBOX simulations of DANCE neutron capture data

The DANCE data for $^{157}\mathrm{Gd}(n,\gamma)$ was taken on the event-by-event basis, thus it is possible to construct many types of spectra. The E_γ spectrum for $M_{cl} = 2$ is similar to the so-called two step cascade (TSC) spectrum. This is the energy spectrum of the 2 γ-ray cascade following neutron capture. In the TSC method, one gates on a total γ-ray energy and multiplicity two. In a traditional TSC measurement one uses high resolution germanium detectors and can study two-γ decay to individual final states. In the DANCE version the multiplicity 2 measurements may include 2-γ decay to many final states (due to the width of the E_{sum} gate). It seemed very interesting to compare the multiplicity 2 measurement performed at DANCE with a direct TSC measurement.

The direct TSC measurements were performed at the LWR-15 research reactor at Rez [26]. The results from the TSC method applied to the $^{95}\mathrm{Mo}(n,\gamma)^{96}\mathrm{Mo}$ data [27] were compared with those measured at DANCE. The agreement was excellent; the model

parameters that fit the TSC data at Rez also fit the MSC data from DANCE. Here we make a similar comparison for the ^{157}Gd(n,γ) data in order to to determine whether the same parameters worked well for the TSC and MSC ^{157}Gd data. The initial PSF parameters used in the DICEBOX model to fit the DANCE data were taken fromt the TSC Rez data for ^{157}Gd and after several trial-and-error attempts were determined more precisely.

The DICEBOX model that generated γ-ray cascades following ^{157}Gd(n,γ) contains some model adaptations [30]. An up to date model that describes the DANCE TSC ^{157}Gd(n,γ) data best is the following:

$$f(E_\gamma) = f_{E_\gamma}^{(E1)} + f_{E_\gamma}^{(M1)} + f_{E_\gamma}^{(E2)} E_\gamma^2 \tag{2.15}$$

where $f^{(E1)}(E_\gamma) = f_{BA}^{(E1)}(E_\gamma)$ is the E1 PSF from the Brink-Axel model at $E_\gamma > E_H$; $f^{(E1)}(E_\gamma) = f_{KMF}^{(E1)}(E_\gamma)$ – from the Kadmenskij-Markushev-Furman model at $E_\gamma < E_H$; $f^{(E1)}(E_\gamma) = k f_{BA}^{(E1)}(E_\gamma) + (1-k) f_{KMF}^{(E1)}(E_\gamma)$ is the hybrid of both the BA and KMF models at $E_L < E_\gamma < E_H$; and $k = \frac{E_\gamma - E_L}{E_H - E_L}$. The numerical values are: $E_L = 6$MeV, $E_H = 8$MeV.

The expressions for E1 PSF's are:

$$f_{BA}^{(E1)}(E_\gamma) = \frac{1}{3(\pi\hbar c)^2} \sum_{i=1}^{2} \frac{E_\gamma \Gamma_{G_i}^2 \sigma_{G_i}}{(E_\gamma^2 - E_{G_i}^2)^2 + (E_\gamma \Gamma_{G_i})^2} \tag{2.16}$$

$$f_{KMF}^{(E1)}(E_\gamma, T) = \frac{0.7}{3(\pi\hbar c)^2} \sum_{i=1}^{2} \frac{\sigma_G E_G \Gamma_G \Gamma(E_\gamma, T)}{(E_\gamma^2 - E_G^2)^2} \tag{2.17}$$

The width is given by

$$\Gamma(E_\gamma, T) = \Gamma_G \frac{E_\gamma^2 + 4\pi^2 T^2}{E_G^2} \tag{2.18}$$

where $T = T(E) = \sqrt{(E-\Delta)/a}$; E is the excitaiton energy of a final level; Δ is the pairing energy; and a is the shell-model level density. The numerical values are: $\Delta = 1.77$ MeV, $a = 17.91$ MeV^{-1}, $E_{G_1} = 12.23$ MeV, $\Gamma_{G_1} = 2.77$ MeV, $\sigma_{G_1} = 215$ mb, $E_{G_2} = 15.96$ MeV, $\Gamma_{G_2} = 5.28$ MeV, $\sigma_{G_2} = 233$ mb.

The components of the M1 PSF are given by

$$f^{(M1)}(E_\gamma) = f^{(M1)}_{SR}(E_\gamma) + f^{(M1)}_{SF}(E_\gamma) + f^{(M1)}_{SP}(E_\gamma) \tag{2.19}$$

$$f^{(M1)}_{SR}(E_\gamma) = \frac{1}{3(\pi\hbar c)^2} \sum_{i=1}^{2} \frac{E_\gamma \Gamma^2_{R_i} \sigma_{R_i}}{(E^2_\gamma - E^2_{R_i})^2 + (E_\gamma \Gamma_{R_i})^2} \tag{2.20}$$

$$f^{(M1)}_{SF}(E_\gamma) = \frac{1}{3(\pi\hbar c)^2} \sum_{i=1}^{2} \frac{E_\gamma \Gamma^2_{F_i} \sigma_{F_i}}{(E^2_\gamma - E^2_{F_i})^2 + (E_\gamma \Gamma_{F_i})^2} \tag{2.21}$$

$$f^{(M1)}_{SP}(E_\gamma) = const \tag{2.22}$$

where $E_{R_1} = 2.5$ MeV; $\Gamma_{R_1} = 0.2$ MeV; $\sigma_{R_1} = 0.1$ mb; $E_{R_2} = 3.1$ MeV; $\Gamma_{R_2} = 0.4$ MeV; $\sigma_{R_2} = 0.2$ mb; $E_{F_1} = 6$ meV; $\Gamma_{F_1} = 0.8$ MeV; $\sigma_{F_1} = 0.7$ mb; $E_{F_2} = 8$ MeV; $\Gamma_{F_2} = 1.8$ MeV; $\sigma_{F_2} = 1.1$ mb; $f^{(M1)}_{SP} = 1 \cdot 10^{-9}$ MeV^{-5}; $f^{(E2)}(E_\gamma) = f^{(E2)}_{SP}(E_\gamma) = 5 \cdot 10^{-11}$ MeV^{-5}.

The model of the back-shifted Fermi gas (BSFG) was adopted to determine the level density in the region above $E_{crit} = 2.1$ MeV:

$$\rho(E, J, \pi) = f(J) f(\pi) \frac{exp[2\sqrt{(E - E_1)a}]}{12\sigma_c 2^{1/2} a^{1/4} (E - E_1)^{5/4}} \tag{2.23}$$

where $E_1 = 0.28$ MeV and $a = 17.91$ MeV^{-1} are adjustable coefficients; $f(J) = exp(\frac{-J^2}{2\sigma_c^2}) - exp(\frac{-(J+1)^2}{2\sigma_c^2})$ is the probability distribution function (PDF) for the spin;
and $\sigma_c^2 = 0.0146 \frac{1+\sqrt{1+4a(E-E_1)}}{2aA^{5/3}}$ is a spin cut off parameter.

At higher energies the level density ρ becomes independent of parity π, when this happens – $f(\pi) = 0.5$, but parity dependence is could be asymmetric below $E = 3$ MeV. The following empirical equation is used to approximately account for this effect:

$$f(\pi = +) = \frac{1}{2}(1 + \frac{1}{1 + e^{(E - \Delta_\pi)C_\pi}}) \tag{2.24}$$

and subsequently

$$f(\pi = -) = 1 - f(\pi = +) = \frac{1}{2}(1 - \frac{1}{1 + e^{(E - \Delta_\pi)C_\pi}}) \tag{2.25}$$

Here Δ_π is the energy at which the level density changes from π-dependent to π-independent with the rate C_π. The values of $E_1 = 9$ MeV and $a = 2.92$ MeV^{-1} were used. The parity dependence related parameters are $C_\pi = 1$ MeV^{-1} and $\Delta_\pi = 5$ MeV. The simulation results, however, proved to be largely independent of the parity, thus, this dependence was dropped.

2.4.6 Summary

The ^{157}Gd experiment was conducted to measure the neutron capture cross section and to test the statistical model and determine the PSFs in that nucleus. The ^{157}Gd target consisted of the ^{9}Be backing foil on which ^{157}Gd was deposited. The ^{157}Gd deposition was highly non-uniform, and thus it was not possible to determine the incident neutron flux absolutely. The ^{157}Gd(n,γ) cross section was determined relative to a well-known isolated resonance in ^{197}Au.

The DANCE data enables the application of γ-ray multiplicity techniques to determine resonance spins. Resonances in the experimental data are observed above those listed in the Atlas of Resonances [31]. New resonances were observed up to $E_n = 2$ keV, but because of limited statistics the spins of these resonances could not be determined. Spin values were determined for the strong resonances up to $E_n = 205$ eV. The DANCE data was compared to that of the Mughabghab atlas [31], and spin values were corrected for several resonances.

The statistical model was tested on the ^{157}Gd(n.γ) data. The DICEBOX code was used to simulate the γ-ray cascades following neutron capture. The GEANT4 model of DANCE simulated the DANCE response function using the DICEBOX output of the γ-ray cascades as a source. The simulated spectra of E_{sum} and E_γ were compared to the experimental data, then the necessary changes were made in the DICEBOX input and the simulation process was iterated. After several trial-and-error attempts the preferred E1, M1, and E2 PSFs were determined. The DANCE results on these PSFs were compared with other data [26] on the same nuclide. Agreement was found within errors. The simulations indicate that the E1 strength can be described by a simple Brink-Axel model [32], and the scissors mode is likely to be present in ^{158}Gd.

Chapter 3

^{89}Y Experiment

3.1 Introduction

Yttrium [21] occurs in many rare earth minerals, even the lunar rock samples have some yttrium content. The only stable isotope is ^{89}Y. Yttrium (Fig. 3.1) is a silver colored metal that is relatively stable in air, but ignites at temperatures above 400°C. Yttrium has numerous applications in industry and science: yttrium is used in making red phosphors for television cathode ray tubes and LEDs. It is also used in many applications, including electrodes, electrolytes, electronic filters, lasers, and superconductors. Yttrium has no known biological role, but exposure to yttrium can cause lung disease in humans and animals. Yttrium is similar to the lanthanoid group and has been grouped with rare earth elements since it is found in rare earth minerals. Yttrium is created through stellar



Figure 3.1: Yttrium has one stable isotope: ^{89}Y.

nucleosynthesis, mainly by the s-process (72%) of slow neutron capture of lighter elements inside pulsating red giant stars, and by the r-process (28%) of rapid neutron capture of lighter elements during supernova explosions. Yttrium isotopes ^{90}Y and ^{91}Y are common products of nuclear fission of ^{235}U in nuclear reactors.

The main interest in measuring neutron capture on ^{89}Y is to improve the value of yttrium as a radchem detector for neutron flux measurements. The absolute cross section of the reaction $^{89}\mathrm{Y}(n,\gamma)$ was determined using the DANCE facility at LANSCE.

3.2 Neutron capture measurements on ^{89}Y

A radchem detector uses a set of radiochemical procedures to determine isotopic ratios of materials, following reactions that occurred in this material.

The yttrium radchem detector involves exposing yttrium to a neutron flux and measuring the products of neutron-induced reactions on yttrium. Figure. 3.2 lists some of the key reactions. The isotopic ratio $\frac{^{87}Y}{^{88}Y}$ is connected with the inelastic neutron scattering and the neutron flux as follows:

$$\frac{^{87}Y}{^{88}Y} = \frac{1}{2}\sigma(n,2n)\Phi_n \tag{3.1}$$

where Φ_n is the neutron fluence above the 11.6 MeV threshold for the $^{88}\mathrm{Y}(n,2n)$ reaction. The problem with Eq. 3.1 is that the ratio $\frac{^{87}Y}{^{88}Y}$ is affected by neutron capture reactions on both nuclei, and the cross sections of both $^{87}\mathrm{Y}(n,\gamma)$ and $^{88}\mathrm{Y}(n,\gamma)$ reactions have not been measured. No data is available for these nuclei in ENDF/B-VII, JENDL, and JEFF libraries. The $^{87}\mathrm{Y}(n,\gamma)$ reaction is impossible to measure because the half life of ^{87}Y, is only 3.34 days. There is a similar issue with ^{88}Y, with a half life of 106.6 days. Measuring the reaction $^{88}\mathrm{Y}(n,\gamma)$ with DANCE is extremely challenging but might be possible. The only reasonable option is to measure the $^{89}\mathrm{Y}(n,\gamma)$ reaction and then use these data to constrain model calculations for ^{87}Y. Both ^{87}Y and ^{89}Y are odd-even nuclei.

The reaction $^{89}\mathrm{Y}(n,\gamma)$ has been measured before. The experimental data (Fig. 3.3) on the cross sections has an error of ∼40% in the E_n range 5 keV to 10 MeV, with the error varying from 10% to 70%. The evaluated data sets (Fig. 3.4) are inconsistent. The difference in cross sections between the different sources is as large as a factor of 10.

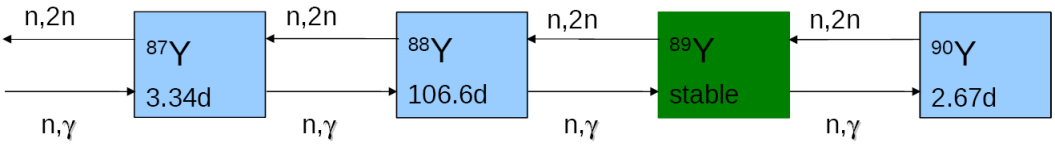

Figure 3.2: Chain of yttrium transformations following neutron exposure.

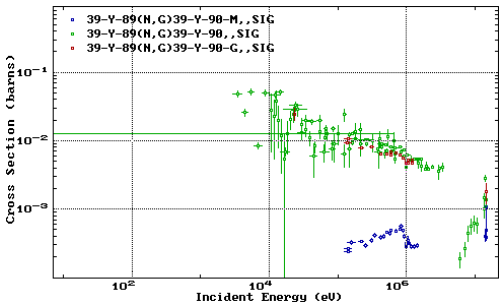

Figure 3.3: EXFOR data for ^{89}Y(n,γ).

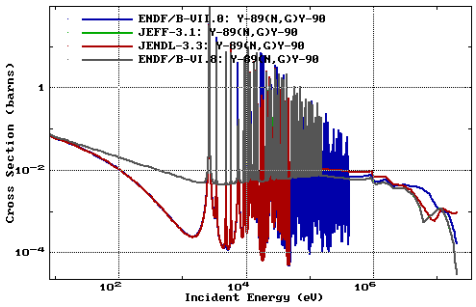

Figure 3.4: ENDF/B-VII, JEFF, and JENDL data for ^{89}Y(n,γ).

Resolving these large differences in cross sections and improving the accuracy is the main motivation for the DANCE measurements of the ^{89}Y(n,γ) reaction. These improved cross sections can then be used to constrain model calculations for the ^{87}Y(n,γ) cross section. The ultimate goal is to measure the ^{88}Y(n,γ) cross section as well, but for now it is not possible due to the short half life of ^{88}Y.

3.2.1 Targets: ^{nat}Y, ^{nat}Fe, ^{nat}Pb, ^{208}Pb, ^{181}Ta, ^{197}Au

DANCE was designed to measure neutron capture, but in practice for some targets backgrounds contribute most of the counts – this is the case for ^{89}Y. The cross section of ^{89}Y(n,el) is 10^2–10^4 times larger than that of neutron capture at different neutron energies. Since it was anticipated that additional background measurements would be needed, several targets (Table 3.2) were prepared to collect as much additional data as possible within a given beam time in order to address the issues of beam attenuation, target self shielding, and neutron scattering background.

There are three ^{89}Y targets: thick (284 $\frac{mg}{cm^2}$), thin (11.3 $\frac{mg}{cm^2}$), and medium (56.7 $\frac{mg}{cm^2}$). Each ^{89}Y target (Fig. 2.1) is a self-supported foil mounted on an aluminum ring. Only the ^{89}Y material is exposed to the incident neutron beam. Of course, it is best to run as thin a target as possible to minimize beam attenuation and target self-shielding problems.

Table 3.1: Targets used in the $^{89}Y(n,\gamma)$ experiment.

Target	**Beam Time**	**Purpose**	**Specs**
^{89}Y	7 days	5% error at E_n=1–100keV	11.3; 56.7; 284 $\frac{mg}{cm^2}$
^{nat}Fe	1 day	(n,el) background	79.8 $\frac{mg}{cm^2}$; 99.995% chemical
^{nat}Pb	1 day	(n,el) background	43.5 $\frac{mg}{cm^2}$
^{208}Pb	1 day	(n,el) background	30.5 $\frac{mg}{cm^2}$; 98.4% isotope
^{197}Au	0.5 day	Flux determination	1.93 $\frac{mg}{cm^2}$
^{181}Ta	1 day	Contaminant	0.5 $\frac{mg}{cm^2}$, 99.988% isotope

For ^{89}Y it was anticipated that low statistics might limit the accuracy of the final (n,γ) data. Since the (n,el) cross section is 10^2–10^4 times higher than that of the (n,γ) reaction, the upper limit of the ^{89}Y target thickness is defined by the DAQ capability to handle a maximum data rate. To account for all of these issues and to obtain the best data possible, it was decided to run three targets that cover a range of thicknesses in the ratios 1:5:25. The data from the thick target is used for low cross section regions (in the valleys), while the thin target data covers resonances where the thick target becomes self shielded and the resonance cross section is significantly affected. As a precaution, data from the medium thickness target was collected as well, in case neither the thin nor the thick target worked out as planned. The medium target is a compromise between statistics and self-shielding issues.

The ^{89}Y targets were produced by Alfa Aesar [23]. Since they are self supported foils, the only background from yttrium is elastic neutron scattering $^{89}Y(n,el)$. Later in the analysis it was discovered that the (n,el) background contributes up to 90–95% of total statistics depending on the neutron energy. The background subtraction must be done as accurately as possible, but first this background has to be separated from neutron capture. An experimental simulation of the (n,el) background can be performed by running a special target – a scatterer. The idea is that the target contributes mostly (n,el) counts, and very little from (n,γ). To qualify for the scattering target, it must satisfy certain requirements:

- should be a stable isotope or mixture of stable isotopes and the atomic number should not be too much smaller than that of ^{89}Y. Otherwise neutrons will be moderated on light nuclei more than on ^{89}Y;

- cross sections of both neutron capture and neutron scattering should be well known;

- should have large (n, el) and small (n, γ) cross section;
- should be a self-supported foil or at least deposited on a very thin backing material (captop, mylar), so that other backgrounds are minimized;
- should have few resonances.

Many isotopes meet these requirements, but the most convenient are ^{nat}Fe and ^{nat}Pb. Both are inexpensive, stable, have a large ratio $\frac{\sigma(n,el)}{\sigma(n,\gamma)}$, weak resonances start in the keV region, and have a flat $\sigma(n, el) \approx 10$ b up to 100-keV incident neutron energy. Later analysis showed that the ^{nat}Fe and ^{nat}Pb targets provide a (n, el) background simulation that is not sufficient to obtain 5% accuracy on the ^{89}Y(n, γ) cross section. Therefore an additional neutron scatterer was measured – ^{208}Pb. This isotope worked better than ^{nat}Fe and ^{nat}Pb; it has a flat $\sigma(n, el) of about \approx 10$ b cross section in the neutron energy range E_n =1 meV – 1 MeV, and the first resonances start at ∼100 keV. In the end the ^{208}Pb(n, el) data was considered best for simulating the ^{89}Y(n, el) background.

During the measurements a quick analysis was done to check the data quality. Some unidentified resonances were present in the ^{89}Y neutron spectra. These resonances were identified as from ^{181}Ta. One possible explanation for the ^{181}Ta contamination is that the technique for making Y foils uses a Ta roller, thus the Y foils were mechanically injected with a small amount of tantalum. ^{181}Ta is the only stable tantalum isotope. The ^{181}Ta(n, γ) cross section is $\sim 10^3$ times larger than that of ^{89}Y(n, γ), so even a tiny impurity of ^{181}Ta may seriously affect the ^{89}Y data. The level of ^{181}Ta contamination was estimated based on the cross sections of both elements. The concentration of ^{181}Ta is 10^{-4}–10^{-5} per ^{89}Y atom. To subtract the contamination background, which includes both (n, el) and (n, γ), a ^{181}Ta target was measured. It was a self-supported foil of 0.5 $\frac{mg}{cm^2}$ thickness and 99.988% isotopic purity.

The last target used in the ^{89}Y experiment was the ^{197}Au target. It is a self-supported foil of 1.93 $\frac{mg}{cm^2}$ thickness. The cross section of the 4.9-eV ^{197}Au(n, γ) resonance is well measured and can be used as a reference for absolute determination of the incident neutron flux at $E_n = 4.9$ eV. Once Φ_n is known at this energy, the flux can be calculated for the entire neutron energy range $E_n = 10^{-2}$–10^6 eV. The obvious condition for serving as a reference target is that the target must have the same geometry as the ^{89}Y target.

3.2.2 Experimental setup

All of the targets related to the ^{89}Y experiment were self-supported foils, mounted on the Al target holder (Fig. 2.2). The Al frame was placed in the center of DANCE, inside the beam pipe under vacuum, similar to the targets in the ^{157}Gd experiment (Sec. 2.2.2). The beam pipe, where the targets were placed, was under 50 mtorr vacuum (1 torr = $\frac{1}{760}$ bar = 133.332 Pa); thus neutron beam attenuation by air was negligible.

The initially scheduled targets were ^{189}Y, ^{nat}Fe, and ^{197}Au. During the measurements a small portion of the ^{189}Y data was replayed for a quality check, and the ^{181}Ta contamination was discovered. The decision was to adjust the remaining beam time in order to run the ^{181}Ta target as well. After the entire ^{89}Y data set was measured and processed, it turned out that the quality of the ^{nat}Fe data was not as good as anticipated. Therefore, two more neutron scattering targets were tested, namely ^{nat}Pb and ^{208}Pb, and ^{208}Pb was chosen to subtract the (n, el) background.

All of the data of the ^{89}Y experiment was taken using the DAQ continuous mode. The incident neutron energy was limited to ∼10 eV at the low end, and 1 MeV at the top. The segmented mode was not used since the region of interest spans the keV energies, which is completely covered with the DAQ working in the continuous mode. The total dedicated beam time, including the targets that were measured later, was ∼12 days.

After the analysis of the ^{89}Y data was completed, the final cross section data implied that improved statistics would help to reduce the error. Thus more data were taken on two targets, ^{89}Y and ^{208}P. The beam time was split equally between ^{89}Y and ^{208}Pb targets, since most of the error comes from the (n, el) background subtraction. The additional statistics improved the accuracy by ∼30%.

3.3 Data analysis

The raw data from the ^{89}Y experiment was saved into binary files in the MIDAS format [10], the same as for the ^{157}Gd experiment. The total number of runs is 235, which corresponds to an average data rate of 1 $\frac{Gbyte}{hour}$. Of these runs 113 are with the ^{89}Y targets, and of these 62 runs are with the thick ^{89}Y target. This target was considered the best for cross section determination due to higher statistics. The remaining $235 - 113 = 122$ runs of the Fe, Pb, Au, and Ta targets provide additional data for the (n, el) background

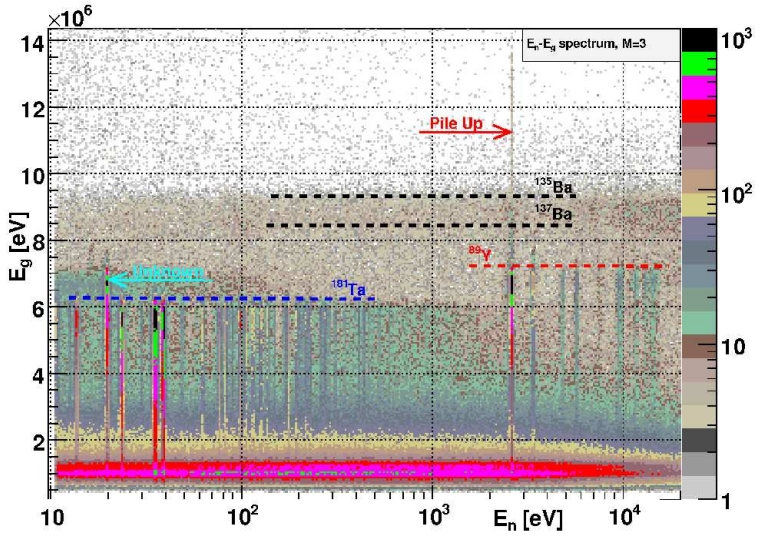

Figure 3.5: 2 D spectrum for the thick yttrium target for M_3.

subtraction, the ^{181}Ta contaminant subtraction, and the neutron flux determination. Some of the data processing procedures are similar to those for ^{157}Gd, but a significant part of the data analysis is unique for ^{89}Y. In the following chapters I shall refer to ^{157}Gd if the data analysis is similar, and shall describe the analysis in detail if it is different from that followed for ^{157}Gd.

3.3.1 Overview of the raw data spectra

During the ^{89}Y experiment a small portion of the data was replayed, calibrated and organized, and an initial check performed to enable decision making regarding additional targets and measurements. Figure. 3.5 is the 2D spectrum from the thick ^{89}Y target for $M_{cl} = 3$ only. The X-axis is the incident neutron energy E_n, and the Y-axis is the total energy E_{sum} of the neutron capture decay. This spectrum immediately shows the issues with the (n, el) background and some unknown non-Y resonances, indicating the existence of contaminants.

The first unusual thing to notice is that there are some resonances in the E_n =10–400 eV region. The Q-value of these resonances is ∼6.1 MeV, less than the 6.857 MeV Q-value of the ^{89}Y(n, γ) reaction. Thus, these resonances are from an impurity in the ^{89}Y target. From the E_n energies of each resonance and the Q-value the resonance was identified

Table 3.2: Q–values for (n,γ) on Y, Ta and Barium.

Isotope	**Q**(n,γ) **[MeV]**	**Abundance [%]**
^{89}Y	6.857	100
^{181}Ta	6.063	99.988
^{134}Ba	6.972	2.417
^{135}Ba	9.108	6.592
^{136}Ba	6.906	7.854
^{137}Ba	8.612	11.232
^{138}Ba	4.723	71.698

as due to neutron capture on ^{181}Ta. At this point a ^{nat}Ta target was scheduled for DANCE measurement in addition to the other targets.

The ^{89}Y resonances start at ∼2.6 keV. Using the TOF technique they can be distinguished up to 20 keV incident neutron energy. One resonance is above the Q-value of ^{89}Y(n,γ), up to E_{sum}=14 MeV. This is due to pileup and it is observed only with the thick ^{89}Y target.

There is also one unidentified resonance at 20 eV. The E_{sum} spectrum of this resonance indicates that it is not from ^{181}Ta, but probably from one of the Gd isotopes. Being unable to resolve this anomaly, the points around 20 eV are simply dropped from the ^{89}Y(n,γ) cross section. No E_{sum} data similar to the unidentified resonance was observed at other E_n energies. Thus the conclusion is that this resonance is the strongest in its isotope, and this isotope affects no other cross section data except for the E_n = 20 eV narrow cut.

The major challenge in analyzing the ^{89}Y data was the neutron scattering background. ^{89}Y scatters neutrons 10^2–10^3 times more effectively than it captures them. Neutrons scattered from the target are scattered inside the BaF_2 crystals and eventually are captured. Since natural Ba is a mixture of 5 isotopes with different abundances, there are 5 different (n,γ) channels. Each produces its own capture decay cascade and has a different Q-value. In the spectrum (Fig. 3.5) at least two Q-value boundaries are seen. One results from ^{135}Ba(n,γ) and another from ^{137}Ba(n,γ).The intensities of these two captures are different due to difference in cross sections and isotopic abundances. These capture reactions are background for the ^{89}Y(n,γ) reaction and must be subtracted. The level of (n,el) background is rather high for ^{89}Y; it contributes up to 90-95% of the total statistics. Fortunately, two of the five Ba isotopes have their neutron capture Q-values distinctly higher than that

for ^{89}Y(n,γ), thus neither the ^{135}Ba nor the ^{137}Ba background contributions can be used to subtract the entire (n,el) background from all five Ba isotopes.

Another background is the low E_{sum} energy background, which consists of several components:

- 511-keV annihilation peak – the γ-quantum produces an $e^- - e^+$ pair and the positron annihilates with the electron. Two 511 keV γ-quanta are created – one escapes the BaF_2 crystal, and one is detected;
- 1022-keV annihilation peak – the γ-quantum produces an $e^- - e^+$ pair, the positron annihilates with the electron. Two 511 keV γ-quanta are created and both are detected with the BaF_2 crystal;
- 2-MeV peak – double annihilation γ-quanta plus β^--decay;

These backgrounds originate from different sources: the target, the BaF_2 crystals and the ambient background. It is practically impossible to account for these sources correctly. An energy cut on E_{sum} above 2 MeV is the only option for eliminating these backgrounds.

3.3.2 Time calibration spectra. Differential cross section. γ-energy calibration. Particle identification (PI).

The time calibration procedure for the ^{89}Y data is very similar to that followed for the ^{157}Gd data (Sec. 2.3.5). However, due to the relatively high count rate the procedure for the ^{89}Y data has some differences from the case of the ^{157}Gd data.

DANCE is an array of 160 BaF_2 crystals arranged in a 4π sphere. The incident neutron beam hits the target in the center of DANCE. Besides neutron capture other reaction channels are open, one of which is elastic neutron scattering. The distribution of the scattered neutrons is not isotropic. The differential cross section for ^{89}Y(n,el) (Fig. 3.6) indicates that angular distribution is forward peaked. In general at lower energies the neutron scattering is closer to isotropic.

Thus the downstream part of DANCE experiences a higher (n,el) background than the upstream part. Crystals located in the downstream part of DANCE generate data at a higher rate than the rest of the BaF_2 crystals. As long as neutron capture is a dominant contributor to the data rate, this issue is not that important. For ^{89}Y, where most of the

data rate comes from the (n, el) background, this asymmetry must be accounted for when performing the time calibration. The time calibrated spectrum (Fig. 3.7) indicates that some crystals have more counts than others. For example, the crystals 52 – 57 have more counts – evidence of higher statistics; while the crystals 62 – 67 have less counts, so they experience lower (n, el) background.

Although downstream crystals as seen on the time spectrum undergo higher count rate relative to the crystal 0, the data from all of the crystals is being gated when choosing cuts for the time coincidence window. Thus no capture data will be lost as long as data from upstream crystals is not cut off. For example, Fig. 3.7 indicates that it is possible to put the time window as narrow as 5 – 10 ns; this will eliminate most of the neutron scattering background and keep the capture data.

The γ-energy calibration of the ^{89}Y data was performed similar to the procedure for ^{157}Gd (Sec. 2.3.3). This was also true for the PI procedure (Sec. 2.3.3) for the BaF_2 crystals and the 3 beam monitors.

3.3.3 ^{181}Ta contaminant in the ^{nat}Y targets

As mentioned above, all of the ^{89}Y targets are contaminated with tantalum. The major stable isotope of tantalum is ^{181}Ta, with a natural abundance of 99.988%. There are also are traces of the metastable isotope ^{180m}Ta (0.012%), which is ignored here. An attempt was made to clean the ^{89}Y target of ^{181}Ta. The initial assumption was that the ^{89}Y foils were made by rolling the raw ^{89}Y material with ^{181}Ta rollers, and that therefore the ^{181}Ta contamination was on the surface of the ^{89}Y target. The medium, 5 mil thick, ^{89}Y target was etched with nitric acid. The mass of the ^{89}Y foil was reduced by ∼10%; its thickness was reduced from 5 mil to 4.5 mil (1 mil = 10^{-3} inch). When this target was again measured with DANCE, there was no change in the level of the ^{181}Ta contamination. Thus, the ^{89}Y targets are contaminated with ^{181}Ta homogeneously, and there is no known way to remove that contamination except to prepare new ^{89}Y targets.

A high purity ^{181}Ta target was measured with DANCE to isolate the contaminant effect on ^{89}Y. In Fig. 3.8 two neutron spectra for multiplicity M_{cr}=3 are presented; one (blue line) is ^{89}Y before any correction for background; and another (green line) is the pure ^{181}Ta spectrum. The resonances of both spectra below 100 eV match well. The aim is to reduce the ^{181}Ta background as much as possible without losing the ^{89}Y data. The

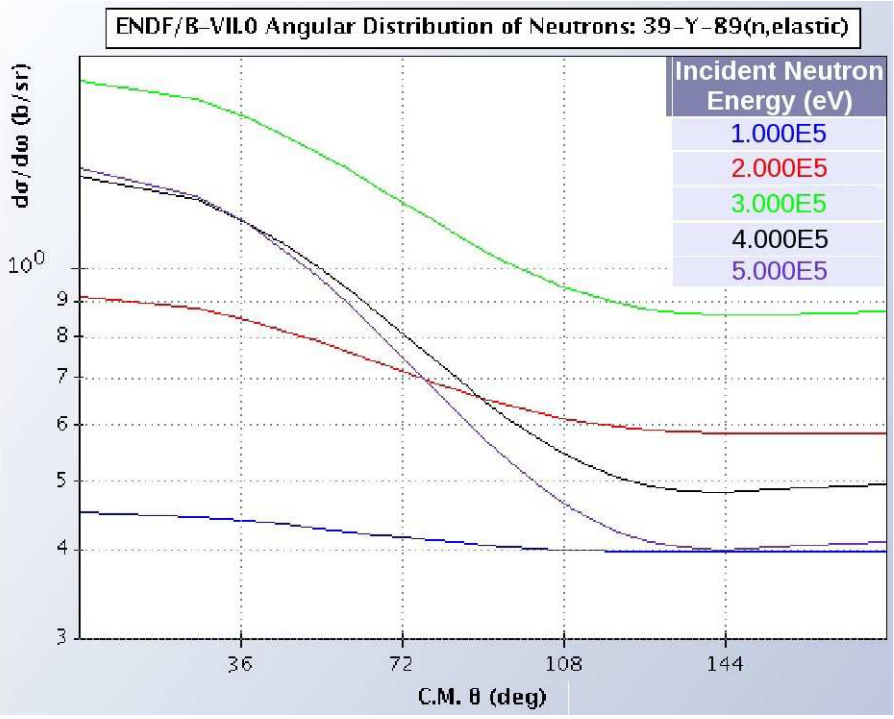

Figure 3.6: Differential cross section of ^{89}Y(n, el) at several E_n energies.

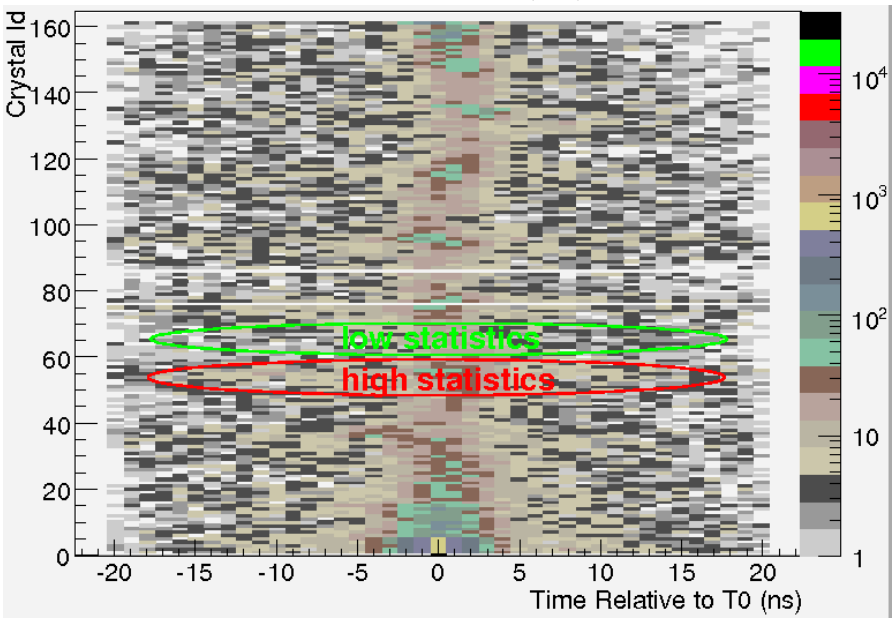

Figure 3.7: Downstream DANCE crystals experience higher (n, el) background than upstream crystals.

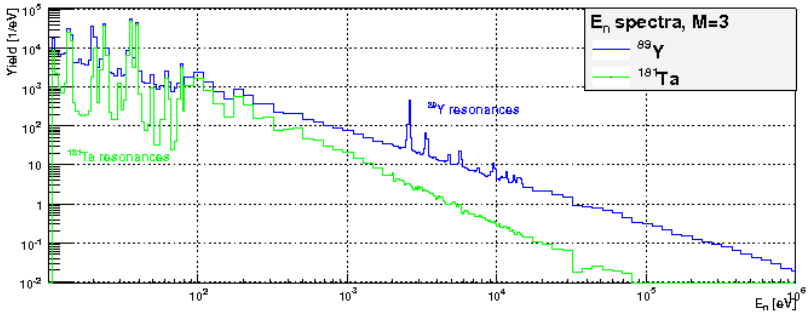

Figure 3.8: Neutron spectra of ^{89}Y contaminated with ^{181}Ta and of pure ^{181}Ta.

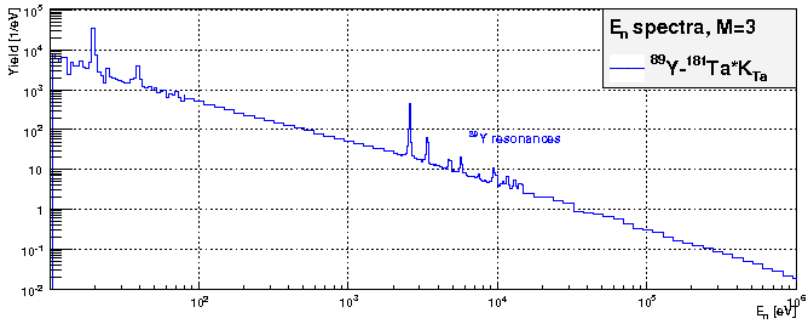

Figure 3.9: Yttrium neutron spectrum after ^{181}Ta is subtracted.

subtraction is performed for each neutron energy bin as follows:

$$N(^{89}Y) = N(^{89}Y +^{181} Ta) - N(^{181}Ta) \cdot K_{Ta} \tag{3.2}$$

where $N(^{89}Y +^{181} Ta)$ is the number of counts in the E_n bin of the ^{89}Y target contaminated with ^{181}Ta; $N(^{181}Ta)$ is the number of counts in the same E_n bin of the pure ^{181}Ta target; and $N(^{89}Y)$ is the number of the ^{89}Y counts after subtracting the ^{181}Ta background. The resulting E_n spectrum for $M_{cr} = 3$ of ^{89}Y is shown in Fig. 3.9. Some residual contaminant background is left at the energies of $E_1 = 19.5$ eV (possibly a Gd isotope), and $E_2 = 37$ eV (pileup of the ^{181}Ta resonance). The latter can be easily eliminated by applying E_{sum} cuts close to the Q-value of the ^{89}Y(n,γ) reaction, which is higher than that of ^{181}Ta(n,γ).

The level of the Ta contamination was estimated to be 10^{-4}–10^{-5} per ^{89}Y atom. It is no surprise that such a tiny quantity of ^{181}Ta produces such a prominent background effect in the ^{89}Y measurements, because the cross section of ^{181}Ta(n,γ) is $\sim 10^2$–10^3 (depending on the neutron energy) larger than that of ^{89}Y(n,γ).

The Ta background is important only in the low neutron energy region, below 100 eV. The ^{89}Y resonances start at $E_n = 2.6$ keV, here the Ta background contributes ∼10% of the total statistics.

3.3.4 Simulating neutron scattered $^{89}\mathbf{Y}(n, el)$ background

Scattered neutrons mainly resulting from the ^{89}Y(n, el) reaction is the major source of background. In fact, the (n, el) background was the major source of the count rate in the ^{89}Y experiment: over 90% of the total statistics was due to neutrons scattered from the ^{89}Y target and then captured by the five Ba isotopes in the BaF_2 crystals. Subtracting the (n, el) background accurately is the most challenging and important part of the DANCE data analysis.

To subtract the (n, el) background it must first be separated from the ^{89}Y(n, γ) data. As explained above, the scattered neutrons are captured by the five Ba isotopes. The E_{sum} neutron captures on Ba isotope are similar to the capture on ^{89}Y; the only difference is in the Q-values . Two Ba isotopes, ^{135}Ba and ^{137}Ba, have Q-values equal to 9.108 and 8.612 MeV, respectively. These are larger than the 6.857-MeV Q value of ^{89}Y(n, γ). This difference in Q-values is large enough to separate neutron capture on ^{89}Y from capture on these Ba isotopes, and thus, from the (n, el) background; it just has to be simulated properly.

To simulate the (n, el) background means to collect the data from some target that has a neutron scattering cross section similar to the ^{89}Y neutron scattering cross section, and has negligible neutron capture. Several targets, ^{nat}Fe, ^{nat}Pb, and ^{208}Pb, that satisfy these requirements were measured with DANCE. The best neutron scatterer turned out to be ^{208}Pb. In Fig. 3.10 is a plot of the ENDF/B-VII cross sections versus incident neutron energy. There are 4 reactions shown:

- ^{89}Y(n, γ) – the green line. This is very small between the resonances (10^{-2} – 10^{-3} barn), and few resonances are larger than 10 barn. This cross section varies depending on the nuclear data library.

- ^{89}Y(n, el) – the blue line. This cross section is 10^2 – 10^3 times larger than ^{90}Y(n, γ). The first resonance occurs at ∼2.6 keV, at the same E_n as neutron capture.

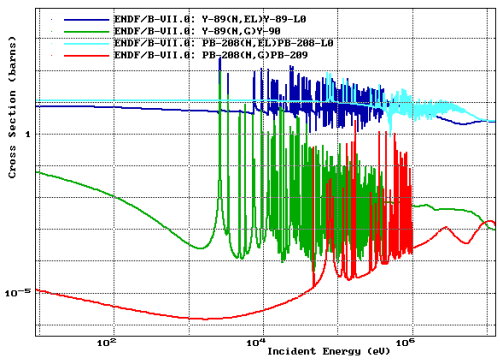

Figure 3.10: ENDF/B-VII data on (n, γ) and (n, el) for ^{89}Y and ^{208}Pb.

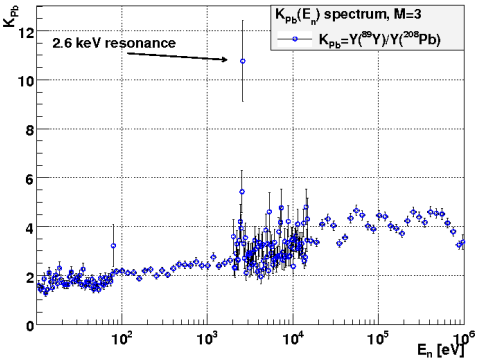

Figure 3.12: $K_{Pb}(E_n)$ correlates with the ratio $\frac{^{89}Y(n,el)}{^{208}Pb(n,el)}$.

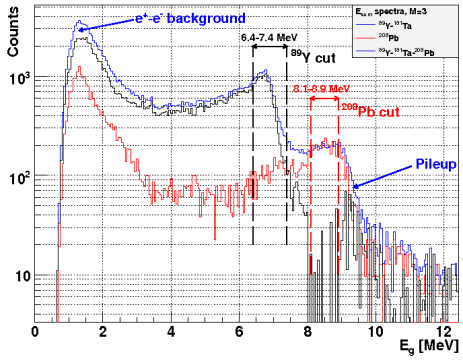

Figure 3.11: Subtraction of the ^{89}Y(n, el) background simulated through ^{208}Pb(n, el) within one E_n bin.

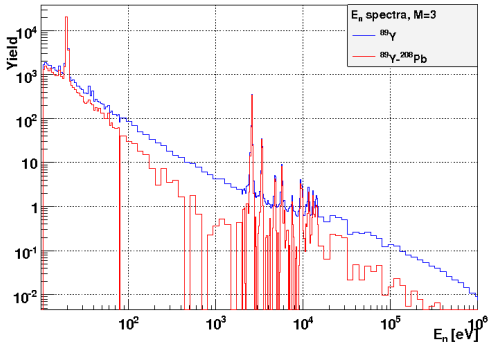

Figure 3.13: ^{89}Y(E_n) spectra before and after subtracting the ^{89}Y(n, el) background.

- ^{208}Pb(n, γ) – the red line. This cross section is very small (0.1 – 1 μbarn) up to E_n = 50 keV. Even at the resonances the capture is negligible compared to ^{208}Pb(n, el).
- ^{208}Pb(n, el) – the cyan line. The cross section is very similar to ^{89}Y(n, el) up to E_n = 70 keV.

The fact that the cross sections of ^{89}Y(n, el) and ^{208}Pb(n, γ) are so similar and that ^{208}Pb(n, γ) is very small, makes ^{208}Pb a very good candidate for the neutron scattering simulator. The region of interest of the ^{89}Y(n, γ) cross section is E_n = 10 eV – 300 keV. Neutron capture on ^{208}Pb can be a problem only above 70 keV, thus when subtracting the (n, el) background it is possible to over subtract because of the ^{208}Pb(n, γ) contribution. However, the Q-value of the ^{208}Pb(n, γ) reaction is 3.937 MeV, which is far below the 6.857 MeV value of ^{89}Y(n, γ). Applying cuts on E_{sum} solves the problem of background from neutron capture on ^{208}Pb.

The subtraction of the (n, el) background from the ^{89}Y data in some ways is similar to the subtraction of the Be background for the ^{157}Gd data (Sec. 2.3.8). The subtraction is performed for each neutron energy bin as follows:

- each E_n bin of the 2D histogram is projected onto the Y-axis and the E_{sum} spectra (Fig. 3.11) are built for ^{208}Pb (red line) and ^{89}Y (blue line) after the ^{181}Ta subtraction;
- The region above the Q-value of the ^{89}Y(n, γ) reaction is chosen for yield normalization. For ^{89}Y this is $E_{sum} = 8.1$ – 8.9 MeV;
- In this region the ^{208}Pb spectrum is normalized to the ^{89}Y spectrum with the normalization coefficient K_{Pb};
- $N(^{89}Y(n,\gamma)) = N(^{89}Y(n,\gamma) + ^{89}Y(n,el)) - N(^{208}Pb(n,el)) \cdot K_{Pb}$ is computed and the net result for the ^{89}Y neutron capture (black line) is obtained;
- To remove the $e^- - e^+$ pair production background and other residual backgrounds, a narrow cut around $E_{sum} = 6.857$ MeV is applied. The yield of this cut is the value for a given neutron energy bin.

More should be said about the K_{Pb} normalization coefficient. Naturally, it correlates with the cross sections of both the ^{89}Y(n, el) and ^{208}Pb(n, el) reactions. However, one should not expect to see a strong dependence of K_{Pb} on the ratio of these two cross sections. The (n, el) background results from multiple scattering on both the target and BaF_2 crystals. Therefore the scattered neutrons slow down inside the BaF_2 crystal for some time. This increases its TOF and, correspondingly decreases its energy. Thus, the (n, el) resonances are not observed in the E_n spectra – they are spread over the entire neutron energy region. Only the strongest (n, el) resonances can be seen in the $K_{Pb}(E_n)$ spectra (Fig. 3.12).

The ^{89}Y(E_n) spectra change drastically after subtracting the (n, el) background. In Fig. 3.13 two ^{89}Y spectra are presented – before (blue line) and after (red line) the background subtraction. The countss drop by up to 90–95% between resonances. Subtraction of large numbers close to each other results in a significant increase in the relative error – the more equal the numbers, the larger the relative error. For ^{89}Y the initial raw E_n spectra have good statistics with errors <1%, but after subracting the (n, el) background the error increases up to 5% at resonances and 20-50% between them. The problem is worse if the

^{208}Pb statistics are much less than that of ^{89}Y, because in that case the ^{208}Pb data first has to be normalized with the corresponding error. The best way to reduce the error is first to increase the statistics for both ^{89}Y and ^{208}Pb, and second to split the beam time between ^{89}Y and ^{208}Pb such that their total statistics are approximately equal and the error in calculating K_{Pb} is minimized. Additional beam time was allocated for the ^{89}Y experiment, and only two targets were studied – ^{89}Y and ^{208}Pb. The beam time was split to equalize the statistics for both targets.

3.3.5 Corrections for beam attenuation and target self shielding

Once all of the possible backgrounds are subtracted, there is nothing more to be done to the ^{89}Y data. However, some other parameters must be determined in order to calculate absolute values of the ^{89}Y(n,γ) cross section. First, consider Eq. 3.3 to calculate the neutron capture cross section:

$$\sigma_{n,\gamma}(E_n) = \frac{AN_{n,\gamma}(E_n)}{N_a \rho_s S N_n(E_n) \varepsilon_{tot} \varepsilon_{cut}} \tag{3.3}$$

Some parameters in this equation are known, but some must be determined. The parameters already known are:

- A=88.9$\frac{g}{mol}$ – the atomic mass of the ^{89}Y nucleus;
- N_a=6.022·10$^{23}\frac{1}{mol}$ – Avogadro's number;
- $\rho_s = 0.0653cm \cdot 4.472\frac{g}{cm^3} = 0.292\frac{g}{cm^2}$ – the areal density of the thick ^{89}Y target;
- $S = \frac{\pi}{4} \cdot (1.5cm)^2 = 1.767cm^2$ – the area of the target exposed to the beam;
- $\varepsilon_{tot} = 0.93$ – the efficiency of detecting at least 1 γ-quantum from an (n,γ)-event by DANCE;

The yet unknown parameters that can be determined from the experimental data are:

- $N_{n,\gamma}(E_n)$ – number of capture events per $cm^2 \cdot eV$ at a given neutron energy bin;
- $N_n(E_n)$ – number of neutrons per $cm^2 \cdot eV$ at a given neutron energy bin;
- ε_{cut} – the efficiency of detecting the γ-cascade after applying cuts on both E_{sum} and M_{cr}.

Eq. 3.3 is valid for thin targets where beam attenuation and target self shielding can be neglected, but is not valid for the ^{89}Y experiment. Self shielding and beam attenuation are relevant here and the $^{89}\mathrm{Y}(n,\gamma)$ cross section must be corrected for these issues. The $^{89}\mathrm{Y}(n,\gamma)$ cross section itself is small enough that it can be neglected for these purposes, but the $^{89}\mathrm{Y}(n,tot)$ cross section is large enough to attenuate the neutron beam and self shield neutron capture significantly, especially at resonances for the thick ^{89}Y target.

Attenuation of the neutron beam passing through the ^{89}Y target is calculated knowing the total cross section for neutrons interacting with ^{89}Y and the target thickness. The classic transmission experiment implies that the target is uniform, its size is larger the the beam spot, and the incident beam is parallel within the experimental geometry, i.e., no neutrons escape without being detected. The formula for the neutron beam attenuation is:

$$\Phi(E_n) = \Phi_0(E_n) \cdot e^{-\sigma_{tot}(E_n)x} \tag{3.4}$$

where $\Phi(E_n)$ is the intensity of the beam at a given neutron energy passing through the target; Φ_0 is the incident beam at a given E_n that hits the target; σ_{tot} is the $^{89}\mathrm{Y}(n,tot)$ cross section at a given E_n; and x is the target thickness. The $^{89}\mathrm{Y}(n,tot)$ cross section is 10^2–10^3 times larger than that of $^{89}\mathrm{Y}(n,\gamma)$, and therefore the total cross section is measured reasonably well: it was taken from the ENDF/B-VII library. The loss of beam intensity due to beam attenuation (blue line on Fig. 3.14) was calculated for the neutron energy range E_n = 10 eV – 1 MeV. The attenuation mostly varies within a few percent, but at resonances the beam be attenuated as much as 10%. The neutron beam was corrected for its attenuation in order to calculate the $^{89}\mathrm{Y}(n,\gamma)$ cross section correctly.

Target self shielding is the effect of reducing number of capture events due to beam attenuation that reduces the number of incident neutrons that cause capture events. The exact sequence that leads to self shielding is as follows:

- the incident beam hits the target with intensity Φ_0;
- due to the beam attenuation the beam intensity gradually reduces from Φ_0 to Φ while passing through the target. Thus the neutron capture intensity is larger at the front edge of the target than at the back edge;
- the total capture intensity is smaller than if it were caused by the beam of the Φ_0

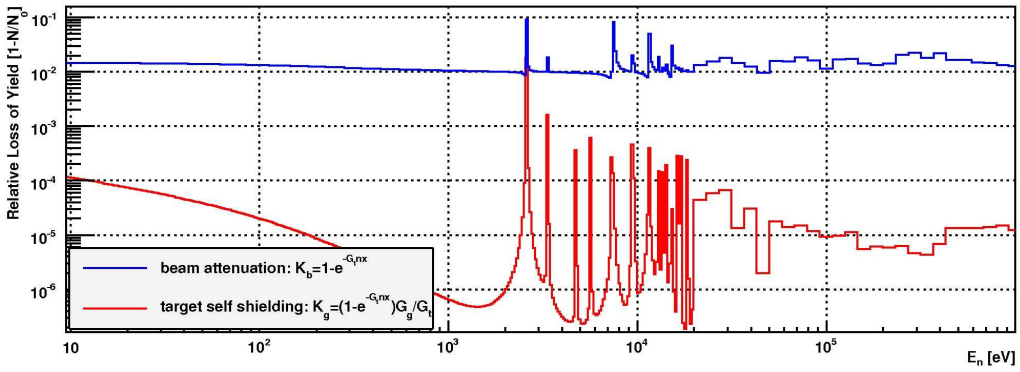

Figure 3.14: Self-shielding effects for ^{89}Y

intensity at the front target edge;

- some capture intensity is lost because some neutrons participate in reactions other than (n,γ); this loss is called target self shielding;

The formula for calculating the self shielding of neutron capture on a ^{89}Y target is:

$$\Phi = \Phi_0 \frac{1}{(1-e^{-\sigma_{tot}x})\frac{\sigma_{n,\gamma}}{\sigma_{tot}}} \tag{3.5}$$

where Φ is the observed DANCE (n,γ) intensity; Φ_0 is the true intensity of (n,γ) at the front edge of the ^{89}Y target; σ_{tot} the ^{89}Y(n,tot) cross section; $\sigma_{n,\gamma}$ the ^{89}Y(n,γ) cross section; and x the target thickness. The self shielding in ^{89}Y(n,γ) was calculated in the energy range E_n = 10 eV – 1 MeV using the ENDF/B-VII data as a source for both ^{89}Y(n,tot) and ^{89}Y(n,γ). The self shielding (red line on (Fig. 3.14)) is small in the entire E_n region except for the strongest resonance, where it reaches 7%.

The cumulative effect of beam attenuation and target self shielding is interesting. On one hand, the larger $\sigma_{n,tot}$, the more the beam is attenuated. On the other hand, large $\sigma_{n,tot}$ and x do not necessarily imply that self shielding is large as well; it is the ratio $\frac{\sigma_{n,\gamma}}{\sigma_{n,tot}}$ that is important. If neutron capture is dominant and the beam attenuation is large because of a very thick target, then the self-shielding effect will be small, since most neutrons that do not pass through the entire target are captured via the (n,γ) channel. Therefore, beam attenuation and target self shielding should be corrected separately.

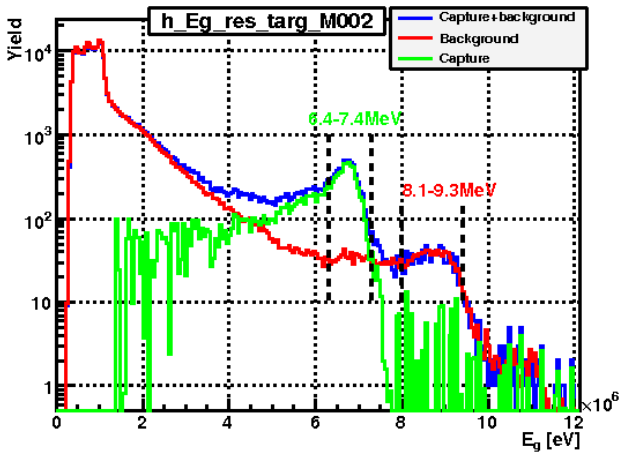

Figure 3.15: E_{sum} spectrum for $M_{cl} = 2$; The closer cut to the Q-value, the larger the signal-to-noise.

3.3.6 Processing losses – efficiency of cuts

One of the terms in Eq. 3.3 is the efficiency ε_{cut} of the cuts. This is the efficiency of detecting a γ-cascade after applying cuts on E_{sum} and M_{cl}. This efficiency is equal to the ratio $\frac{Y_{cut}}{Y_{tot}}$ of two yields, where:

1. Y_{tot} is the total yield of the γ-cascade, including all M_{cl} and the range of $E_{sum} = 0.0$ – 7.4 MeV;

2. Y_{cut} is the yield of the γ-cascade for the range $M_{cl} = 4$ – 6, and $E_{sum} = 6.4$ – 7.4 MeV;

These cuts on M_{cl} and E_{sum} are absolutely necessary for the ^{89}Y data; it is the last chance to reduce residual backgrounds to the level of error uncertainties. The shape of E_{sum} spectra for any E_n range follows a similar dependence on multiplicity and E_{sum} energy: the larger M_{cl} and the closer E_{sum} is to the Q-value, the lower the background. An example of how ε_{cut} was determined for the ^{89}Y data is shown in Fig. 3.15. This is an E_{sum} spectrum gated on the 4.779-keV resonance. The green line is the capture cascade after subtracting backgrounds.

First, the total area A_{E_{tot},M_i} of the E_{sum} spectrum is calculated in the range E_{sum} = 0 – 7.4 MeV, which is somewhat higher than the 6.857-MeV Q-value of ^{89}Y(n,γ) because the pulse height function from the BaF_2 crystal is broadened. A_{tot} is the sum of areas

A_{E_{tot},M_i} calculated for all of the practical multiplicities $M_{cl} = 1 - 9$:

$$A_{tot} = \sum_{M_{cl}=1}^{9} A(E_{tot}, M_i) \tag{3.6}$$

Second, the same area is calculated for a certain E_{sum} range and certain M_{cl}s. The E_{sum} range is around 6.857 MeV, the Q-value of ^{89}Y(n,γ), and it chosen to be E_{sum} = 6.4 – 7.4 MeV. The lower bound is determined by the 6.063 MeV Q-value of the ^{181}Ta contaminant. The upper bound should be close to 6.857 MeV, and is determined from the E_{sum} shape to maximize signal-to-noise. The multiplicities also were chosen to maximize the signal-to-noise ratio, For ^{89}Y the range was $M_{cl} = 4 - 6$.

$$A_{cut} = \sum_{M_{cl}=4}^{6} A(E_{cut}, M_i) \tag{3.7}$$

Third, the yields Y_{tot} and Y_{cut} correspond to the areas A_{tot} and A_{cut}, respectively. Thus the ratio of areas is the efficiency:

$$\varepsilon_{cut} = \frac{A_{cut}}{A_{tot}} \tag{3.8}$$

For ^{89}Y the cut efficiency is equal to 0.118(2), where the 0.002 error is the statistical error.

When calculating A_{tot}, the E_{sum} range may include low energy backgrounds. At low multiplicities ($M_{cl} = 1 - 2$) the residual annihilation background may still impact the data. As can be seem from the shape of the E_{sum} spectrum (green line on Fig. 3.15), at lower E_{sum} the cascade contribution is small. Therefore, if the residual background is relatively high at lower E_{sum}, the lower bound of the area integration should be increased by ∼1 MeV to cut off the annihilation background. This should be done only for low – M_{cl} = 1 and 2 – since at higher M_{cr} >2 the residual background left after subtraction is small. If such a cut off is performed, computer simulations may help in determining how much of the cascade was removed. Normally, losses of useful data due to such cuts do not exceed 3–5% percent of the total area at a given M_{cl}. It is less than 2% of the total area of all M_{cr}s. The ε_{cut} error margin is correspondingly increased.

3.3.7 Neutron flux determination using ^{197}Au as a reference

The absolute neutron flux at the target location is one of the terms in Eq. 3.3. $N_n(E_n)$ is the number of neutrons per $cm^2 \cdot eV$ in a given neutron energy bin. Three beam monitors are used at DANCE, which measure the neutron flux at ∼2 m away from the target in the center of DANCE. These beam monitors cannot directly determine the beam flux at the target location. Instead a reference target is measured with DANCE. The reference target has to satisfy the following simple requirements:

- has to be of the same size and geometry as the ^{89}Y target;
- the (n, γ) cross section has to be well known;
- the (n, el) cross section must be small in order to reduce background;
- the target should have an isolated (n, γ) resonance in the E_n range of DANCE;

One of the available isotopes is ^{197}Au. Several ^{197}Au targets were used to determine the neutron flux at DANCE. The best target was considered to be the 1 μm thick self-supported foil. The ^{197}Au target thickness and uniformity, are known with 10% accuracy.

To determine the neutron flux at the target location, Eq. 3.3 is used but in a different order. For reasons of space the ^{197}Au experiment will not be described in full detail, but it will be explained how the ^{197}Au data was used in order to determine the neutron flux for the ^{89}Y experiment.

The goal is to determine the neutron flux at the target location $N_n(E_n)$, but because beam monitors are located 2 m downstream from the target, the best option is to use the known ^{197}Au(n, γ) cross section to determine the ratio $\frac{N_{n,\gamma}(E_n)}{N_n(E_n)}$ for the ^{197}Au experiment and then to use this ratio to determine the ^{89}Y(n, γ) cross section in Eq. 3.3.

The ^{197}Au experimental setup is similar to that of ^{89}Y. The ^{197}Au target was located at the same place that the ^{89}Y was located. Since the 12 hour measurements were taken immediately after measuring ^{89}Y, the parameters of the DAQ, the neutron beam, and the beam monitor settings change very little. The data analysis is similar to those of both ^{89}Y and ^{157}Gd up to the point where background is subtracted.

The only region of interest is around the 4.9-eV resonance. Since the target is a self-supported foil, the (n, el) background is subtracted from the 4.9-eV resonance in the

same fashion as was done for the ^{89}Y data. The only difference is that for ^{89}Y the ^{9}Be data is used, but the ^{197}Au data has no associated ^{9}Be spectra. The narrow region on both sides of the 4.9-eV resonance is considered as the background, and is subtracted as in Sec. 3.3.4.

Then the neutron spectra of all M_{cl}s are summed and the single neutron spectrum of ^{197}Au is used. The 4.9-eV resonance of ^{197}Au(n,γ) is the best candidate for an isolated resonance with a well known cross section. The same Eq. 3.3 is applied to the ^{197}Au data, but the only unknown parameter here is $N_n(E_n)$:

$$N_n(E_n) = \frac{AN_{n,\gamma}(E_n)}{N_a\rho_s S\sigma_{n,\gamma}(E_n)\varepsilon_{tot}\varepsilon_{cut}} \tag{3.9}$$

where $\sigma_{n,\gamma}(E_n)$ is the cross section at the 4.9-eV resonance, $\varepsilon_{tot} = 100\%$, and the remaining parameters have the same meaning as for ^{89}Y but with different values.

The 4.9-eV resonance must be fit to the ENDF/B-VII spectrum of ^{197}Au(n,γ), and the fitting coefficient is used for the ^{89}Y data in the entire E_n range. Rewrite Eq. 3.3 as follows:

$$\sigma_{n,\gamma}(4.9eV) = \frac{N_{n,\gamma}(4.9eV)}{K_S N_n(4.9eV)} \tag{3.10}$$

The denominator $K_S N_n$ here depends only on the experimental setup, and since it is the same for ^{89}Y and ^{197}Au, $K_S N_n$ is the same for both targets. N_n is known from the beam monitor data for each data set, and K_S for ^{197}Au is determined by fitting the 4.9-eV resonance of ^{197}Au to that of ENDF. The fitting is done with SAMMY [24], a code for analysis in cross the resonance regions.

3.3.8 Determination of the ^{89}Y(n,γ) cross section

The last step in the ^{89}Y data analysis is to collect all of the parameters of Eq. 3.3 and calculate the ^{89}Y(n,γ) cross section. There were three unknown parameters:

- $N_{n,\gamma}(E_n)$ – number of capture events per $cm^2 \cdot eV$ at a given neutron energy bin;
- $N_n(E_n)$ – number of neutrons per $cm^2 \cdot eV$ at a given neutron energy bin;
- ε_{cut} – the efficiency of detecting the γ-cascade after applying cuts on both E_{sum} and M_{cl}.

Once the efficiency cut ε_{cut} is determined, the ^{89}Y neutron spectra are summed over the M_{cl}s, for which the ε_{cut} was applied, into a single E_n spectrum. $N_{n,\gamma}(E_i)$ is the number of counts in the E_i neutron energy bin of the ^{89}Y spectrum. $N_n(E_i)$ is number of counts in the same E_i bin of the beam monitor spectrum.

To calculate the cross section Eq. 3.3 has to be applied for each E_n bin of the ^{89}Y and beam monitor spectra. The only change to be made in Eq. 3.3 is to account for one additional term K_S that comes from determination of the neutron flux using SAMMY fitting of the 4.9-eV resonance of ^{197}Au(n,γ). Thus, the new formula for the cross section is:

$$\sigma_{n,\gamma}(E_n) = \frac{AN_{n,\gamma}(E_n)}{N_a\rho_s S K_S N_n(E_n)\varepsilon_{tot}\varepsilon_{cut}} \tag{3.11}$$

where K_S is a normalization coefficient derived from the determination of the absolute neutron flux. All other terms have the same meaning as in Eq. 3.3. The difference between equations 3.3 and 3.11 is that the latter equation calculates the absolute cross section. The cross section unit is $[cm^2]$, which can be converted into $[barn]$ with the relation $1[b] = 10^{-24}[cm^2]$.

3.4 Discussion of results

The main goal of the ^{89}Y experiment was to determine the absolute cross section of ^{89}Y(n,γ), where "absolute" means independently from nuclear data libraries such as ENDF/B-VII, JENL, and JEFF. However, for correct determination of the ^{89}Y(n,γ) cross section, a ^{197}Au target was used to determine the intensity of the incident neutron beam. The well-isolated ^{197}Au(n,γ) resonance at $E_n = 4.9$ eV served as a reference standard for calculating the absolute neutron flux. Thus the neutron capture cross section on ^{89}Y is linked to the 4.9-eV resonance in ^{197}Au. Nevertheless, the ^{89}Y(n,γ) cross section is said to be determined absolutely, since the 4.9-eV resonance in ^{197}Au is very well known and has cross section errors of a fraction of 1%, which is far less than the uncertainties in the ^{89}Y(n,γ) cross section.

The neutron capture cross section is not the only information obtained from DANCE data. Resonance spectroscopy is also possible under favorable conditions. For ^{157}Gd (Sec. 2.4.2) spin assignment techniques were successfully used to determine resonance spins and photon strength functions (PSFs) were obtained from the γ-ray cascade

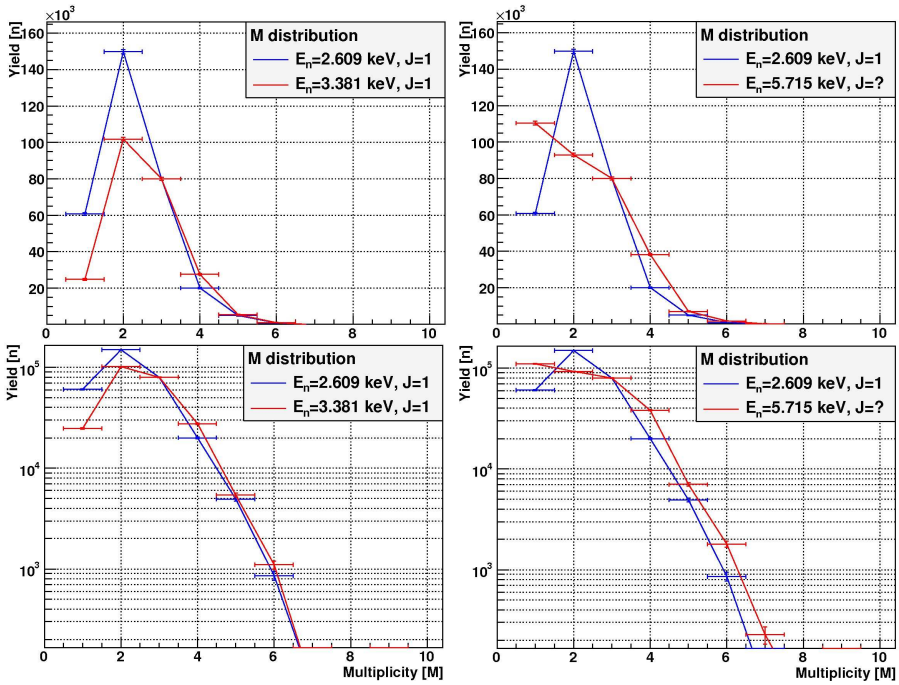

Figure 3.16: The M distributions for ^{89}Y are not as distinctive as for ^{157}Gd.

data. However, for ^{89}Y the data is adequate to perform the resonance spectroscopy that worked well for the ^{157}Gd data.

3.4.1 Spin assignments in ^{89}Y resonances

The resonance spectroscopy and spin assignment techniques applied to the ^{157}Gd (Sec. 2.4.2) data were also attempted for ^{89}Y, but the results are quite different for these two nuclei.

The Koehler method [28] was tested on the ^{89}Y data. The range of cluster multiplicity M_{cl} is 1 to 6. The M_{cl} distributions for the two strongest resonances at $E_1 = 2.6$ keV (blue line) and $E_1 = 3.4$ keV (red line) are shown in Fig. 3.16. In principal it is possible to determine the average multiplicity for either resonance; but the statistics of capture events are too low and the two M_{cl} distributions are similar within t errors. Thus, this method provides no information about the spin from the γ-ray multiplicity even for the strongest resonances because of the low statistics and target contaminants with background. The verdict is that this method does not work even for the strongest resonances.

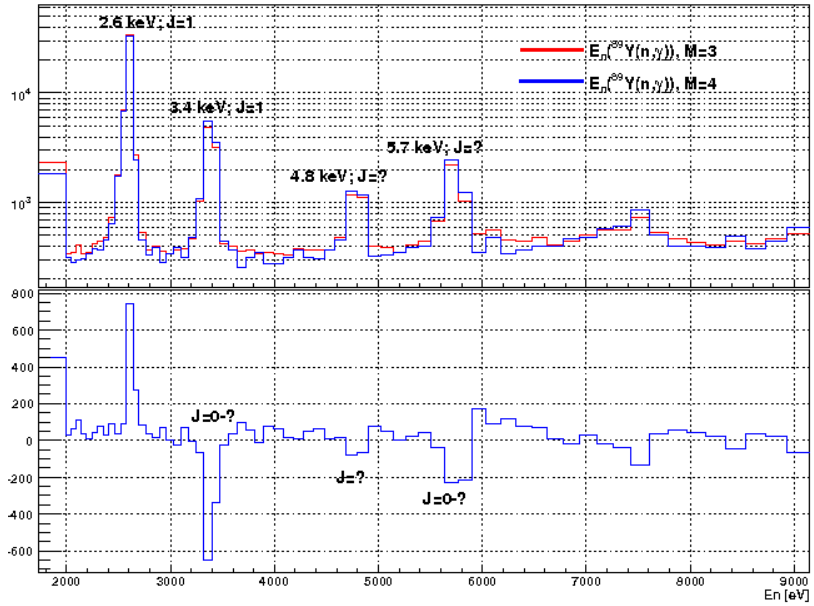

Figure 3.17: Cross section of ^{157}Gd(n, el): DANCE vs. ENDF/B-VII.

The method that I developed, using direct comparison of E_n spectra for different values of M_{cl}, was also applied to the ^{89}Y data. The best signal-to-noise ratio is observed for the multiplicity ratio $\frac{M_{cl}=3}{M_{cl}=4}$, thus, the use of these two spectra (see Fig. 3.17) should give the best results with this spin assignment method. The results are inconsistent: at resonance energies peaks and dips are observed, but on the other hand some maxima and minima are present at energies where there are no resonances. Also, the DANCE data for the 3.4-keV resonance seems to disagree with the accepted $J = 1$ assignment. Therefore, the verdict here is the same as for the Koehler method – no reliable spin assignment is possible for the ^{89}Y data.

The most advanced and sensitive technique is the Becvar method [29]. The neutron spectra for $M_{cl} = 3$ to 6 were decomposed and an attempt at spin assignments was made. But this method turned to be most sensitive to backgrounds. The ^{89}Y data was initially heavily contaminated with both ^{181}Ta(n, γ) and ^{89}Y(n, el) backgrounds. In the data analysis most of the backgrounds were removed by first subtraction and then placing cuts on E_{sum} around the Q-value of the ^{89}Y(n, γ) reaction. While this works well for the cross section determination, the remaining data are not good enough to decompose the E_n spectra with the Becvar technique. Thus the most sensitive method in the ^{157}Gd analysis does not help

determine spin assignments for the ^{89}Y data.

All of the three spin assignment methods are not applicable for the ^{89}Y data for the following reasons:

- the statistics of capture events are low, and thus the M_{cl} distributions for different spins are the same within errors;
- the residual background spoils the very weak spin dependence from M_{cl};
- only the strongest 3 resonances are distinguished well enough for resonance spectroscopy. Most of the resonances are too dense for the DANCE timing hardware to resolve;

3.4.2 ^{89}Y(n,γ) cross sections for 3 targets

The absolute values of the ^{89}Y(n,γ) cross section were determined for three targets of different thicknesses – thin (1 mil), medium (5 mil), thick (25 mil). The three cross sections are equal within errors, but the accuracy is different. In Fig. 3.18-3.20 the DANCE cross sections from the three targets are compared to the ENDF/B-VII data.

The thin target cross section (Fig. 3.18) has the poorest accuracy of the three data sets, not because of statistics, but because of the background subtractions. The errors vary: 10-20% at resonances, up to 80% in dips, and 50% at E_n = 10 keV – 30 keV.

The medium target cross section (Fig. 3.19) also has relatively large errors since the beam time dedicated to this one was less than the other targets. The accuracy varies depending on E_n: 10-20% at resonances, 50-80% in dips, and 30 – 50% at E_n = 10 keV – 30 keV.

The accuracy of the thick target cross section (Fig. 3.20) is the best due to improved statistics and thus better background subtraction. An additional 7 days of beam time were spent to improve the statistics on this 25-mil target, as well as 4 additional days of measurements for the ^{208}Pb target. The background subtraction is the main contribution to the errors in the ^{89}Y(n,γ) cross section. Thus it is important to have better statistics not just on ^{89}Y, but also on the ^{208}Pb target, since it serves to simulate the (n,el) background.

Overall the accuracy of the ^{89}Y(n,γ) cross section was improved by up to 30% after taking additional data on both the thick yttrium and lead targets.

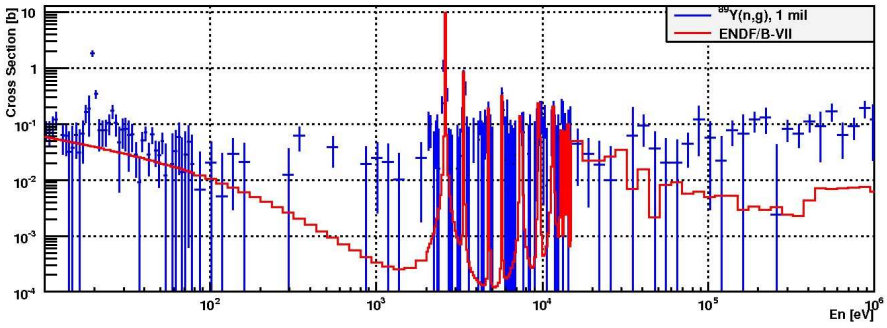

Figure 3.18: $^{89}\mathrm{Y}(n,\gamma)$ measured for the 1 mil thin target with DANCE.

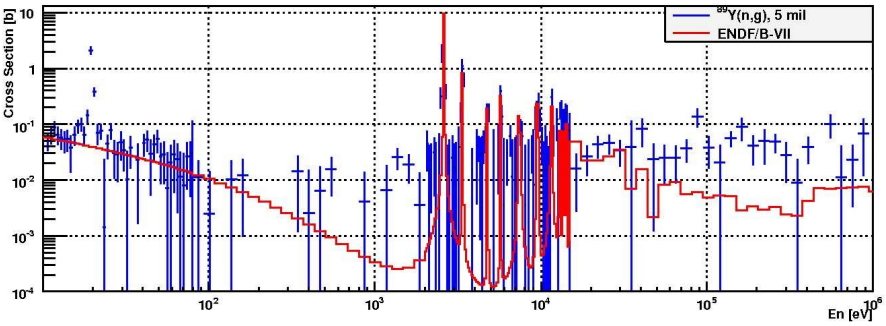

Figure 3.19: $^{89}\mathrm{Y}(n,\gamma)$ measured for the 5 mil medium target with DANCE.

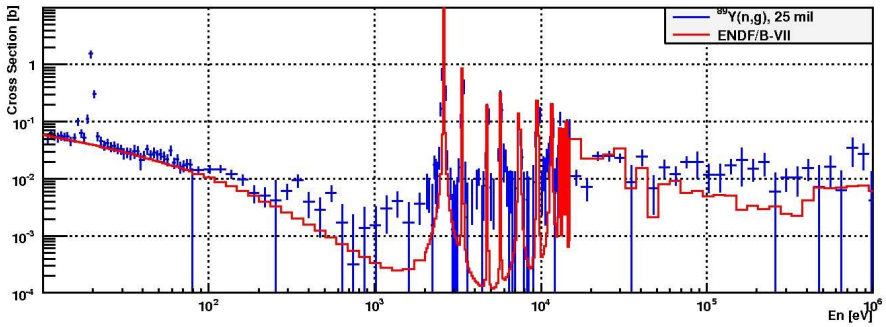

Figure 3.20: $^{89}\mathrm{Y}(n,\gamma)$ measured for the 25 mil thick target with DANCE.

3.4.3 Comparison of DANCE data with ENDF and EXFOR

After the ^{89}Y(n,γ) cross section was determined, the last thing to do was to compare the data to other measurements and evaluations. Neutron capture on ^{89}Y was both measured and evaluated before the DANCE experiment. The evaluated data libraries for the ^{89}Y(n,γ) cross section are ENDF/B-VII (USA, 2006), JEFF-3.1 (Europe, 2005), and JENDL-3.3 (Japan, 2002). The ENDF/B-VI (USA, 2001) library is not included since it was updated to ENDF/B-VII. The experimental data sets are the current DANCE data and the EXFOR library. The latter contains point-wise cross section data with the width of each E_n bin and the errors on cross section given.

In Fig. 3.21 the DANCE data and the evaluated data are compared. The first thing to notice is the striking difference in cross sections between different sources. JENDL-3.3 has the resonance region resolved up to $E_n = 45$ keV; the JEFF resonance data goes up to 150 keV; and ENDF/B-VII contains resonance structure up to 400 keV.

The most striking difference between evaluated data sets is the regions between resonances. Different cross sections are equal until $E_n = 10$ eV and then start to deviate from each other. At $E_n = 1$ keV ENDF/B-VII and JENDL-3.3 cross sections are 10 – 15 times lower than the JEFF-3.1 cross section. This large difference continues until the region where resonances are not resolved, up to 150 keV. Above this energy the difference in cross sections is much smaller, "only" 30%. It should be noted that the evaluated data provides no errors, and thus the large difference could be explained by small cross sections: the range of the ^{89}Y(n,γ) cross section is 1 – 10 mbarn between resonances, while at resonances the cross sections can be as large as 10 – 100 barn. The ratio of the cross sections at resonances and in dips can be as large as a factor of 10^4.

The DANCE ^{89}Y(n,γ) cross section was determined independently from any evaluated data. The E_n bin width is chosen so that a compromise is made between the errors, which should be minimized, and the resonance structure, which is preserved within reasonable limits. The DANCE data (blue line on Fig. 3.21) is close to the evaluated data sets within errors everywhere except between resonances. At higher energies, $E_n \geqslant 10$ keV, where the cross section is averaged with wider E_n bins, the DANCE results are similar to JENDL-3.3 and JEFF-3.1, but higher than ENDF/B-VII. The DANCE cross section between resonances is larger, probably due to resonance broadening.

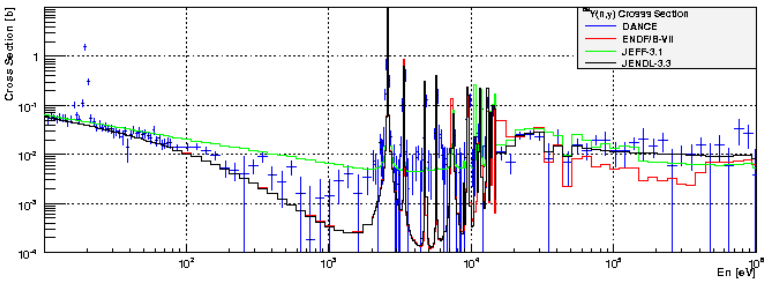

Figure 3.21: ^{89}Y(n,γ): DANCE vs. evaluated data libraries.

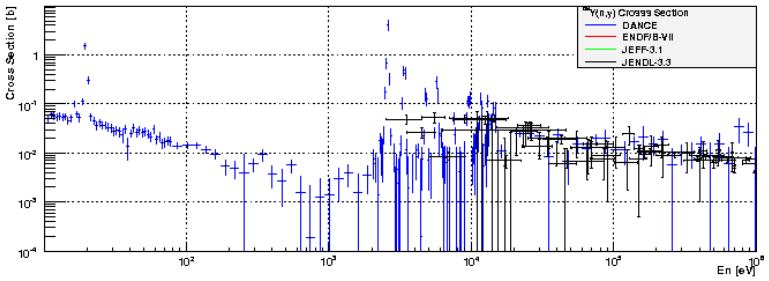

Figure 3.22: ^{89}Y(n,γ): DANCE vs. other experimental data.

The EXFOR library [22] is a collection of experimental data sets. When comparing the DANCE data to the EXFOR cross sections (Fig. 3.22), it seems that the agreement is much better with the evaluated data sets. The EXFOR data has fewer points, wider E_n bins, and larger errors on the cross section, than do the DANCE data. The most important thing to notice is the number of cross section points. The EXFOR data starts at $E_n = 3.5$ keV and goes up to 10 MeV, with ∼100 points. The DANCE data starts at $E_n = 10$ eV and ranges over 5 neutron energy decades up to 300 keV with a few hundred cross section points. The DANCE data is better than any previous experimental data by the following critria: E_n range, number of data points, energy resolution, and accuracy.

3.4.4 Summary

The DANCE capture measurements on ^{89}Y were performed in two stages: the main portion of the data was collected in 2008, and better statistics were obtained in 2009. The three ^{89}Y targets, 1 mil, 5 mil, and 25 mil, thick self-supported foils were measured and the ^{89}Y(n,γ) cross section was determined for each of them using the same physical settings. A ^{197}Au self-supported target of 100 $\frac{mg}{cm^2}$ thickness was used to determine the neutron flux

at the target position through the use of the 4.9-eV resonance in ^{197}Au(n,γ), which has a well determined cross section. More targets of different shapes, sizes, and isotopes were measured to simulate the ^{89}Y(n,el) background: ^{nat}Fe, ^{nat}Pb, and ^{208}Pb. The ^{208}Pb data set was best for the background subtraction. One additional ^{181}Ta target was measured to account for the ^{181}Ta contamination background in the ^{89}Y targets. In total, data were collected from 7 different targets. The results from only 3 of them are presented here.

The main challenge in the data analysis was the neutron scattering background. It contributed to ∼90% of the total count rate when measuring the ^{89}Y targets. To subtract this type of background the ^{208}Pb target with a large $\frac{\sigma(n,el)}{\sigma(n,\gamma)}$ ratio was successfully used to simulate the ^{89}Y(n,el) reaction.

The cross section results were compared with those of evaluated nuclear data libraries and other experimental data sets. The agreement between the DANCE and evaluated data sets is reasonably good within errors at resonances and off-resonances regions: 10 eV – 1 keV, 10 keV – 300 keV; but the difference is larger between resonances. The agreement between DANCE data and other experiments is very good at higher energies $E_n \geqslant$ 10 keV, because the DANCE results are of much better quality than any other experiment previously performed. The DANCE results include more points, better energy resolution, smaller errors, and even some resonances are resolved.

The ^{89}Y experiment revealed some of the limitations of DANCE. The smallest values of the ^{89}Y(n,γ) cross section points are at $\sim 10^{-2}$ b with 50% error; the largest values are at $\sim$ 100 b. Thus, the dynamic range of the measured neutron capture cross section is 4 orders of magnitude. At this moment, ^{89}Y(n,γ) has the smallest cross section, and the largest ratio $\frac{\sigma(n,el)}{\sigma(n,\gamma)}$, and thus the lowest signal-to-noise ratio, of all of the isotopes measured with DANCE. And all this was possible for the imperfect ^{89}Y targets contaminated with other nuclei.

Resonance spectroscopy was not possible to perform with these data because the signal-to-noise is not sufficient for this type of analysis. The spin determination techniques produced no results to compare with the latest literature data [31]. The resonance density is too high for the DANCE timing hardware to resolve most of the resonances.

Bibliography

[1] *The Los Alamos National Laboratory Spallation Neutron Sources.*
P.W. Lisowski, C.D. Bowman, G.J. Russell, S.A. Wender.
Nuclear Science and Engineering: 106, 208-218, 1990.
University of California, Los Alamos National Laboratory Physics Division, Los Alamos, NM 87545, Oct 17, 1989.

[2] *Performance of the LANCE-WNR Facility as an Intense Pulsed Neutron Source for Neutron Nuclear Physics.*
A.F. Michaudon, S.A. Wender.
Los Alamos National Laboratory, LA-UR-90-4355.

[3] *Monte Carlo study of the neutron emission spectra at the Manuel Lujan Jr. Neutron Scattering Center.*
M. Mocko, G. Muhrer, T. Ino, M. Ooi, L.L. Daemen, Y. Kiyanagi.
Nuclear Instruments and Methods in Physics Research A, 594 (2008), p. 373-381, `www.elsevier.com/locate/nima`

[4] *LANSCE Facilities for High-Power Target Development.*
Steve Wender.
2nd High-Power Targetry Workshop, Oak Ridge, TN, October 10-14, 2005.

[5] *n_TOF - The neutron facility at CERN.*
n_TOF collaboration.
`http://pceet075.cern.ch/`

[6] *A 4π BaF_2 detector for (n,γ) cross-section measurements at a spallation neutron source.*
M. Heil, R. Reifarth, M.M. Fowler, R.C. Haight, F. Kappeler, R.S. Rundberg, E.H. Seabury, J.L. Ullmann, J.B. Wilhelmy, K. Wishhak.
Nuclear Instruments and Methods in Physics Research A 459 (2001) 229-246.

[7] *Acquisition - Analysis System for the DANCE (Detector for Advanced Neutron Capture Experiment) BaF_2 Gamma-Ray Calorimeter.*
J.M. Wouters, T.A. Bredeweg, E. Esch, R.C. Haight, J.M. O'Donnell, R. Reifarth, R.S. Rundberg, J.M. Schwantes, J.L. Ullmann, D.J. Vieira, L.B. Wilhelmy, A. Alpizar-Vicente, R. Hatarik, S.A. Sheets.

[8] *Acqiris Corporation, 18.*
Chemin des Auls 1228 Plan-les-Quates, Geneva, Switzerland.

[9] *Red Hat Inc.*
Varsity Drive, Raleigh, NC 27606, USA.
http://www.redhat.com/

[10] *MIDAS - Maximum Integration Data Acquisition System.*
S. Ritt, P.-A. Amaudruz, unpublished.
https://midas.psi.ch

[11] *ROOT - An Object-Oriented Data Analysis Framework.*
Rene Brun and ROOT collaborators.
http://root.cern.ch/root

[12] *Lawrence Livermore National Laboratory.*
7000 East Avenue, Livermore, CA 94550, USA.
http://www.llnl.gov

[13] *Gadolinium.*
http://www.ncnr.nist.gov/resources/n-lengths/elements/gd.html

[14] *Berrylium.*
http://periodic.lanl.gov/elements/4.html

[15] *CANDU - CANada Deuterium Uranium Reactor.*
Atomic Energy of Canada Limited.
http://www.aecl/ca

[16] *GNU compression utility.*
http://www.gzip.org

[17] *Third extended file system - a journaled file system for Linux kernel.*
S. Tweedie.
http://olstrans.sourceforge.net/release/OLS2000-ext3/OLS2000-ext3.html

[18] *Root based Object oriented Midas Extenstion.*
https://midas.psi.ch/rome/

[19] *Gas gain on single wire chambers filled with pure isobutane at low pressure.*
YU.I. Davydov, R. Openshaw, V. Selivanov, G. Sheffer.
TRIUMF, 4004 Westbrook Mall, Vancouver, BC, Canada V6T 2A3.
RRC Kurchatov Institute, Kurchatov sq.1, Moscow, 123182, Russia.
http://adsabs.harvard.edu/abs/2004physics..10004D

[20] *LND, INC. Designers and Manufacturers of Nuclear Radiation Detectors.*
Oceanside, New York, USA.
http://www.lndinc.com

[21] *Yttrium.*
http://periodic.lanl.gov/elements/39.html

[22] *Evaluated Nuclear Data File (ENDF/B-VII).*
http://www.nndc.bnl.gov/exfor/endf00.jsp

[23] *Alfa Aesar. A Johnson Mattey Company.*
30 Bond St., Ward Hill, MA 01835, USA.
`http://www.alfa.com`

[24] *The SAMMY code. An R-matrix tool for analysis of cross section data in the resolved and unresolved resonance regions .*
Oak Ridge National Laboratory, P.O. Box 2008, Oak Ridge, TN 37831, USA.
`http://www.ornl.gov/sci/nuclear_science_technology/nuclear_data/sammy/`

[25] *Neutron Capture and Total Cross-Section Measurements and Resonance Parameters of Gadolinium.*
G. Leinweberm, D.P. Barry, M.J. Trbovich, J.A. Burke, N.J. Drindak, H.D. Knox, R.V. Ballad, R.C. Block, Y. Danon, L.I. Severnyak.
Nuclear Science and Engineering: 154, 261-279 (2006).

[26] *Facility and method for studying two-step γ cascades in thermanl neutron capture.*
J. Honzatko, K. Konechny, I. Tomandl, J. Vacik, F. Becvar, P. Cejnar.
Nuclear Instruments and Methods. **A376**, 434 (1996).

[27] *Test of the statistical model in ^{96}Mo with the BaF_2 γ-calorimeter DANCE array.*
S.A. Sheets, U. Agvaanlusan, J.A. Becker, F. Becvar, T.A. Bredeweg, R.C. Haight, M. Jandel, M. Kritcka, G.E. Mitchell, J.M. O'Donnell, W. Parker, R. Reifrath, R.S. Rundberg, E.I. Sharapov, J.L. Ullmann, D.J. Vieira, J.B. Wilhelmy, J.M. Wouters, C.Y. Wu.
Physical Review C **79**, 024301 (2009).

[28] P.E. Koehler, J.L. Ullmann, T.A. Bredeweg, J.M. O'Donnell, R. Reifarth, R.S. Rundberg, D.J. Vieira, J.M. Wouters.
Phys. Rev. C **76**, 025804 (2007).

[29] *Optimized γ-multiplicity based spin assignments of neutron resonances.*
F. Becvar, P.E. Koehler, M. Krticka, G.E. Mitchell, J.L. Ullmann.
Preprint submitted to Nuclear Instruments and Methods A.

[30] *Photon Strength Functions in Rare-Earth Nuclei Studied from Slow Neutron Capture.*
Milan Krticka, Ph.D. Thesis, Charles University in Prague, Faculty of Mathematics and Physics, Apr 2002.

[31] *Atlas of Neutron Resonances.*
S.F. Mughabghab.
National Nuclear Data Center, Brookhaven National Laboratory, 2006.
`http://www.nndc.bnl.gov/atlas`

[32] D.M. Brink, Thesis, Oxford University, 1955, pp. 101-110.
P. Axel, Phys. Rev. 126 (1962) 671.

Appendices

Appendix A

Results on ^{157}Gd

A.1 List of additional figures for ^{157}Gd

The following figures represent results for the spin assignment and resolved (n, γ) resonances in ^{157}Gd.

The figures A.1 – A.6 illustrate the results on author's spin assignment mehtod. The results for each $M_i - M_j$ combination includes two figures. The top figure contains 2 E_n spectra normalized to each other at the 20.56-eV resonance. The red line is the E_n spectrum for M_i, and the blue line is the E_n spectrum for M_j. The bottom figure contains 1 E_n spectrum, which is a difference $M_i - M_j$ between the top two spectra.

The figures A.9 – A.35 are the M_{cl} distributions of the ^{157}Gd(n, γ) resonances from 21.54 eV to 194.37 eV, these figures represent the results on the Koehler's spin assignment method. Each figure contains two M_{cl} distributions: the red line for the certain i-resonance with unknown spin J_i, and the blue line for the 20.56-eV resonance with the known spin $J = 2$.

The figures A.36 – A.42 are the results of the Becvar's spin assignment method in the range $E_n = 20$ – 670 eV. Each figure has 3 E_n spectra for within a certain range of E_n. The black line is the raw yield (counts) of ^{157}Gd(n, γ). The green line is the decomposed E_n spectrum of the J=2 function. The red line is the decomposed E_n spectrum of the J=1 function. The spin assignment for a particular resonance is based on the ratio: green line vs. red line. If the red line yield is more than the green line yield, it corresponds to the spin $J = 1$ being more likely than the spin $J = 2$ for that resonance. At some energy an up

the two yields start to look similar within error bars, this energy is where spin assignment ends. The last reliable spin assignment is made at $E_n = 319$ eV. The last spin assignment with this method is made at $E_n = 593$ eV.

The figures A.43 – A.46 are the raw E_n spectra of $^{157}\mathrm{Gd}(n,\gamma)$ with the high energy resolution to distinguish as many resonance as possible. The continuous mode data contains the first resonance at 20.56 eV and the last resolved resonance at 1074 eV.

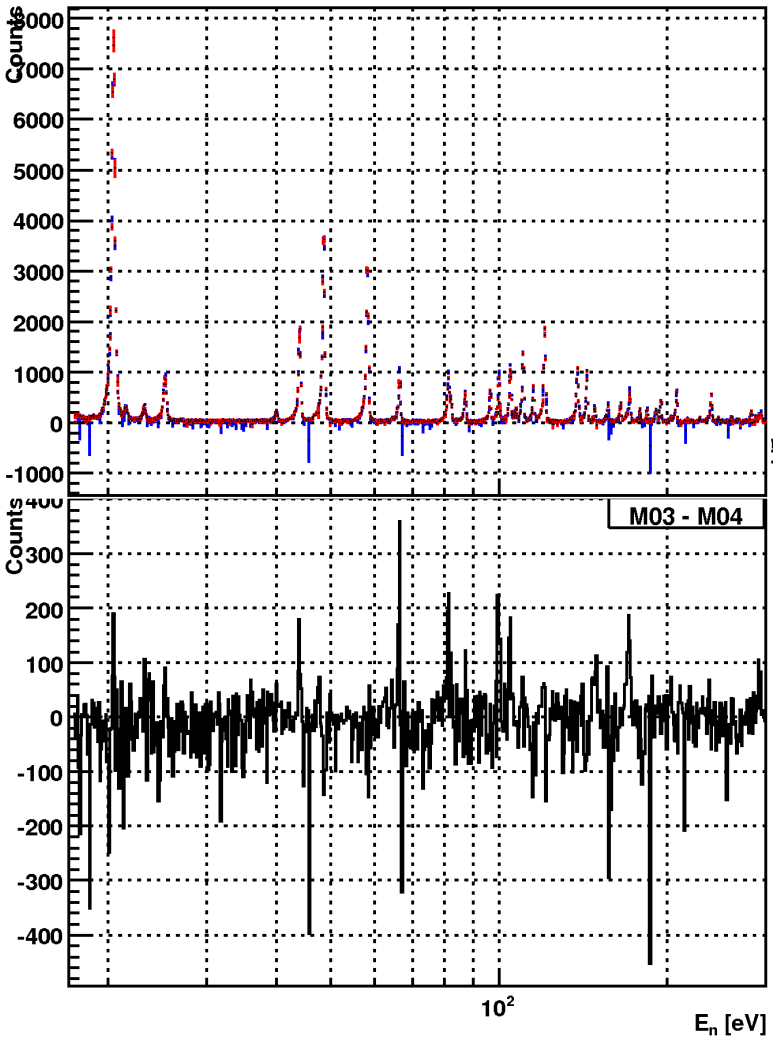

Figure A.1: Spin assignment for $J = 1$ resonances. E_n spectra of $M_1 = 3$ vs. $M_2 = 4$.

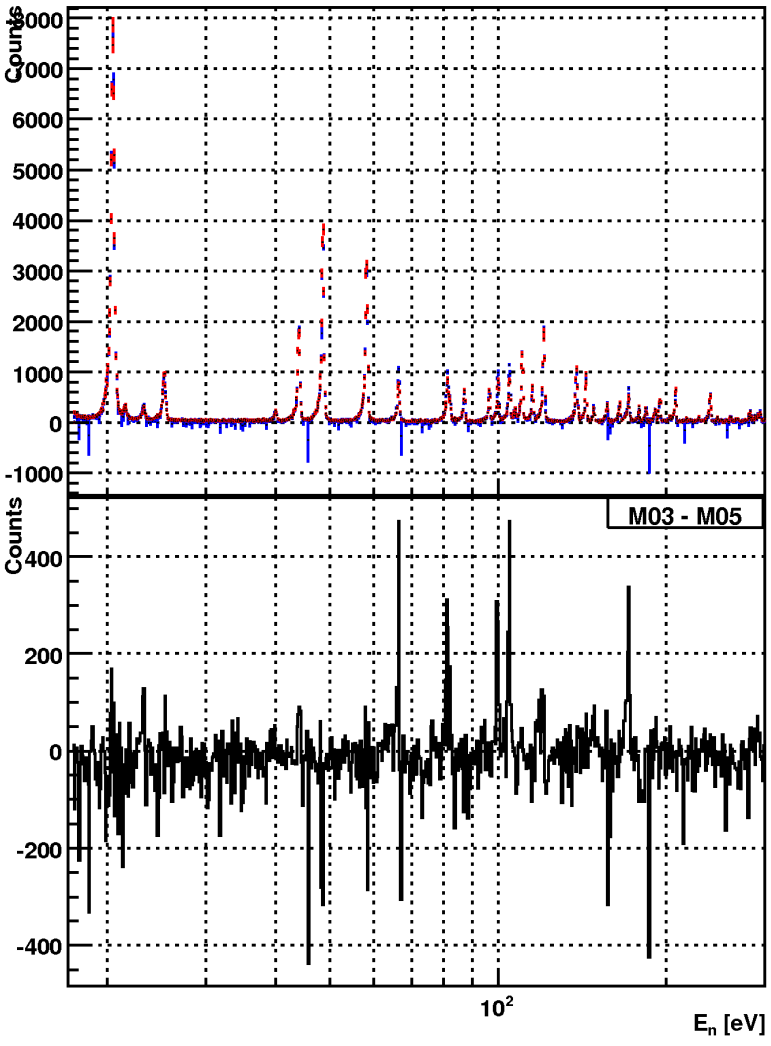

Figure A.2: Spin assignment for $J = 1$ resonances. E_n spectra of $M_1 = 3$ vs. $M_2 = 5$.

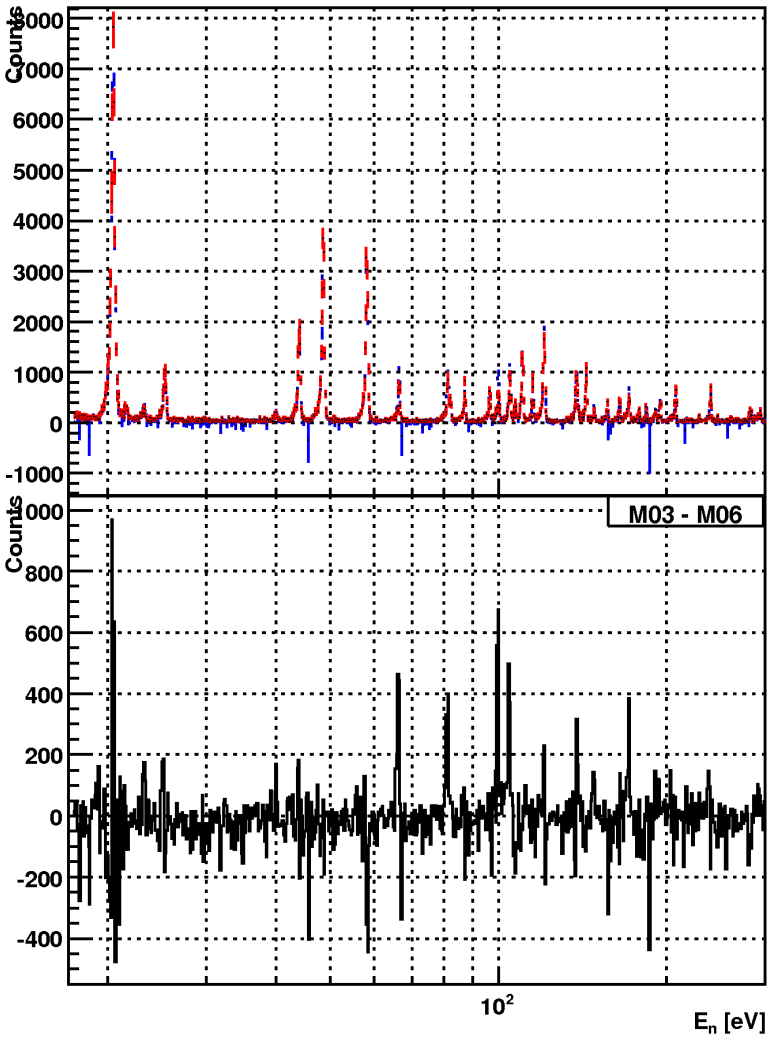

Figure A.3: Spin assignment for $J = 1$ resonances. E_n spectra of $M_1 = 3$ vs. $M_2 = 6$.

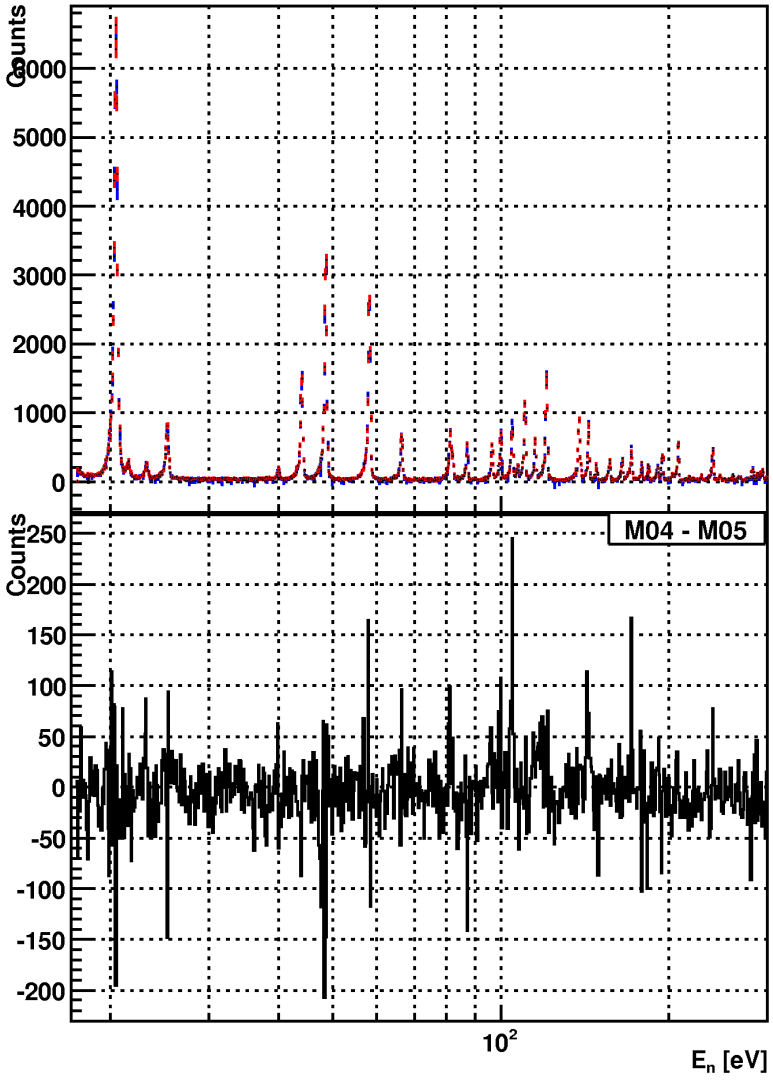

Figure A.4: Spin assignment for $J = 1$ resonances. E_n spectra of $M_1 = 4$ vs. $M_2 = 5$.

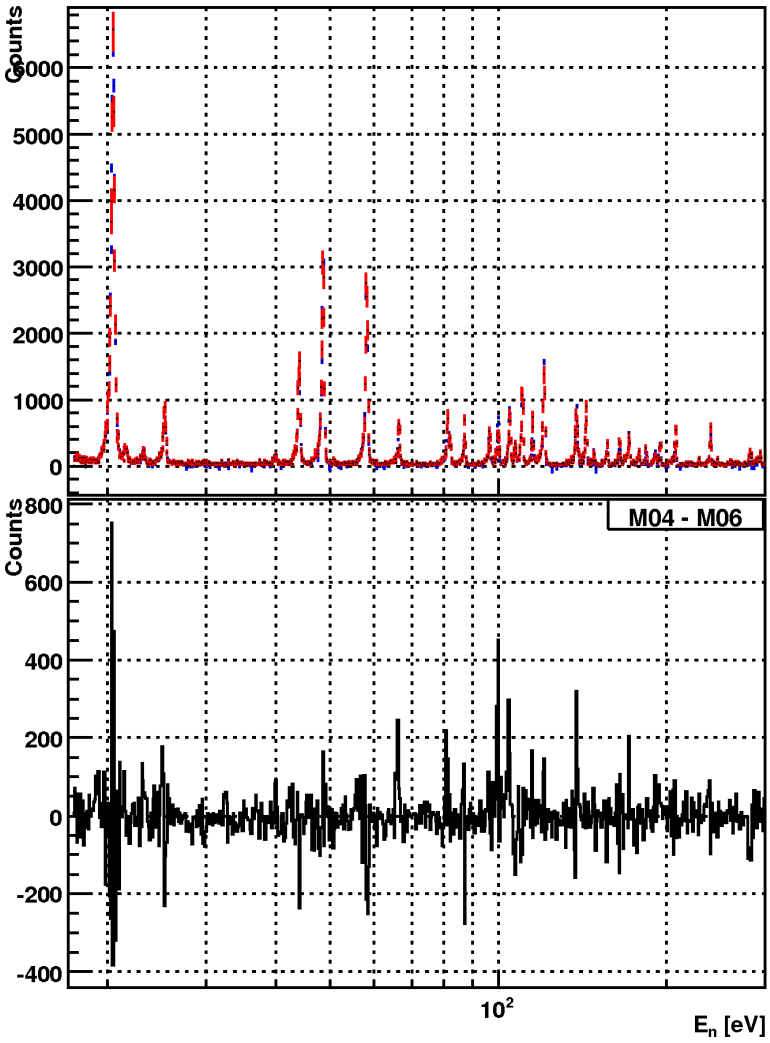

Figure A.5: Spin assignment for $J = 1$ resonances. E_n spectra of $M_1 = 4$ vs. $M_2 = 6$.

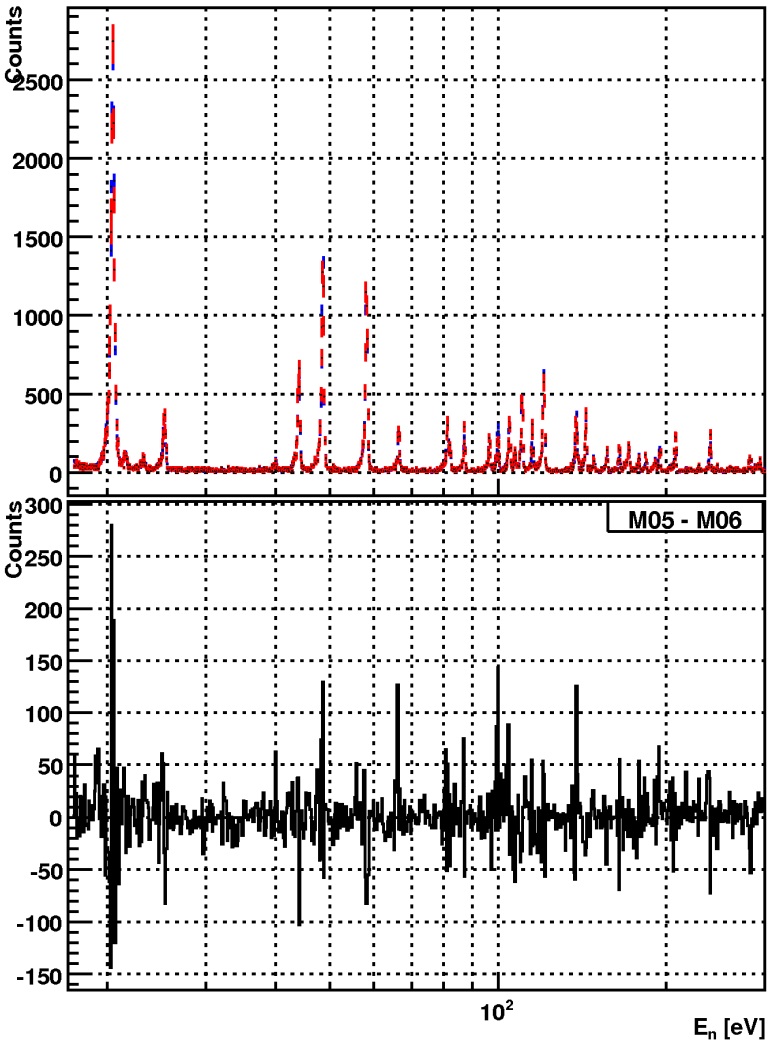

Figure A.6: Spin assignment for $J = 1$ resonances. E_n spectra of $M_1 = 5$ vs. $M_2 = 6$.

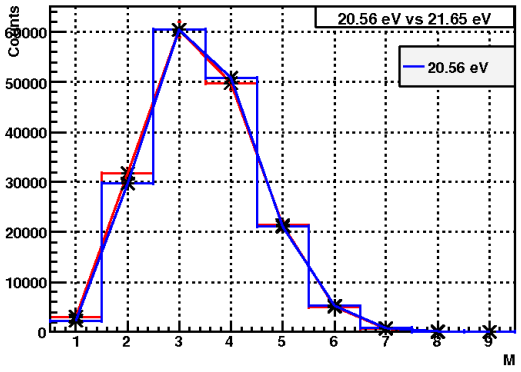

Figure A.7: The 21.65-eV resonance vs. the prototype 20.56-eV resonance.

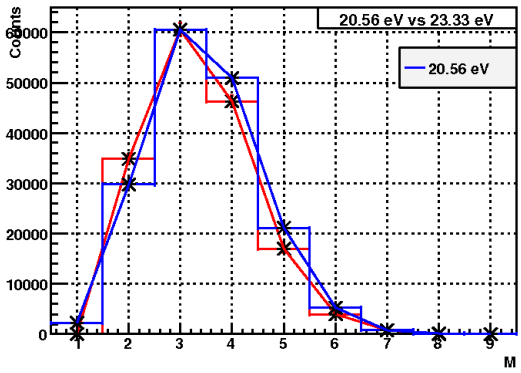

Figure A.8: The 23.33-eV resonance vs. the prototype 20.56-eV resonance.

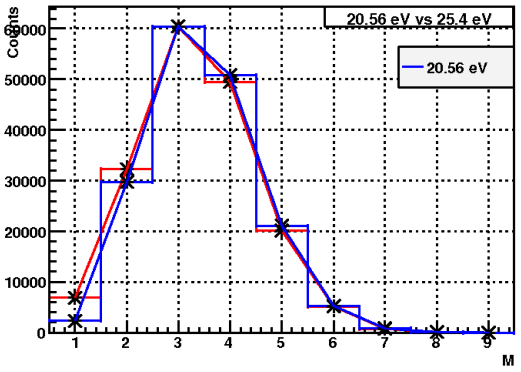

Figure A.9: The 25.4-eV resonance vs. the prototype 20.56-eV resonance.

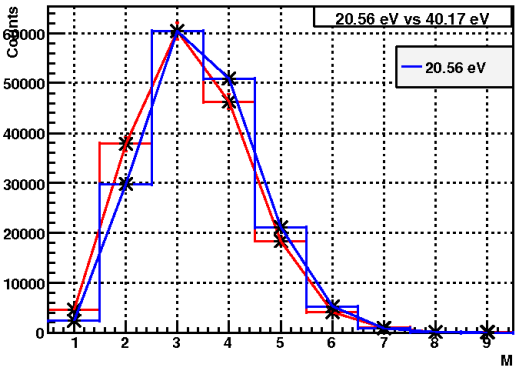

Figure A.10: The 40.17-eV resonance vs. the prototype 20.56-eV resonance.

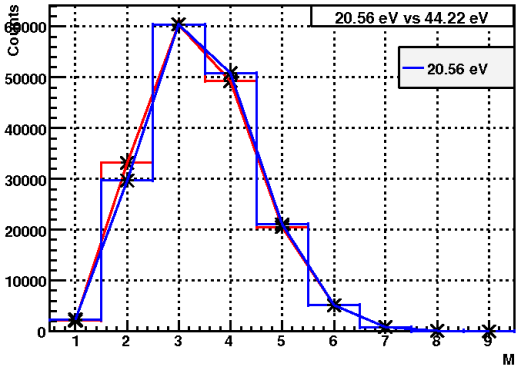

Figure A.11: The 44.22-eV resonance vs. the prototype 20.56-eV resonance.

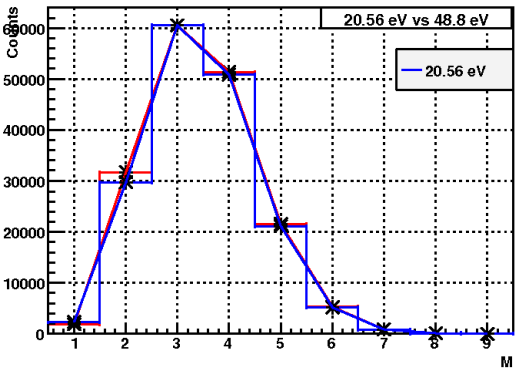

Figure A.12: The 48.8-eV resonance vs. the prototype 20.56-eV resonance.

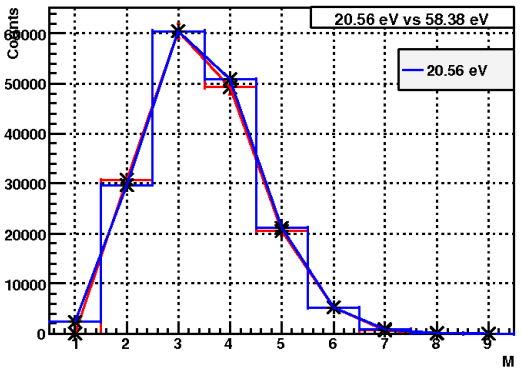

Figure A.13: The 53.38-eV resonance vs. the prototype 20.56-eV resonance.

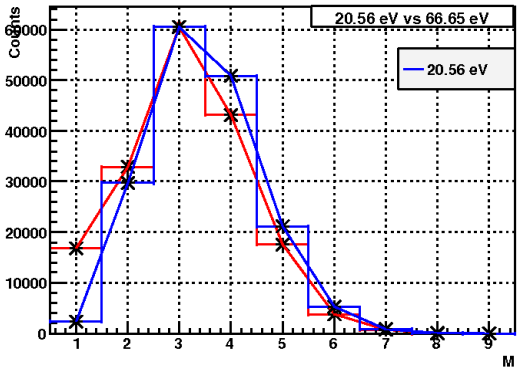

Figure A.14: The 66.65-eV resonance vs. the prototype 20.56-eV resonance.

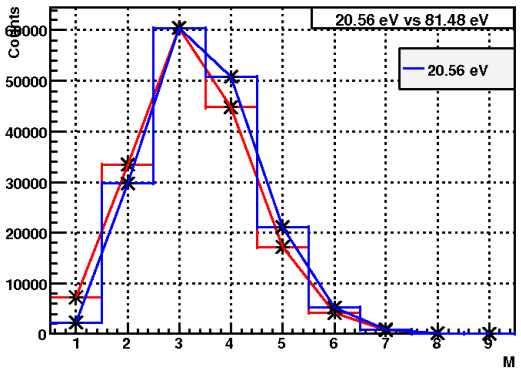

Figure A.15: The 81.48-eV resonance vs. the prototype 20.56-eV resonance.

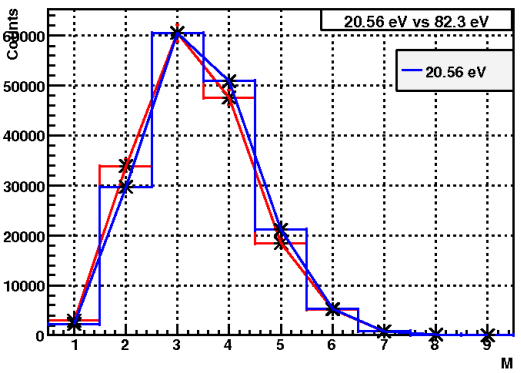

Figure A.16: The 82.3-eV resonance vs. the prototype 20.56-eV resonance.

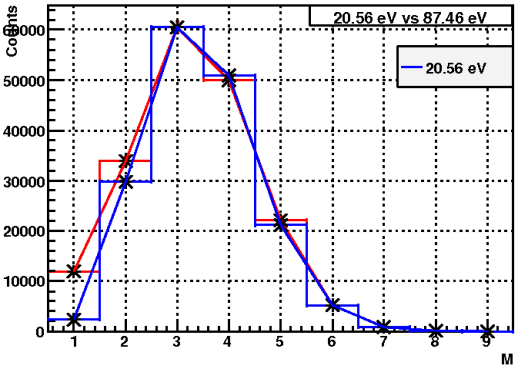

Figure A.17: The 87.46-eV resonance vs. the prototype 20.56-eV resonance.

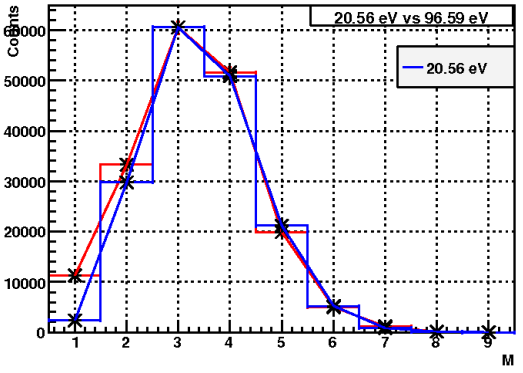

Figure A.18: The 96.59-eV resonance vs. the prototype 20.56-eV resonance.

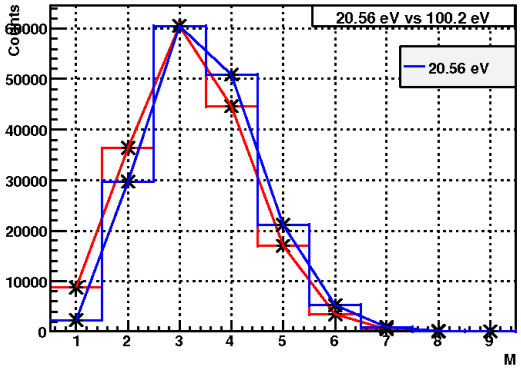

Figure A.19: The 100.2-eV resonance vs. the prototype 20.56-eV resonance.

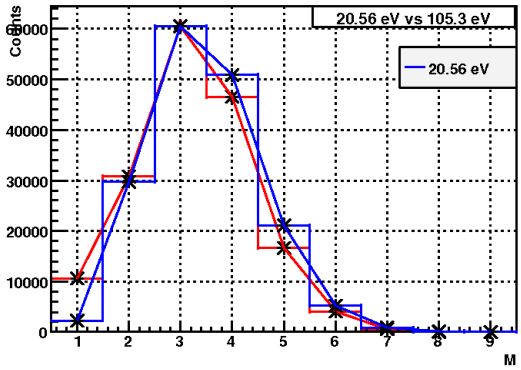

Figure A.20: The 105.3-eV resonance vs. the prototype 20.56-eV resonance.

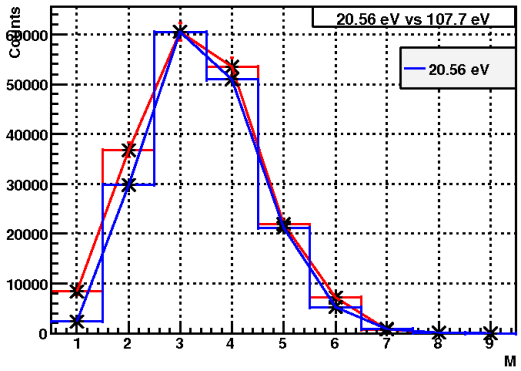

Figure A.21: The 107.7-eV resonance vs. the prototype 20.56-eV resonance.

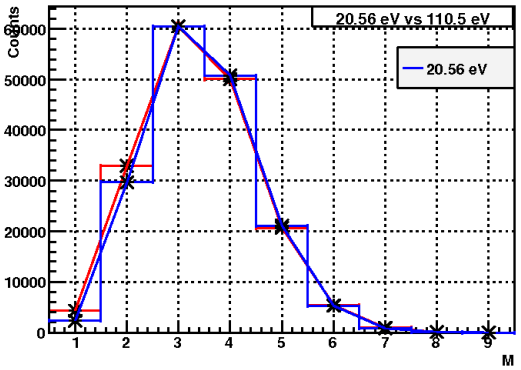

Figure A.22: The 110.5-eV resonance vs. the prototype 20.56-eV resonance.

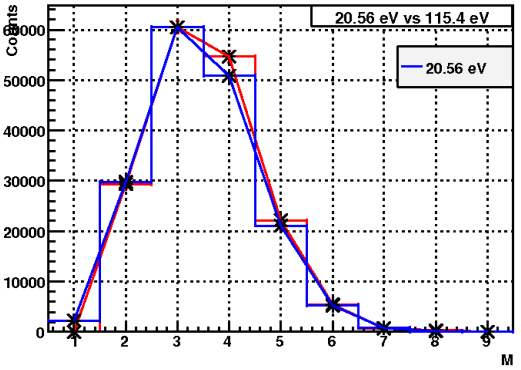

Figure A.23: The 115.4-eV resonance vs. the prototype 20.56-eV resonance.

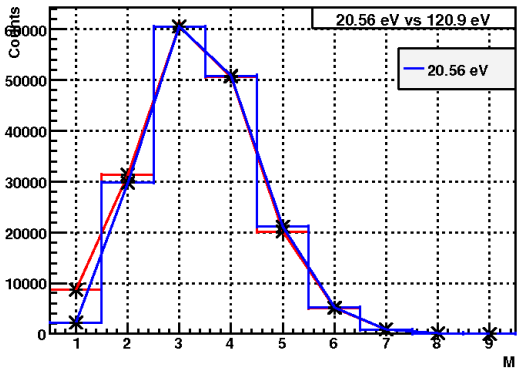

Figure A.24: The 120.9-eV resonance vs. the prototype 20.56-eV resonance.

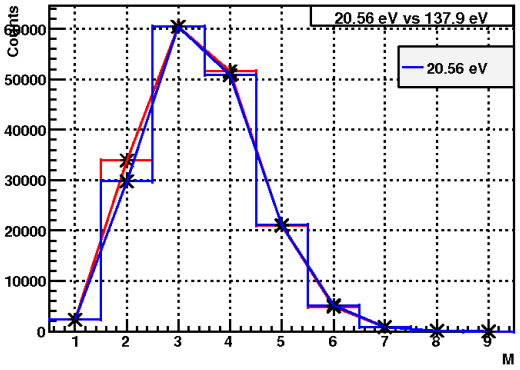

Figure A.25: The 137.9-eV resonance vs. the prototype 20.56-eV resonance.

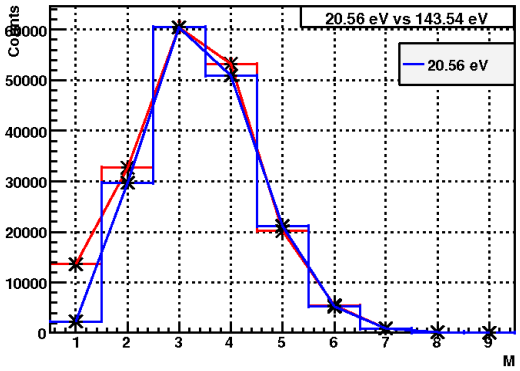

Figure A.26: The 143.54-eV resonance vs. the prototype 20.56-eV resonance.

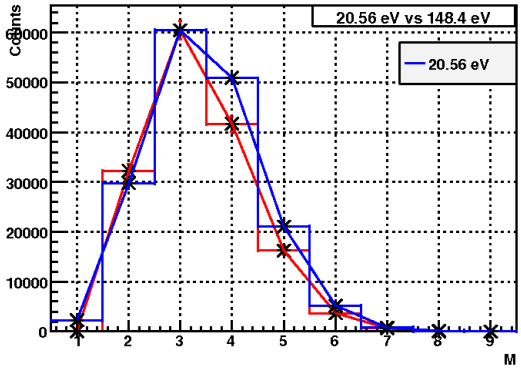

Figure A.27: The 148.4-eV resonance vs. the prototype 20.56-eV resonance.

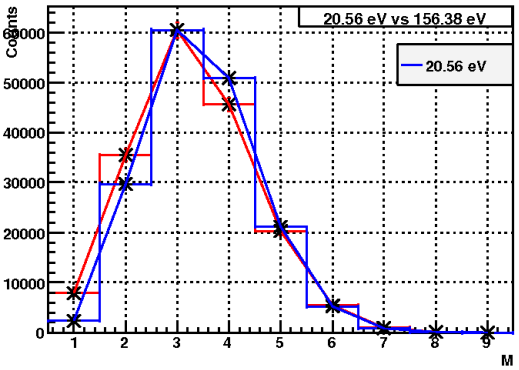

Figure A.28: The 156.38-eV resonance vs. the prototype 20.56-eV resonance.

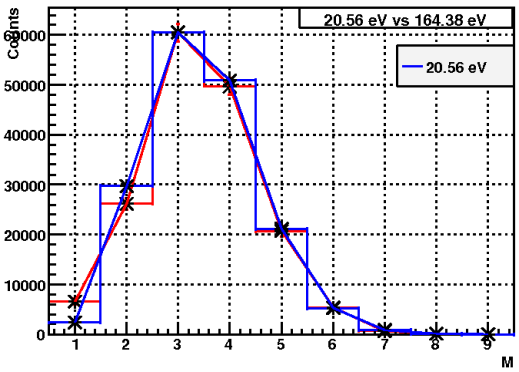

Figure A.29: The 164.38-eV resonance vs. the prototype 20.56-eV resonance.

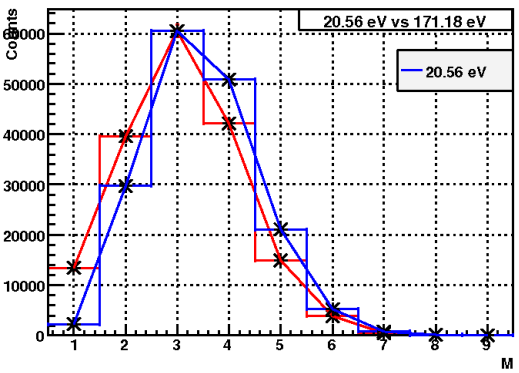

Figure A.30: The 171.18-eV resonance vs. the prototype 20.56-eV resonance.

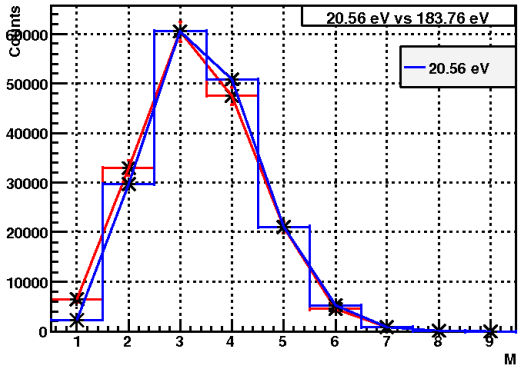

Figure A.31: The 183.76-eV resonance vs. the prototype 20.56-eV resonance.

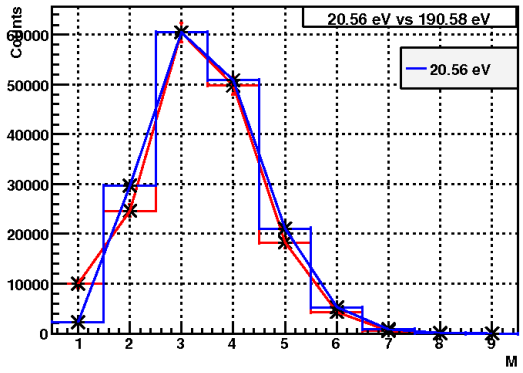

Figure A.32: The 190.58-eV resonance vs. the prototype 20.56-eV resonance.

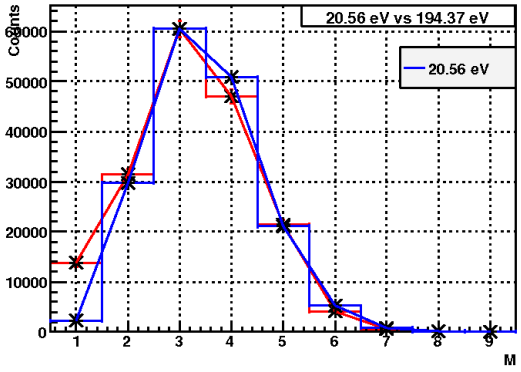

Figure A.33: The 194.37-eV resonance vs. the prototype 20.56-eV resonance.

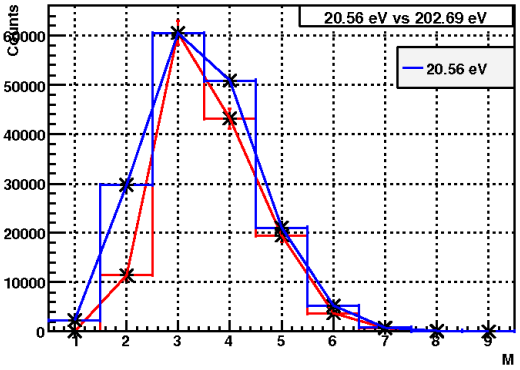

Figure A.34: The 202.69-eV resonance vs. the prototype 20.56-eV resonance.

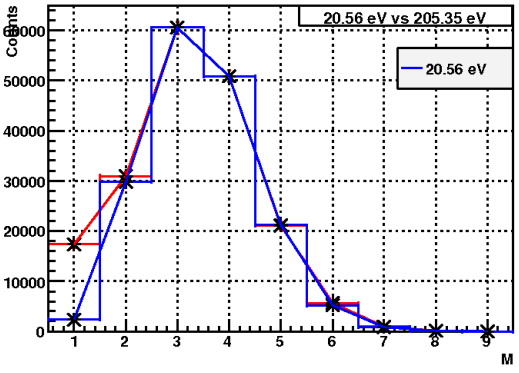

Figure A.35: The 205.35-eV resonance vs. the prototype 20.56-eV resonance.

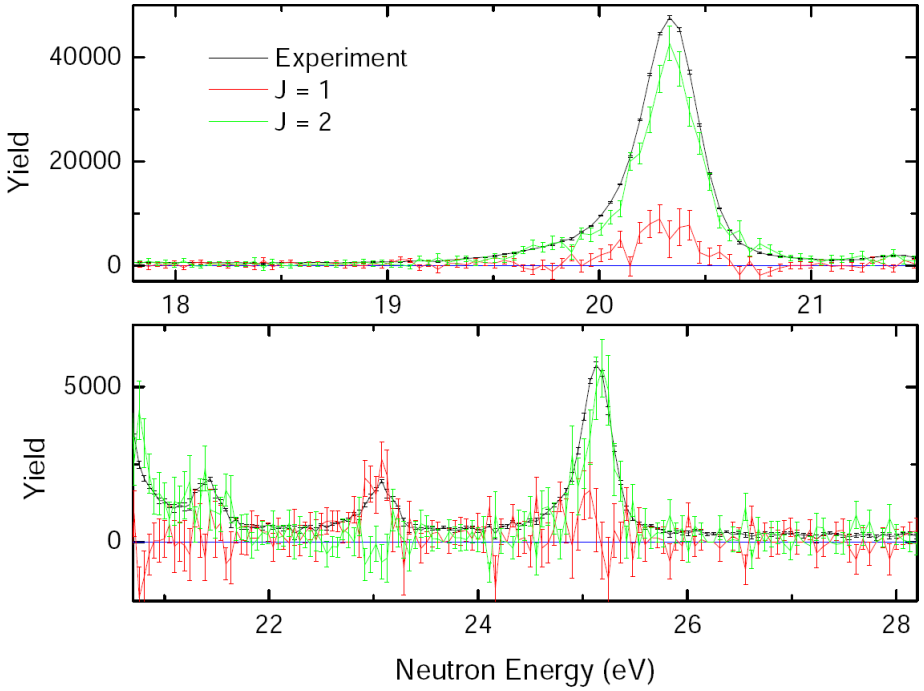

Figure A.36: Spin assignment in the range $E_n = 18 - 28$ eV.

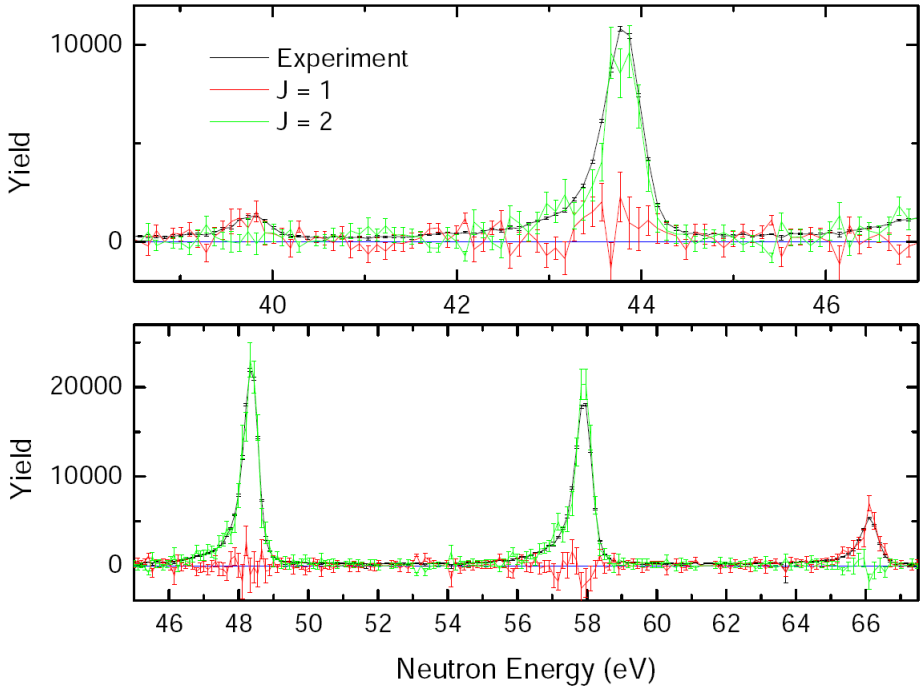

Figure A.37: Spin assignment in the range $E_n = 32 - 67$ eV.

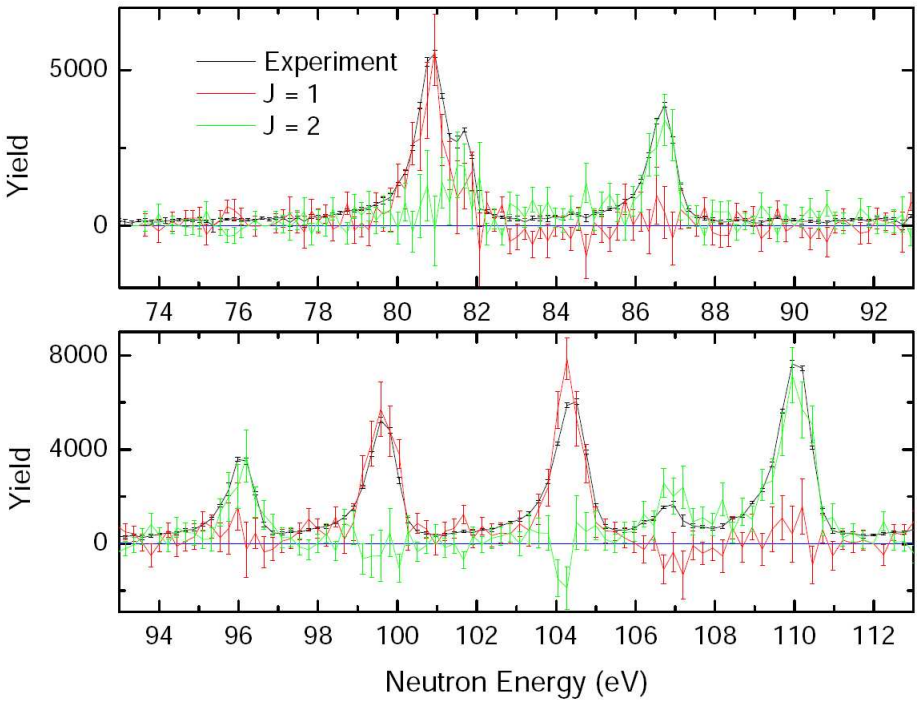

Figure A.38: Spin assignment in the range E_n = 73 – 112 eV.

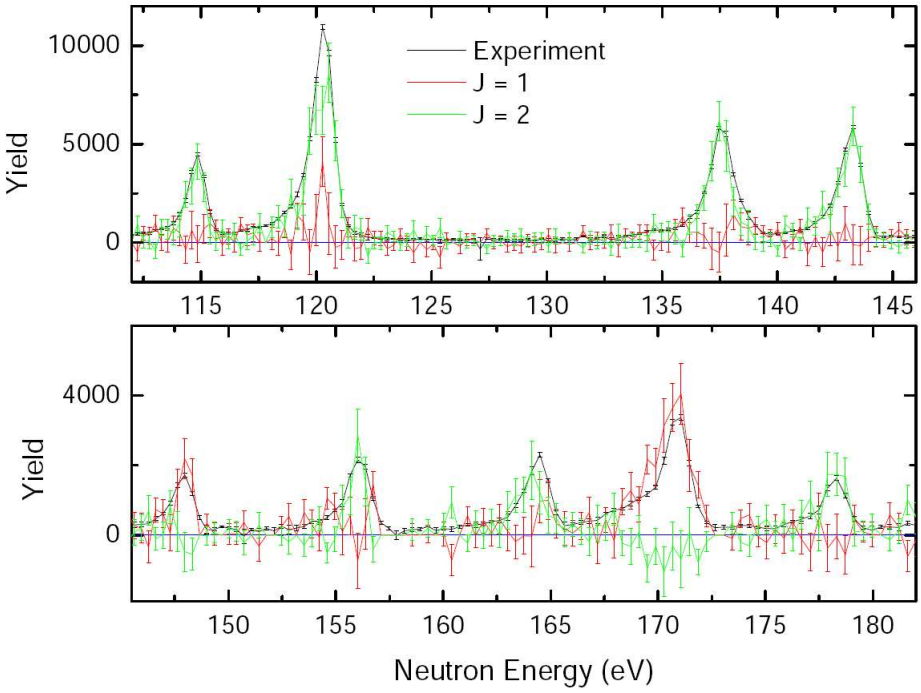

Figure A.39: Spin assignment in the range E_n = 113 – 180 eV.

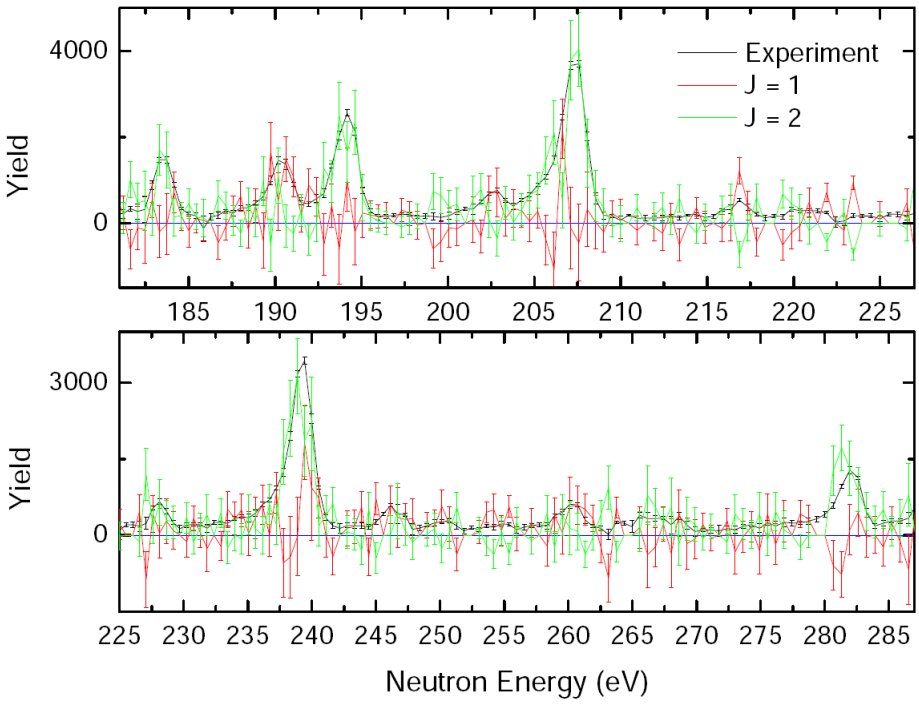

Figure A.40: Spin assignment in the range E_n = 180 – 285 eV.

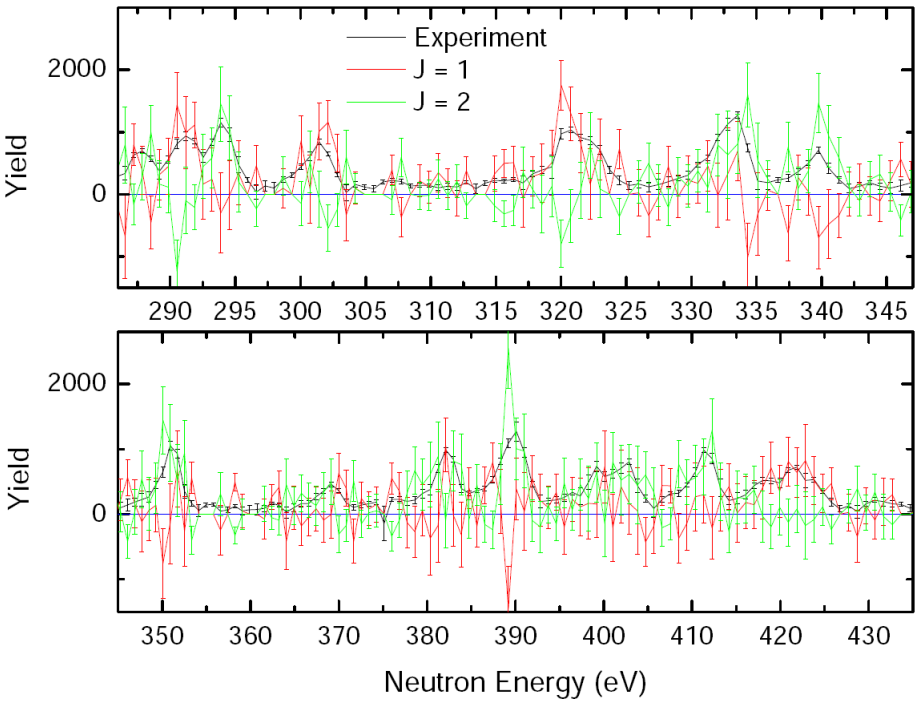

Figure A.41: Spin assignment in the range E_n = 285 – 430 eV.

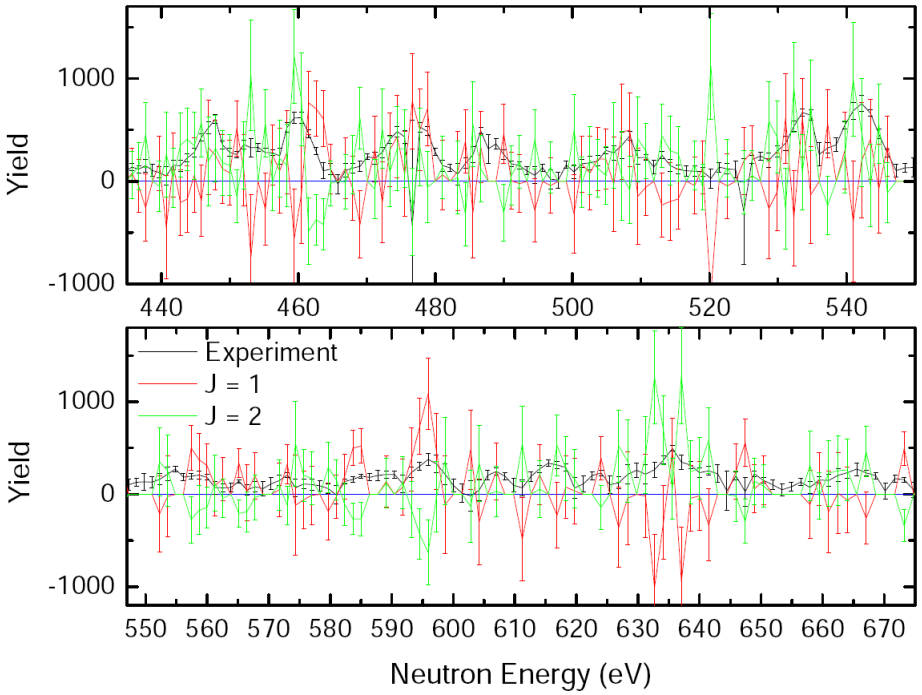

Figure A.42: Spin assignment in the range $E_n = 440 - 670$ eV.

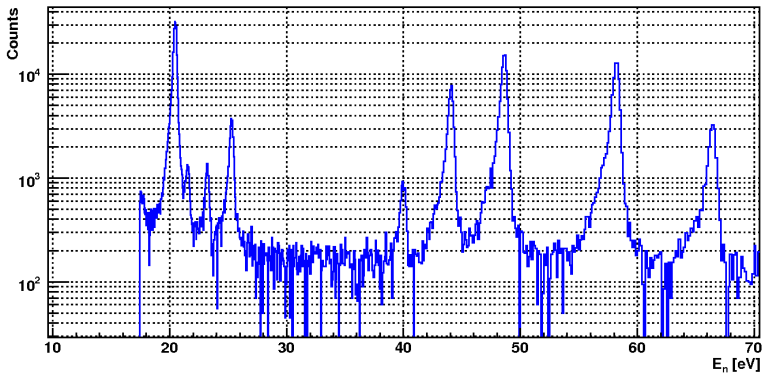

Figure A.43: ^{157}Gd resonances in the range $E_n = 10 - 70$ eV.

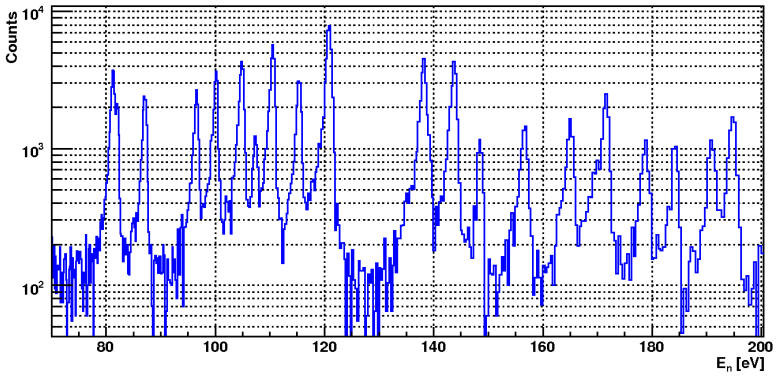

Figure A.44: ^{157}Gd resonances in the range E_n = 70 – 200 eV.

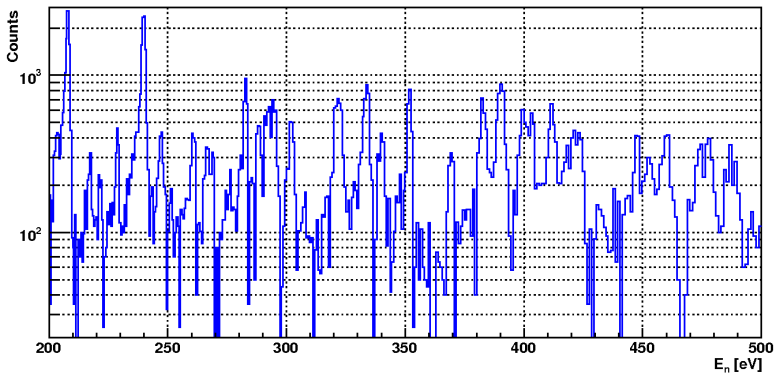

Figure A.45: ^{157}Gd resonances in the range E_n = 200 – 500 eV.

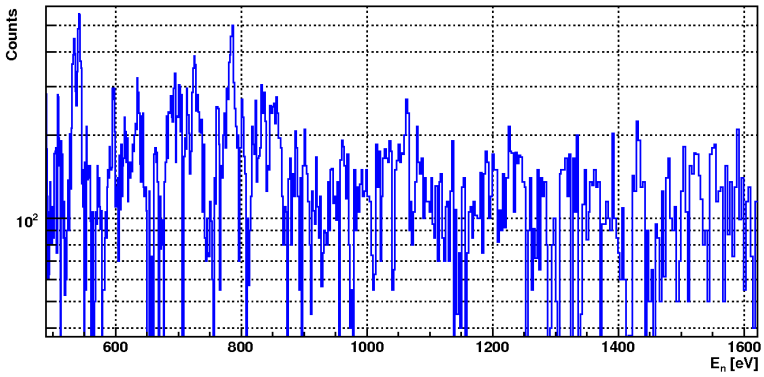

Figure A.46: ^{157}Gd resonances in the range E_n = 500 – 1600 eV.

A.2 List of additional tables for ^{157}Gd

The table below represents spin assignment by the 3 methods for the ^{157}Gd resonances. Author's method include 6 combinations of two cluster multiplicities M_i and M_j, thus, there are 6 possible spin assignments for each resonace. Kohler's method as well as Becvar's one make 1 spin assignment for each resonance.

If the spin value is the the brackets $[J_i]$, it means that this assignment is two-fold but the value J_i is more likely than the other possible spin value $J_j = J_i \pm 1$.

Table A.1: Results on the 3 methods (author, Koehler, Becvar) of the spin assignment for the ^{157}Gd resonances compared to the Atlas of Neutron Resonances of Mughabghab.

Mughabghab		**Author** $J(M_1 - M_2)$						**Koehler**	**Becvar**
E_0 [eV]	J	3-4	3-5	3-6	4-5	4-6	5-6	J	J
0.0314 ±0.0002									
2.825 ±0.015									
16.24 ±0.03									
16.77 ±0.06									
20.56 ±0.04	2	2	2	2	2	2	2		2
21.65 ±0.04	2							2	2
23.33 ±0.04	1	1	1	1	1	1	[1]	1	1
25.4 ±0.04	2	2	2	2	2	2	2	2	2
40.17 ±0.09	1	1	1	1	[1]	[1]		1	[1]
44.22 ±0.1	2	2	2	2	2	2	2	2	2
48.8 ±0.11	2	2	2	2	2	2	2	2	2
58.38 ±0.08	2	2	2	2	2	2	2	2	2
66.65 ±0.15	1	1	1	1	1	1	[1]	1	2
81.48 ±0.15	1	1	1	1	1	1	1	1	1
82.30 ±0.15	2	[2]	[2]	2		[2]	[2]	[2]	
87.46 ±0.15	2	2	2	2	2	[2]	[2]	2	2
96.59 ±0.15	1	2	2	2	2	2	[2]	2	2
100.2 ±0.1	1	1	1	1	1	1	1	1	1

Continued on next page

Table A.1 Continued from previous page

Mughabghab		**Author** $J(M_i - M_j)$						**Koehler**	**Becvar**
E_0 [eV]	J	3-4	3-5	3-6	4-5	4-6	5-6	J	J
105.3 ±0.1	1	1	1	1	1	1	1	1	1
107.7 ±0.1	2	[2]		[2]		[2]	[2]	[2]	2
110.5 ±0.1	2	2	2	2	2	2	2	2	2
115.4 ±0.1	2	2	2	2		2	[2]	2	2
120.9 ±0.15	1		2	2	2	2	2	2	2
135.19 ±0.15	2								
137.9 ±0.15	2	2	2	2	2	2	2	2	2
138.8 ±0.15	2								
139.3 ±0.15	2								
143.54 ±0.15	2	2	2	2	2	2	2	2	2
148.4 ±0.15	1	1	1	1				1	1
156.38 ±0.15	2	2	2	2	[2]	2	2	[2]	2
164.38 ±0.15	2	2	2	2	[2]		[2]	2	2
167.88 ±0.15	2								
169.51 ±0.15	2								
171.18 ±0.15	1	1	1	1	1	1	[1]	1	1
178.48 ±0.15	2	2	2	2	2	[2]			2
183.76 ±0.15	2		2		[2]			[2]	2
190.58 ±0.15	1		[1]					[1]	[1]
194.37 ±0.15	2							2	2
202.69 ±0.15	1							1	
205.35 ±0.25	2							2	2
207.56 ±0.25	2	2	2	2	2	2	[1]		
216.9 ±0.25	1								
220.65 ±0.25	1	1							
228.05 ±0.25	2								
239.3 ±0.25	1	2	2	2	[2]	2	2		2

Continued on next page

Table A.1 Continued from previous page

Mughabghab		**Author** $J(M_i - M_j)$						**Koehler**	**Becvar**
E_0 [eV]	J	3-4	3-5	3-6	4-5	4-6	5-6	J	J
244.6 ±0.25	[1]								
246.39 ±0.25	2			2					
250.2 ±0.25	1								
255.0 ±0.25									
255.2 ±0.25									
260.05 ±0.25	1								
265.61 ±0.25	2								
268.02 ±0.25	2								
281.02 ±0.25	1	[2]	[2]	2		2	2		2
287.6 ±0.25	2								
290.8 ±0.25	1			1		[1]			1
293.7 ±0.25	[1]								[2]
300.9 ±0.8	1	1	1	1	[1]	[1]			[1]
306.4 ±0.25									
319.0 ±0.25	[1]		[1]	[1]	[1]	[1]	[1]		1
321.0 ±0.25	[2]								
339.0 ±0.25	2					[2]			[2]
350.42 ±0.25	2		2	2		[2]			[2]
367.95 ±0.25	2								
381.14 ±0.25	2		2		[2]				
388.83 ±0.25	2		2	2	2	[2]			[2]
397.81 ±0.25	1								
401.21 ±0.25	2								
416.4 ±0.4	2								
421.0 ±0.4	2					[1]	[1]		
429.5 ±0.4	2								
445.4 ±0.4	2								

Continued on next page

Table A.1 Continued from previous page

Mughabghab		**Author** $J(M_i - M_j)$						**Koehler**	**Becvar**
E_0 [eV]	J	3-4	3-5	3-6	4-5	4-6	5-6	J	J
451.4 ±0.4	1								
457.9 ±0.4	2								
472.0 ±0.4	2								
475.8 ±0.4	2								
485.4 ±0.4	2								
510.1 ±0.4	1								
530.4 ±0.4	2								
539.3 ±0.4	2								
555.3 ±0.4	1								
584.0 ±0.4	2								
593.0 ±0.4	1		1	1	1	[1]	[1]		[1]
602.5 ±0.4	2								
618.4 ±0.4	2								
666.6 ±0.4	2								
743.8 ±0.4	2								
756.6 ±0.4	2								